## **Investigation of Novel Lead-Free BiFeO<sub>3</sub>-CaTiO<sub>3</sub> Piezoelectric Ceramics for High-Temperature Energy Storage Applications**

Thesis submitted in partial fulfilment of the requirements for the degree of

#### **DOCTOR OF PHILOSOPHY**

in

#### **MATERIALS ENGINEERING**

by

#### Gomasu Sreenu

(Reg. No. 18ETPM01)

*Under the supervision of* 

Prof. Dibakar Das





# SCHOOL OF ENGINEERING SCIENCES AND TECHNOLOGY UNIVERSITY OF HYDERABAD

HYDERABAD, TELANGANA, INDIA – 500046

**July 2023** 



#### School of Engineering Sciences and Technology, University of Hyderabad, Institution of Eminence, Hyderabad, Telangana, India, 500046



#### **CERTIFICATE**

This is to certify that the thesis entitled, "Investigation of Novel Lead-Free BiFeO<sub>3</sub> - CaTiO<sub>3</sub> Piezoelectric Ceramics for High-Temperature Energy Storage Applications" submitted by Gomasu Sreenu, bearing registration number 18ETPM01 in partial fulfilment of the requirements for the award of Doctor of Philosophy in Materials Engineering, School of Engineering Sciences and Technology, is a bonafide work carried out by him under my supervision and guidance.

This thesis is free from plagiarism and has not been submitted previously in part or in full to this or any other University or Institute for the award of any degree or diploma.

Parts of this thesis have been:

#### A. Published in the following publications:

- 1. <u>Gomasu Sreenu</u>, Mahfooz Alam, Didier Fasquelle, Dibakar Das "High-frequency dielectric characterization of novel lead-free ferroelectrics" J Mater Sci: Mater Electron, 31, 18477–18486 (2020). https://doi.org/10.1007/s10854-020-04391-7
- **2. Gomasu Sreenu**, Subhadeep Saha, R. N. Bhowmik, J. P. Praveen, Dibakar Das "Investigation of structural, electrical, and dielectric properties of lead-free (BiFeO<sub>3</sub>)<sub>(1-x)</sub> (CaTiO<sub>3</sub>)<sub>x</sub> ceramics" J Mater Sci: Mater Electron 33, 24959–24971 (2022). https://doi.org/10.1007/s10854-022-09205-6
- **3.** Subhadeep Saha, <u>Gomasu Sreenu</u>, J Paul Praveen, Dibakar Das "Effect of Nd<sup>3+</sup> substitution on structural, morphological, and electrical properties of Bismuth Ferrite ceramics" J Mater Sci: Mater Electron 34, 559 (2023). <a href="https://doi.org/10.1007/s10854-023-09947-x">https://doi.org/10.1007/s10854-023-09947-x</a>
- **4.** <u>Gomasu Sreenu</u>, Subhadeep Saha, and Dibakar Das, "Synthesis of Novel Lead-free (BiFeO<sub>3</sub>)<sub>(x)</sub> (CaTiO<sub>3</sub>)<sub>(1-x)</sub> Ceramics and Thermal, Structural, Microstructural and Ferroelectric Characterizations for Energy Storage Applications" AIP conference proceedings (2023) (Accepted)

#### B. Presented at the following conferences:

- Gomasu Sreenu, Dibakar Das, Oral talk on "Lead-free ferroelectric materials for energy storage applications" at Science, Technology, and Innovation Talks (STIN-2021) as a part of National Science Day celebrations organized by the International Advanced Research Centre for Powder Metallurgy and New Materials (ARCI), held from 25<sup>th</sup>- 26<sup>th</sup> February-2021, Hyderabad, India.
- 2. <u>Gomasu Sreenu</u>, Subhadeep Saha, Dibakar Das, Poster presentation on "Synthesis and characterization of (x)BiFeO<sub>3</sub> (1-x) CaTiO<sub>3</sub> solid solution for structural, morphological, thermal and electrical properties" at Second International e-conference on Physics of Materials & Nanotechnology (ICPN-2021) held from 28<sup>th</sup> to 30<sup>th</sup> Oct 2021, Organized by Department of Physics, Mangalore University, India.
- 3. <u>Gomasu Sreenu</u>, Subhadeep Saha, Dibakar Das, Flash talk/Oral presentation on "Structural and electrical characterizations of novel lead-free ferroelectric bulk ceramics (1-x)BiFeO<sub>3</sub> –xCaTiO<sub>3</sub> for energy storage applications" in the 'International Virtual Conference on Advanced Ceramics and Technologies: Materials and manufacturing (IvaCCT- 2021) held from 13<sup>th</sup>-14<sup>th</sup> Dec 2021 organized by Indian ceramic society Karnataka chapter.
- 4. <u>Gomasu Sreenu</u>, Subhadeep Saha, RN Bhowmik, Dibakar Das, **Oral presentation** on "A Novel Lead-free Ferroelectric High Energy Density Ceramic System for High-Temperature Energy Storage Applications" at AEM2022 **Imperial College London, UK** held from 6<sup>th</sup> 8<sup>th</sup> April 2022.
- 5. <u>Gomasu Sreenu</u>, Subhadeep Saha, RN Bhowmik, D Das, Poster presentation "Dielectric and Ferroelectric Characteristics of (BiFeO<sub>3</sub>)<sub>(1-x)</sub> –(CaTiO<sub>3</sub>)<sub>x</sub> Lead-Free Ceramics for High-Temperature Energy Storage Application" at IIM-ATM, RFC Hyderabad, India held from 14<sup>th</sup> 16<sup>th</sup> November 2022.
- 6. <u>Gomasu Sreenu</u>, Subhadeep Saha, D das Poster presentation "Dielectric and Electrical Characterizations of Lead-free (BiFeO<sub>3</sub>)<sub>(1-x)</sub> (CaTiO<sub>3</sub>)<sub>x</sub> Ceramics for Energy Storage Applications" at Global Trends in Traditional to Space Ceramics organized by Indian ceramic society, IIT-BHU held from 8<sup>th</sup> 9<sup>th</sup> December 2022.
- 7. **Gomasu Sreenu**, Subhadeep Saha, Dibakar Das, Poster presentation "Synthesis of Novel Lead-free (BiFeO<sub>3</sub>)<sub>(x)</sub> (CaTiO<sub>3</sub>)<sub>(1-x)</sub> Ceramics and Thermal, Structural, Microstructural and Ferroelectric Characterizations for Energy Storage Applications" at 66th DAE Solid State Physics Symposium, Birla Institute of Technology Jharkhand, India held from 18<sup>th</sup> to 22<sup>nd</sup> Dec 2022.

Gomasu Sreenu, Subhadeep Saha, RN Bhowmik, Dibakar Das Poster presentation on "Structural and Electrical Characteristics of a novel Lead-free Ferroelectric (1-x)BiFeO3 -xCaTiO3 Ceramics for High-Temperature Energy Storage Application" at advanced in functional materials (AFM), Kyushu University, Fukuoka, Japan held from 9th to 12th Jan 2023.

The student has passed the following courses towards fulfilment of the coursework requirement for Ph. D.

Course Code	Title of the Course	Credits	Results
PD801	Research Methodology	4	Pass
PD802	Advanced Materials Processing and Characterization	4	Pass
PD803	Advanced Engineering Mathematics	2	Pass
PD805	Materials Characterization - I	4	Pass

Supervisor P. 1655 Pros 201

Prof. Dibakar Das
School of Engineering Sciences and

Technology (SEST), University of

Hyderabad, Hyderabad, T.S. India

Dean of the School

Dr. Jai Prakash Gautam

Professor & Dean,

School of Engineering Sciences and

Technology (SEST), University of

Hyderabad, T.S. India

University of Hyderabad Hyderabad-500046.

## Thesis Approval for Ph.D.

This Thesis entitled "Investigation of Novel Lead-Free BiFeO<sub>3</sub> - CaTiO<sub>3</sub> Piezoelectric Ceramics for High-Temperature Energy Storage Applications" by Gomasu Sreenu (Reg. No. 18ETPM01), is approved for the degree of Doctor of Philosophy.

Examiners
S
Supervisor

#### **DECLARATION**

I, Gomasu Sreenu, declare that this thesis entitled, "Investigation of Novel Lead-Free BiFeO3 - CaTiO3 Piezoelectric Ceramics for High-Temperature Energy Storage Applications" has been composed solely by myself under the supervision of Prof. Dibakar Das, UoH and it has not been submitted, in whole or in part, in any previous application for the award of any degree. To the best of my knowledge, this thesis contains no material previously published by any other person and appropriate references/citations are made for results and literature obtained from different authors for comparison purposes. I also declare that I have adhered to all academic honesty and integrity principles and have not misprinted or fabricated falsified any idea/ data/ fact/ source in my thesis submission. I understand that any violation of the above will cause disciplinary action by the Institute and can also evoke penal action from the sources that have not been properly cited or from whom proper permission has not been taken when needed.

(Signature)

Gomasu Sreenu

Reg. No.: 18ETPM01

Date: 22/02/2023

#### **ACKNOWLEDGEMENTS**

It has been a truly marvellous journey in my life, replete with numerous surprises and delights. This period of pursuing my PhD not only imparted invaluable scientific knowledge through diverse experiments but also allowed me to glean wisdom from a plethora of individuals, traditions, and cultures. It has enriched my understanding of research and life, exposing me to an array of captivating concepts and fascinating personalities.

Above all, I wish to extend my sincere gratitude to my esteemed supervisor, Professor Dibakar Das, from the distinguished School of Engineering Sciences and Technology (SEST) at the esteemed University of Hyderabad (UoH). His guidance in introducing me to the captivating realm of energy storage systems for my current research topic has been invaluable. Throughout the course of my PhD study, his unwavering advice, constant support, encouragement, motivation, and remarkable patience have been instrumental in shaping my academic journey. Professor Das' profound erudition, fast and effective working nature and vast reservoir of experience have been a constant source of inspiration and fortitude, propelling me forward in my scholarly pursuits.

I express my heartiest regards to the doctoral committee members Prof. Jai Prakash Gautam and Prof. S Srinath for their valuable insights, guidance, support, and encouragement. I want to thank the deans of SEST present and former and all department faculties for their support. I extend my gratitude to the UoH admin for their support.

I would like to thank funding bodies; Department of Science and Technology (DST) FIST, DST PURSE UGC-Grant, Non-Net fellowship, University of Hyderabad, The Institution of Eminence (IoE) grant University of Hyderabad (UoH) Govt of India.

I want to thank my research collaborators; Prof. Fasquelle Didier, UDSMM Head of the group: Materials & Functional Oxides for Applications, University of the Littoral Opal Coast (ULCO), France. I sincerely thank Dr Siddhartha Ghosh, SoP, SRM University, AP, India for providing constructive suggestions. I want to thank Dr Rabindranath Bhowmik, SoP, Pondicherry University, India for providing infrastructural support and valuable insights. Dr A. R. James (Scientist-E), DMRL Hyderabad, India. Dr Cheng-Sao Chen, ME, Hwa Hsia University of Technology, Taiwan.

I would like to thank the seniors; Dr Jai Shree, Dr Paul, Dr Leela Sree, Dr Anshu, Dr Khushnuma, Dr Qasim and Dr Indla, Dr Janakiram, Dr Pandu Sunil, Dr Ravikiran, Dr Kamal, Dr Johnny

I want to thank research scholars Mahfooz Alam, Sukumoy, Parthiban, and Ranjan I would like to thank my batch mates Sai, Jyoti, and Mamatha.

I want to thank my lab mates Saha, Arun, Mahesh, Gouri, Ramesh and Manidipta Friends Arun, Deekshith, Aakash, Charan, Madhu, Srikanth, Vinay, Hasan, Bharath, Anil, Shiva, Nanda, Sai, Ranjith, Dharani, Bindu, Sravani. I want to thank Dr Dhamodar, Dr Santhosh, all technical and non-technical staff SEST, and the UoH fraternity. I extend my gratitude to Prof. Manisha Priyam, Kiran, Sujatha, and Suki Iyer.

I would like to thank my family for their unconditional love and support

Gomasu Sreenu

#### **ABSTRACT**

As the global population continues to expand at an unprecedented rate and the global economy thrives, there is a similar surge in energy consumption worldwide. However, this surge in energy demand brings forth many challenges that cannot be overlooked. One of the most pressing concerns is the detrimental impact of energy consumption on the environment. High CO, CO<sub>2</sub> levels, air pollution, and the exhaustion of fossil fuel reserves are all significant issues that need urgent attention. Lead is hazardous to human health and the environment, so looking for lead-free energy storage systems has gained interest in recent years. Considering these problems, it becomes evident that tapping various green and regenerative energy sources is the most promising resolution. The usage of energy storage systems is increasing day by day in electrical and electronic devices, viz., in hybrid electric vehicles, pulsed power systems and high-frequency inverters. In bulk form, they may be used as dielectric resonators, filters in communication, and devices as window sections in microwave windows in fusion reactors or as high-power antennas in pulsed power transmitters.

In the present investigation, BFO-BZO, BFO-CTO, and BFO-STO matrix were initially fabricated and thorough structural, microstructural, and dielectric properties were explored. Lead-free (1-x) BiFeO<sub>3</sub>-xCaTiO<sub>3</sub> (BFO-CTO) (x = 0.1, 0.3, and 0.5) piezoelectric ceramics have been studied for possible applications in high-temperature energy storage systems. The influence of CTO on the energy storage properties of BFO at high temperatures has been studied in detail from a thorough analysis of the structural and dielectric properties of the BFO-CTO system. Novel lead-free (1-x) BFO-xCTO (x = 0.6, 0.7, and 0.8) RFEs were synthesized using the solution auto combustion method, and structural and microstructural properties were systematically explored. CTO incorporation into the BFO-CTO matrix suppressed the formation of oxygen vacancies, and Fe-ion fluctuations by inhibiting the Fe<sup>+3</sup> to Fe<sup>+2</sup> transition confirmed through XPS. I-V hysteresis loops, frequency, temperature-dependent dielectric properties and dielectric relaxation times were discussed in detail. The ultrafast dielectric relaxation time of 44  $\mu$ s was obtained for 0.7 of x. Stable P-E loops were observed up to 190 °C and a high recoverable energy density of 2.5 J cm<sup>-3</sup> was obtained for the bulk ceramics.

## **Table of Contents**

CERTIFICATE	ii
Thesis Approval for Ph.D.	v
DECLARATION	vi
ACKNOWLEDGEMENTS	vii
ABSTRACT	ix
LIST OF FIGURES	xiii
LIST OF TABLES	xixx
Nomenclature	XX
Abbreviations	xxii
CHAPTER - 1	1
INTRODUCTION	1
1.1 Significance of energy	1
1.2 Types of energy storage systems	2
1.3 Electrochemical energy storage	3
1.4 Capacitors and perovskite ceramics applications	3
1.5 Perovskite	5
1.6 Ferroelectricity	6
1.6.1 Multiferroics	7
1.7 Bismuth ferrite	8
1.8 Crystal structure of BFO	8
1.9 Ferroelectric properties	9
1.10 Electrostatic energy storage in Ceramics	10
1.10.1 Electrostatic Capacitors	10
1.11 Crucial factors for assessing the properties of energy storage	11
REFERENCES	15
CHAPTER - 2	19
LITERATURE REVIEW	19
2.1 Lead-free ferroelectric dielectric ceramics	19
2.2 Research interest gained towards electrostatic energy storage capacitors from 2010 - 2020	20
2.3 Recent investigations on lead-free materials for energy density and efficiency	21
2.4 Efficiency and recoverable energy density of various lead-free materials	22
2.5 Recent investigations on lead-free BFO-based ceramics and key findings	23
REFERENCES	26
CHAPTER - 3	30
OBJECTIVE OF THE WORK	30
CHAPTER - 4	32
EXPERIMENTAL PROCEDURE	32
4.1 Synthesis of BiFeO <sub>3</sub> powder using solution combustion route	32

4.2 Synt	hesis of CaTiO <sub>3</sub> powder using solution combustion route	33
4.3 Calc	ination	34
4.4 Grai	nulation	36
4.5 Pelle	etization	36
4.6 Bind	er burnout and sintering	39
4.6.1	Microwave sintering technique	39
4.7 Dens	sity measurement	41
4.8 Elect	troding	41
4.9 The	characterization techniques used in the present investigation	43
CHAPTER -	- 5	45
RESULTS A	ND DISCUSSIONS	45
5A Stru	ctural, and high-frequency dielectric characterization of novel lead-free BFO-CTO, Bl	F <b>O-</b>
BZO, and	BFO-STO ferroelectric ceramics	45
5A. 1.	Structural characterizations	45
5A. 2.	Microstructural characterizations	47
5A. 3.	Dielectric characterizations	49
5A. 4.	Conductivity properties as a function of frequency	53
5A. 5.	Discussion	54
REFERENC	CES	56
5B Inve	stigation of Structural, Electrical, and Dielectric Properties of Lead-Free (BiFeO <sub>3</sub> ) <sub>(1-x)</sub> -	_
(CaTiO <sub>3</sub> ) <sub>x</sub>	Ferroelectric Ceramics	57
5B. 1.	Structural characterization of calcined BFO and CTO	57
5B. 2.	Thermogravimetry analysis	57
5B. 3.	Sintering temperature difference of BFO and CTO and choosing the MWS technique	58
5B. 4.	Structural characterization of sintered $(BFO)_{(1-x)} - (CTO)_x$	60
5B. 5.	Structural tolerance factor (t)	62
5B. 6.	Microstructural characterization	62
5B. 7.	Elemental studies	64
5B. 8.	Conduction mechanisms in $(BFO)_{(1-x)} - (CTO)_x$ ceramics	65
5B. 9.	Dielectric properties	66
REFERENC	CES	68
5C Influ	nence of CTO on Structural, Microstructural, Electrical and Dielectric Properties of Bl	FO-
based Lea	nd-Free Ceramics Through Microwave Sintering	70
5C. 1.	Structural analysis	70
5C. 2.	Microstructural characterization	73
5C. 3.	Electrical properties of BFO-CTO ceramics	74
5C. 4.	Dielectric properties	77
REFERENC	CES	80
5D Stud	y of High-Energy Density in Lead-Free BiFeO3-CaTiO3 Relaxor-Ferroelectric Cerami	cs for
High-Tem	perature Energy Storage Applications	82

	5D. 1.	Structural analysis	82
	5D. 2.	Microstructural analysis	86
	5D. 3.	X-ray photoelectron spectroscopy (XPS)	87
	5D. 4.	Current-Voltage (I-V) characteristics	88
	5D. 5.	Frequency-dependent dielectric properties and dielectric relaxation behaviour of BFO-C	TO
	ceramics a	at room temperature	89
	5D. 6.	Temperature-dependent dielectric properties and relaxor ferroelectric behaviour of BFO	-CTO
	ceramics	93	
	5D. 7.	Polarization – Electric field (P-E) loops of BFO-CTO ceramics	95
RE	FERENCE	S	103
CH.	APTER - 6		106
SUI	MMARY A	ND CONCLUSIONS	107
LIS	T OF PU	BLICATIONS	110
LIS	T OF CON	FERENCE PRESENTATIONS	111
AW.	ARDS		113

## LIST OF FIGURES

Fig. 1.1 Representation of energy density versus power density of various energy systems	
along with their characteristic timescales.	2
Fig. 1.2 Applications of electrostatic energy storage capacitors.	4
Fig. 1.3 Schematic representation of perovskite structure	6
Fig. 1.4 The relationship between multiferroic and magnetoelectric materials	8
Fig. 1.5 Schematic of BFO crystal structure and ferroelectric polarization	9
Fig. 1.6 The structural layout of an electrostatic capacitor	11
<b>Fig. 1.7</b> Schematic view of energy storage and dipole alignment in dielectrics up on applying an electric field	11
Fig. 1.8 P–E curves for linear dielectrics (LD), FE, AFE, and RFE.	
Domains are shown in the insets of the schematic layout, which align with applying E.	13
Fig. 4.1 BiFeO <sub>3</sub> viscous solution before combustion	33
Fig. 4.2 CaTiO <sub>3</sub> viscous solution before combustion	33
Fig. 4.3 Schematic layout of BFO-CTO synthesis, processing, and characterization	34
<b>Fig. 4.4</b> Calcination profile of as-synthesized BFO and CTO powders at an optimized temperature condition	35
<b>Fig. 4.5</b> Resistance heating furnace used for calcination representing heating elements and alumina crucible.	35
Fig. 4.6 Green pellet with dimensions; diameter ~10 mm, thickness ~1 mm	37
Fig. 4.7 Relative green density and bulk density as a function of applied load	38
Fig. 4.8 Manual grinding using mortar and pestle	38
Fig. 4.9 Green pellet making using uniaxial compaction setup and die	38
Fig. 4.10 Binder burnout and microwave sintering profile for optimized sintering	
temperature conditions of (1-x)BFO- xCTO	40
Fig. 4.11 Microwave sintering furnace setup and sample loading in SiC susceptor	40
Fig. 4.12 Flow chart for synthesis, and processing of BFO-CTO	41

<b>Fig. 4.13</b> Comparison between resistance furnace sintering (RFS) and microwave sintering (MWS) techniques and optimization of sintering temperature conditions of $(1-x)$ BFO- $x$ CTO ( $x = 0.6, 0.7, \text{ and } 0.8$ )	g 42
Fig 5A. 1 XRD patterns of calcined powders of BFO, BZO and sintered pellet	
of BFO-BZO	45
Fig 5A. 2 XRD patterns of calcined powders of BFO, CTO and sintered pellet of	
BFO-CTO	46
Fig 5A. 3 XRD patterns of calcined powders of BFO, STO and sintered pellet of	
BFO-STO	46
Fig 5A. 4 XRD patterns of sintered pellets of BFO-BZO, BFO-CTO and BFO-STO	47
Fig 5A. 5 Microstructure of the fractured surface of the sintered pellets of BFO-BZO.	
The respective inset shows the mean grain size and the distribution of grain sizes in the sintered pellets.	47
Fig 5A. 6 Microstructure of the fractured surface of the sintered pellets of BFO-CTO.	
The respective inset shows the mean grain size and the distribution of grain sizes in the sintered pellets.	48
Fig 5A. 7 Microstructure of the fractured surface of the sintered pellets of BFO-STO.	
The respective inset shows the mean grain size and the distribution of grain sizes in the sintered pellets.	48
<b>Fig 5A. 8</b> Frequency dependence of the dielectric constant and loss tangent for BFO-BZO sample sintered at 1100 °C/2h	50
Fig 5A. 9 Variation in dielectric constant and loss tangent as a function of frequency for	
the sintered BFO-CTO sample.	51
Fig 5A. 10 Low frequency, up to 1 MHz, dielectric behaviours of sintered BFO-CTO	
sample	52
Fig 5A. 11 Frequency dependent dielectric constant and loss tangent variation for the	
sintered (1100 °C/2h) BFO-STO sample	53

Fig 5A. 12 Frequency dependence of room temperature A.C. conductivity of the sintered	
BFO-BZO, BFO-CTO and BFO-STO samples. 3 labels of data points of each of the	
sample indicate that the estimated conductivity from the dielectric data has been collected	
from 3 different Impedance Analyzer to cover the entire frequency range	54
Fig 5B. 1 X-ray diffractogram of calcined (a) BFO and (b) CTO powder samples	57
Fig 5B. 2 Thermogravimetric analysis (TGA) of $(BiFeO_3)_{(1-x)} - (CaTiO_3)_x$ ceramics:	
(a) $x = 0.6$ and (b) $x = 0.8$	58
Fig 5B. 3 FESEM micrographs of (BiFeO <sub>3</sub> ) <sub>(1-x)</sub> – (CaTiO <sub>3</sub> ) <sub>x</sub> conventional sintered samples	
(a) $x = 0.6$ , and (b) $x = 0.8$	59
Fig 5B. 4 Relative sintered density of (BiFeO <sub>3</sub> ) (1-x) – (CaTiO <sub>3</sub> ) x, MWS vs RFS for	
(a) $x = 0.6$ , (b) $x = 0.7$ , and (c) $x = 0.8$ .	59
<b>Fig 5B. 5</b> Rietveld refined analysis results of X-ray diffraction pattern of (BiFeO <sub>3</sub> )(1-x) – (CaTiO <sub>3</sub> )x, (a) $x = 0.6$ , (b) $x = 0.7$ , and (c) $x = 0.8$ . (d) Merged and broadened XRD	
pattern in the vicinity of 32°	61
<b>Fig 5B. 6</b> Tolerance factor of (BiFeO <sub>3</sub> ) $(1-x) - (CaTiO_3) x (x = 0, 0.6, 0.7, and 0.8)$	
ceramics as a function of x.	62
Fig 5B. 7 FESEM micrographs of (BiFeO <sub>3</sub> )(1-x) – (CaTiO <sub>3</sub> )x microwave sintered samples	3
(a) $x = 0$ , (b) $x = 0.6$ , (c) $x = 0.7$ , and (d) $x = 0.8$ . The inset shows the grain size	
distribution of the samples	63
<b>Fig 5B. 8</b> Elemental analysis of sintered (BiFeO <sub>3</sub> )(1-x) – (CaTiO <sub>3</sub> )x $(x = 0.6, 0.7 \text{ and } 0.8)$ ceramics	64
<b>Fig 5B. 9</b> Leakage current density as a function of electric field at room temperature for sintered (BiFeO <sub>3</sub> ) $(1-x) - (CaTiO_3) x$ samples with $x = 0, 0.6, 0.7$ and $0.8$	66
<b>Fig 5B. 10</b> Variation in electrical conductivity and resistivity of (BiFeO <sub>3</sub> )(1-x) – (CaTiO <sub>3</sub> )x ceramics as a function of electric field at room temperature for samples with $x = 0, 0.6, 0.7$ and $0.8$	
<b>Fig 5B. 11</b> Room temperature frequency dependent (a) dielectric permittivity (ε'), and	00
rig sis. ir room competature nequency dependent (a) dietectric permittivity (8), and	

(b) loss tangent (tan  $\delta$ ) of (BiFeO<sub>3</sub>)(1-x) – (CaTiO<sub>3</sub>)x ceramics with x = 0, 0.6, 0.7

and 0.8	67
Fig 5C. 1 The outcomes of Rietveld refinement analysis of the X-ray diffraction	
pattern of $(BFO)_{(1-x)}$ – $(CTO)_x$ , (a) $x = 0$ , (b) $x = 0.1$ , (c) $x = 0.3$ , (d) $x = 0.5$ , and	
(e) $x = 1$ (f) Enlarged XRD pattern in the vicinity of $32^{\circ}$	71
Fig 5C. 2 Schematic visualization of $(BFO)_{(1-x)}$ – $(CTO)_x$ ceramics for (a) $x = 0.1$ ,	
(b) 0.5, and (c) distorted perovskite structure.	72
Fig 5C. 3 Surface morphology of $(BFO)_{(1-x)}$ – $(CTO)_x$ microwave sintered samples:	
(a) $x = 0$ , (b) $x = 0.1$ , (c) $x = 0.3$ , (d) $x = 0.5$ , and (e) $x = 1$ . The inset graphs show the	
grain size distribution of the samples.	74
<b>Fig 5C. 4</b> Electrical resistivity and conductivity of $(BFO)_{(1-x)} - (CTO)_x$ ( $x = 0, 0.1, 0.3, 0.3$ and $x = 1$ ) ceramics as a function of the electric field at room temperature.	5,
(a) Resistivity and (b) Electrical conductivity.	75
Fig 5C. 5 The variation of leakage current density with respect to the applied electric field	1
at room temperature of microwave sintered (BFO)(1-x) – (CTO)x (x = $0$ , 0.1, 0.3, 0.5,	
and $x = 1$ ) samples.	76
<b>Fig 5C. 6</b> Frequency-dependent (a) dielectric constant, and (b) loss tangent ( $\tan \delta$ ) of (BFO)(1-x) – (CTO)x (x = 0, 0.1, 0.3, 0.5, and x = 1) ceramics.	77
Fig 5C. 7 Temperature-dependent dielectric constant (εr) of (BFO)(1-x) – (CTO)(x)	
samples measured at 20 kHz – 10 MHz and Curie-Weiss law fitting as shown in the inset	
of figures (a) $x = 0.1$ , (b) $x = 0.3$ , and (c) $x = 0.5$	79
<b>Fig 5D. 1</b> Structural, microstructural and XPS results. (a) Refinement analyzed results of XRD for 0.7 of x. (b) Schematic geometrical visualization of Ti-Ti plane. (c) FESEM micrograph for 0.7 of x, inset shows the grain size distribution. (d) XPS fitting results for chemical valence states of Fe	82
Fig 5D. 2 Refinement analyzed results of XRD for 0 of x (a), 0.6 of x (b), 0.8 of x (c),	02
1 of x (d), and (104), (110) peaks shifting, broadening, and merging in the vicinity of 33°.	83
2 22 12 (27) and (10 1); (110) points smithly of 33 .	

<b>Fig 5D. 3</b> Schematic geometrical visualization of the Ti-Ti plane and Fe-Fe plane of (1-x)	
BFO – $x$ CTO ( $x = 1, 0.8, 0.6, and 0$ )	85
<b>Fig 5D. 4</b> FESEM micrographs of fractured surface for (a) $x = 0$ , (b) $x = 0.6$ , (c) $x = 0.8$ of and (g) $x = 0.7$ . The surface morphology for (a) $x = 0$ , (b) $x = 0.6$ , and (c) $x = 0.8$	,
insets show the grain size distribution	86
Fig 5D. 5 XPS results of BFCT ceramics for chemical valency states of Fe	88
Fig 5D. 6 Temperature-dependent current-voltage hysteresis curves for 0.6 of x	
(a). 0.7 of x (b). 0.8 of x (c).	88
<b>Fig 5D.</b> 7 Temperature-dependent current-voltage hysteresis curves for 0.6 of x (a), 0.7 of x (b), and 0.8 of x (c).	89
Fig 5D. 8 Temperature-dependent current-voltage hysteresis curves for 0 of x	89
Fig 5D. 9 Frequency-dependent dielectric properties. $\varepsilon'$ and $\tan\delta$ for 0.6 of x (a),	
$0.7$ of x (b) and $0.8$ of x (c). Different plot colours represent different frequency ranges recorded using different impedance analyzers. (d) Cole-Cole distribution of dielectric relaxation times of $\varepsilon'$ and $\varepsilon''$ for x = 0.6, 0.7 of x (e) and 0.8 of x (f)	90
<b>Fig 5D. 10</b> Frequency-dependent ε' and tanδ for 0 of x, different plot colours represent different frequency ranges recorded using different impedance analyzers	91
<b>Fig 5D. 11</b> Cole-Cole distribution of dielectric relaxation times of $\varepsilon'$ and $\varepsilon''$ for (a) $x = 0$ , (b) $x = 0.6$ , (c) $x = 0.7$ , and (d) $x = 0.8$	92
<b>Fig 5D. 12</b> Temperature-dependent dielectric permittivity of (1-x) BFO – x CTO ceramics measured at 10kHz – 10MHz and the corresponding Curie-Weiss law fitting for	
x = 0.6 (a), 0.7 of x (b) and 0.8 of x (c)	94
Fig 5D. 13 Temperature-dependent $\varepsilon_r$ and $\tan\delta$ for 0.7 of x	95
<b>Fig 5D. 14</b> (a) Temperature-dependent P-E loops at a field of 33.33 kV cm <sup>-1</sup> for 0.7 of x. (b) Time-dependent P-E loops at an electric field of 33.33 kV cm <sup>-1</sup> for 0.7 of x. (c) Variation of electric field-dependent P-E curves measured at a period of 40 ms for 0.7 of x.	•
(d) $W_{rec}$ , $W_{loss}$ , schematic representation at an electric field of 66.66 kV cm <sup>-1</sup> at a period of 140 ms.	96

Fig 5D. 15 (a) Temperature-dependent P-E loops at an electric field of 33.33 kV cm-1 (b)	
Time-dependent P-E loops at an electric field of 33.33 kV cm <sup>-1</sup> (c) Time-dependent P-E	
loops at an electric field of $66.66 \text{ kV cm}^{-1}$ (x =0.7 in all cases).	96
Fig 5D. 16 (a) Variation of temperature-dependent Wrec, Wloss, Pmax, and $\eta$ for 0.7 of x	
at an electric field of 33.33 kV cm <sup>-1</sup> . (b) Variation of time-dependent Wrec, Wloss, Pmax,	
and $\eta$ for 0.7 of x at an electric field of 33.33 kV cm <sup>-1</sup> .	97
Fig 5D. 17 Variation of time-dependent $W_{rec}$ , $W_{loss}$ , $P_{max}$ , and $\eta$ for 0.7 of x at an electric	
field of 66.66 kV cm <sup>-1</sup>	98

## LIST OF TABLES

Table 1.1 Comparison between capacitors and batteries' energy storage, power density           and charging rates	3
<b>Table 5A. 1</b> Dielectric properties of BFO-BZO, BFO-CTO and BFO-STO at $f = 10 \text{ kHz}$ and $10 \text{ MHz}$	54
<b>Table 5B. 1</b> Elemental analysis of the sintered samples of (BiFeO <sub>3</sub> ) $(1-x) - (CaTiO_3) x$ , $(x = 0.6, 0.7, and 0.8)$	64
<b>Table 5C. 1</b> Structural parameters of $(1-x)$ BFO $-x$ CTO yielded by the Rietveld refinement of the XRD results.	72
Table 5C. 2 Angles between the atoms	73
<b>Table 5C. 3</b> Frequency-dependent dielectric properties of the sintered $(BFO)_{(1-x)}$ — $(CTO)_x$ samples for $x = 0, 0.1, 0.3, 0.5,$ and 1	78
<b>Table 5D. 1</b> Structural parameters of $(1-x)BFO - xCTO$ yielded by the Rietveld refinement of the XRD results.	nt 84
<b>Table 5D. 2</b> Angles between planes and atoms yielded from the geometrical representation of (BiFeO3) $(1-x) - (CaTiO3)(x)$ for $x = 0, 0.6, 0.7, 0.8$ and 1	n 85
<b>Table 5D. 3</b> I-V characteristics of (1-x) BFO-x CTO ceramics	89
<b>Table 5D. 4</b> Dielectric relaxation times yielded by cole-cole distribution fittings within the frequency range $16 \text{ kHz} \le f \le 20 \text{ MHz}$ .	e 93
<b>Table 5D. 5</b> Dielectric relaxation times yielded by cole-cole distribution fittings within the frequency range 1 MHz $\leq$ f $\leq$ 3 GHz	e 93
<b>Table 5D. 6</b> Recoverable energy density $(W_{rec})$ , loss $(W_{loss})$ , efficiency $(\eta)$ and maximum polarization (Pmax) for $x = 0.7$	99
<b>Table 5D. 7</b> Comparison of maximum temperature sustainability and $W_{rec}$ between the present work and previous reports on bulk ceramics	99
Table 5D. 8 Comparison of W <sub>rec</sub> between previous reports and present work based on the	
thickness of the bulk ceramics	100

## Nomenclature

ω	Agular frequency
$\epsilon_{r}$	Dielectric constant
$tan\delta$	Loss tangent
$\epsilon_0$	Permittivity of free space (N-m <sup>2</sup> /kg <sup>2</sup> )
a, b, c	Lattice constants (Å)
$r_A$	A site average ionic radius (Å)
E	Electric field (v/cm)
f	Frequency (Hz)
$E_{c}$	Coercive field
$r_{o}$	Oxygen ionic radius (Å)
P	Polarization
$P_{m}$	Maximum polarization
$\mathbf{P}_{\mathbf{r}}$	Remnant polarization
ρ	Resistivity (Ω cm)
J	Current density (A/cm <sup>2</sup> )
$T_{c}$	Curie temperature (°C)
τ	Mean dielectric relaxation time
η	Efficiency
t	Sample thickness (mm)
$T_{m}$	Maximum temperature
γ	Degree of diffusivity
Q	Charge (C)
D	Dielectric displacement

#### Nomenclature

dq Incremental charge

W<sub>rec</sub> Recoverable density

W<sub>loss</sub> Energy loss during discharging

T Tolerance factor

ε' Real part of dielectric permittivity

 $\chi^2$  Goodness of the fit

### **Abbreviations**

LD Linear Dielectrics

FE Ferroelectrics

RFE Relaxor Ferroelectrics

AFE Anti-Ferroelectrics

BFO BiFeO<sub>3</sub>

CTO CaTiO<sub>3</sub>

EDX Energy Dispersive X-Ray Spectrum

FESEM Field Emission Scanning Electron Microscope

XRD X-Ray Diffraction

SMES Superconducting Magnetic Energy Storage

ECs Electrochemical Capacitors

ESD Energy Storage Device

SOFCs Solid Oxide Fuel Cells

EMP Electro-Magnetic Pulse

PE Para Electric

PNRs Polar Nano Regions

BDS Breakdown Strength

MLCC Multilayer Ceramic Capacitor

DCs Dielectric Capacitor

BST BaSrTiO<sub>3</sub>

STO SrTiO<sub>3</sub>

BZO BaZrO<sub>3</sub>

SZO SrZrO<sub>3</sub>

#### **Abbreviations**

BTO BaTiO<sub>3</sub>

PZT PbZrTiO<sub>3</sub>

TBT Tetrabutyl Titanate

RSD Relative Sintered Density

RGD Relative Green Density

IPA Isopropyl Alcohol

PVA Polyvinyl Alcohol

XPS X-Ray Photoelectron Spectrometer

TG Thermogravimetry

#### **CHAPTER - 1**

#### INTRODUCTION

#### 1.1 Significance of energy

As the global population continues to expand at an unprecedented rate and the global economy thrives, there is a similar surge in energy consumption worldwide. To put this into perspective, the world's total energy consumption substantially increased from 54,207 terawatt-hours (TWh) in 1973 to a staggering 111,125 TWh in 2016 [1]. However, this surge in energy demand brings forth many challenges that cannot be overlooked. One of the most pressing concerns is the detrimental impact of energy consumption on the environment. High CO, CO<sub>2</sub> levels, air pollution, and the exhaustion of fossil fuel reserves are all significant issues that need urgent attention. Considering these problems, it becomes evident that tapping into various green and regenerative energy sources is the most promising resolution [2-5]. Regenerative sources, like solar, wind, and geothermal energy, are gradually gaining dominance in the energy landscape, aiming to replace the reliance on fossil fuels [1]. Nevertheless, the transition to renewable energy sources is not without its hurdles. One significant challenge lies in the intermittent nature of most renewable energy sources. Unlike traditional fossil fuels that provide a consistent energy supply, renewables fluctuate in their generation capacity, which poses difficulties in effectively harnessing their full potential. To overcome this hurdle, converting renewable energy, primarily into electricity, a versatile and widely usable form of energy, is imperative. This conversion process necessitates deploying efficient and reliable electrical energy storage solutions. These energy systems are important to ensure that the electricity generated from renewable sources can be effectively captured, stored, and utilized when needed [2, 6-10]. The demand for energy continuously increasing day by day as the world population surges. As the population grows the global economy expands with many environmental challenges. In order to address the environmental problems associated with currently using conventional energy resources, there is a dire need to move towards green and regenerative energy resources to overcome the environmental issues that the globe is facing currently. Moreover, in order to unlock the capability of renewable energy and assure a sustainable and effective energy future, it is most important to develop reliable electrical energy storage systems that can accommodate the intermittent behaviour of most renewable resources.

#### 1.2 Types of energy storage systems

There are different types of energy storage systems, and each one of them has its own advantages and disadvantages. Batteries are impressive in storing a lot of energy, but their discharge rates are low. Flywheels can store a lot of energy and discharge it quickly, but they are more expensive. Superconducting Magnetic Energy Storage (SMES) systems possess high efficiency (η) however, they are also not within the affordable making cost. Electrochemical Capacitors (ECs) offer a good balance of energy and power density. But they are not as efficient as batteries at storing a large amount of energy even though their discharging rate is high. ECs are also relatively inexpensive. Dielectric capacitors and electrostatic energy storage capacitors are better suited for high-power applications. This makes them best suitable for applications where pulsed power is required. In between these extreme strengths and weaknesses, ECs deliver a middle ground, by balancing between energy and power densities. But failed to match the energy storage strengths of batteries or fuel cells, though they offer the advantage of more rapid energy discharge rates than dielectric capacitors. However, they operate at lower voltages, generally < 3 V, which restricts their applications. Moreover, they experience a remarkable leakage current, measured in mA, which can affect their overall efficiency (n) [11-12]. In contrast, electric capacitors, including dielectric and electrostatic capacitors, are best-suitable for high-power applications. They are cost-effective for large-scale power density requirements.

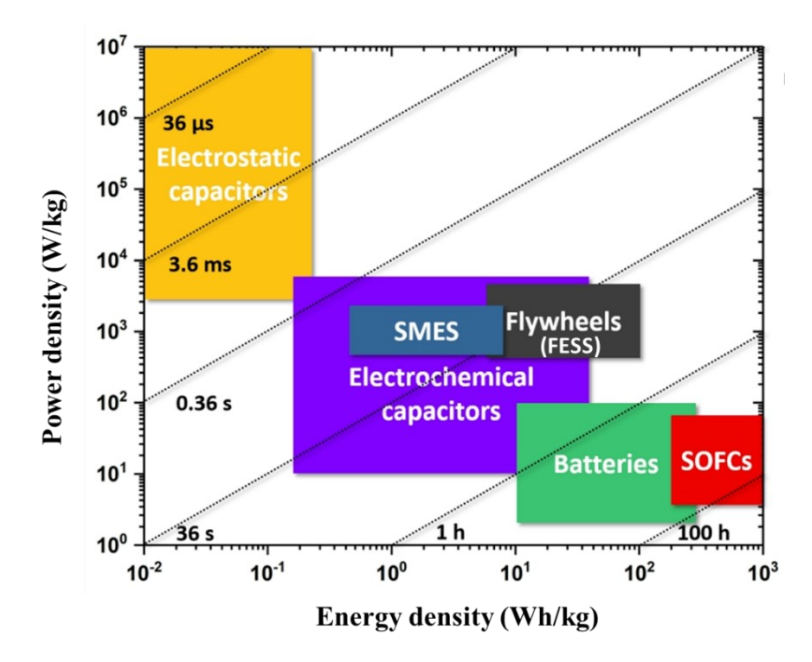


Fig. 1.1 Representation of energy density versus power density of various energy systems along with their characteristic timescales.[13]

To effectively assess and compare the performance of different energy storage devices, the Ragone plot assumes a crucial role. It is a valuable benchmarking tool by providing a graphical representation of energy and power densities. The Ragone plot enables researchers and engineers to evaluate the capabilities of various energy storage technologies and make informed decisions based on their specific energy and power requirements, as illustrated in Figure 1.1.

Table 1.1 Comparison between capacitors and batteries' energy storage, power density and charging rates

Capacitors	Batteries
The low energy density (~ 10 -2 - 10 -1 Wh/kg)	The high energy density (10 - 100 Wh/kg)
High power density (5.103 - 108 W/kg)	Low power density (5 - 500 W/kg)
Fast charging (~ s)	Long charging (~ h)
Electrostatic storage	Electrochemical storage

#### 1.3 Electrochemical energy storage

Each electrochemical energy storage device (ESD) must possess a combination of high and high-power density, making them capable of storing significant energy while delivering it rapidly when needed. The suitability of each ESD depends on its characteristic time [14], as determined by factors such as charge/discharge rate, which are showcased by dashed lines in Figure 1.1. It is essential to bear in mind that external factors, including load resistance, can influence the appropriate charge or discharge rates of the ESD. Figure 1.1 illustrates the comparative performance of capacitors, batteries, and solid oxide fuel cells (SOFCs) regarding charge/discharge rates and power density.

#### 1.4 Capacitors and perovskite ceramics applications

Capacitors outperform electrochemical energy systems and fuel cells in these aspects. Capacitors can store energy by means of redistributing bound charged elements, while electrochemical energy devices and fuel cells store energy through chemical transformations. This fundamental difference accounts for the superior charge or discharge times. Due to their remarkable characteristics, capacitors are employed in various applications. Perovskite ceramics with excellent ferroelectric, paraelectric and particularly high-frequency dielectric properties are suitable for various high-temperature and high-frequency applications. In bulk

form, they may be used as dielectric resonators and filters in communication devices [15, 16], as window sections in microwave windows in fusion reactors [17, 18], or as high-power antennas in pulsed power transmitters [19, 20], where high relative permittivity ( $\varepsilon_r$ ), high-quality factor ( $Q_f$ ), very low dielectric losses ( $tan\delta$ ) and a highly low-temperature coefficient of resonant frequency ( $\varepsilon_r$ ) are the most important material properties. In film form, they may be used in high-frequency capacitor applications, such as decoupling capacitors and tunable microwave capacitors [21, 22]. Capacitor dielectrics are also used in advanced packaging applications [23, 24]. Since the dielectric constant may be strongly dependent on voltage, permittivity tailored thin film capacitor dielectrics find extensive application in tunable devices, including low-cost phase shifters for phased array antennas and tunable oscillators, as well as tunable filters for wireless applications [21]. The usage of energy storage systems is increasing day by day in electrical and electronic devices, viz., in hybrid electric vehicles, pulsed power systems and high-frequency inverters [25]. Moreover, capacitors are particularly suited for high-power applications like fusion, as illustrated in Figure 1.2. These examples demonstrate the diverse applications and significance of capacitors across multiple domains.

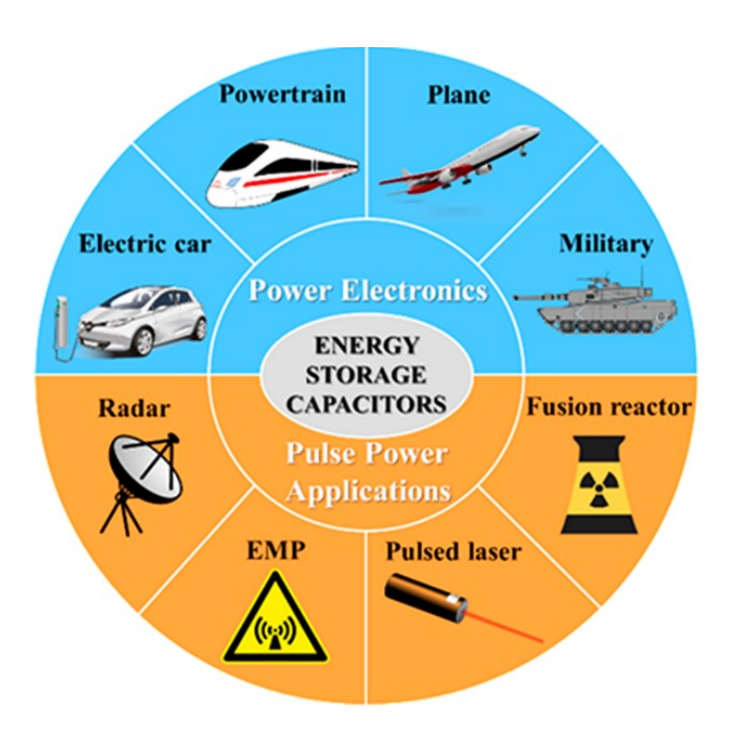


Fig. 1.2 Applications of electrostatic energy storage capacitors. (EMP: electromagnetic pulse)

Different applications necessitate the utilization of capacitors with distinct characteristics tailored to their specific requirements. To illustrate this point, consider the field of microwave communications, where capacitors must possess an exceptionally high-quality factor characterized by minimal dielectric loss. On the other hand, in decoupling circuits,

capacitors are expected to exhibit a substantial capacitance per unit volume. One dielectric capacitor, displays rapid charge/discharge rates, as indicated by its short characteristic time in Figure 1.1. However, it is important to highlight that the dielectric capacitors have a relatively low energy density, as depicted in Figure 1.1 [26]. Researchers have been exploring the development of high-energy density to overcome these limitations. By incorporating such materials, the volume of the capacitor can be significantly reduced, thereby increasing its volumetric efficiency. This advancement holds great potential for various applications prioritizing miniaturization, lightweight design, affordability, and seamless integration [12, 26].

#### 1.5 Perovskite

In the context of perovskite structure, the chemical formula used to represent them is ABO<sub>3</sub>, where A and B are the cations, and O is an anion. Among all the perovskites, oxide perovskites (defined as ABO<sub>3</sub> where O is oxygen anion) are in the limelight because there is a strong interest in this topic because it combines technology and captivating physics. In perovskites, the ionic size of B- site cations are smaller than that of A-site cations. In an ideal perovskite, the cube's corner positions (called A- site) are usually occupied by A cations. In contrast, body center positions (called B-site) are occupied by B cations, and oxygen ions O rest on face centres of the cube, as shown in Figure 1.3. The cations at A-site can be monovalent (Na<sup>1+</sup>, Ag<sup>1+</sup>, K<sup>1+</sup>, etc.), divalent (Pb<sup>2+</sup>, Ca<sup>2+</sup>, Ba<sup>2+</sup>, Sr<sup>2+</sup>, etc.), or trivalent (Bi<sup>3+</sup>, La<sup>3+</sup>, Ho<sup>3+</sup>, etc.) and accordingly, the B-site cations can be pentavalent (W<sup>5+</sup>, Ta<sup>5+</sup>, Nb<sup>5+</sup>, etc.), tetravalent (Ti<sup>4+</sup>, Mn<sup>4+</sup>, Co<sup>4+</sup>, etc.), or trivalent (Fe<sup>3+</sup>, Sc<sup>3+</sup>, Mn<sup>3+</sup>, etc.), respectively. Although, the ideal perovskite structure is cubic, actual perovskite structures deviate from cubic structure due to the distortion. The degree of distortion can be accounted for using the Goldschmidt tolerance factor (t) defined as [27]

$$t = \frac{\left[ (1-x)R_{Bi^{3+}} + xR_{Ca^{2+}} + \frac{1}{R_{O^{2-}}} \right]}{\sqrt{2[(1-x)R_{Fe^{3+}} + xR_{Ti^{4+}} + R_{O^{2-}}]}}$$

- r<sub>A</sub> represents the ionic radius of the A-site
- r<sub>B</sub>, represents the ionic radius of the B-site
- r<sub>O</sub> represents the ionic radius of oxygen ions

For cubic perovskite, t is equal to 1. In most cases, t ranges from 0.8 to 1.

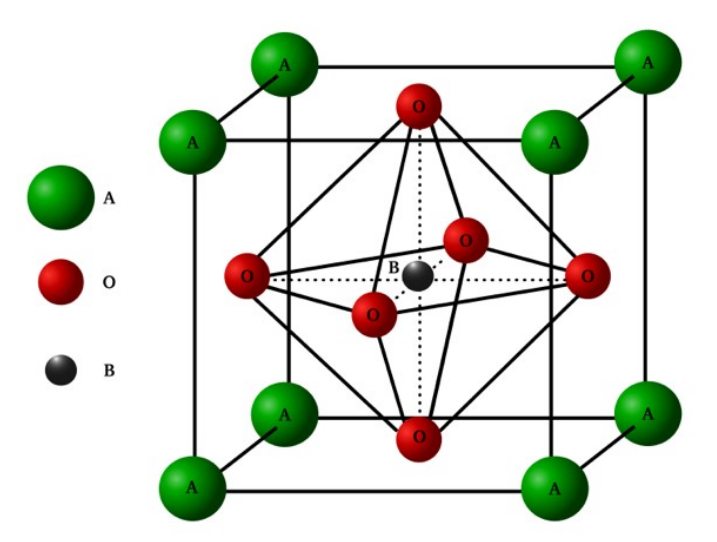


Fig. 1.3 Schematic representation of perovskite structure

The size difference between the A-site cation and B-site cation (t < 1) leads to distortion and tilts in the oxygen octahedra to fit the lattice cations. The octahedral tilts are the most common distortions [28-30]

#### 1.6 Ferroelectricity

The phenomenon of ferroelectricity was discovered in 1921 by Valasek in single-crystal Rochelle salt [31]. Out of twenty-one non-centrosymmetric point groups, ten-point groups exhibit one unique polar axis and deliver a pyro-electric effect, i.e., generation of electric polarization due to the application of thermal energy. All the pyro-electric materials are also piezoelectric, but the converse is invalid. Electric polarization can be switched in some pyroelectric materials by applying electric field. These materials are called ferroelectric (FE) materials. Thus, the necessary condition for a material to classify as a FE is (i) it should have a spontaneous polarization and (ii) the direction of P can be switched with the applied E. All FEs are Para electric (PE), but not vice-versa. In FE materials, there are small regions of uniform polarization called ferroelectric domains. In each FE domain, all the dipoles are oriented in the singular direction. Each electric domain is separated by an interface called a domain wall. The distinctive character of FE materials can be seen as a hysteresis curve in the P versus E curve. The hysteresis loop shows a net spontaneous polarization even without an electric field, and spontaneous polarization disappears at a temperature called  $T_{\rm C}$ , which signifies a temperature at which the material undergoes a transition from a PE state, characterized by high temperature, to a ferroelectric state at lower temperatures. In the PE state, the dielectric constant of ferroelectric material obeys Curie-Weiss law as given below.

$$\frac{1}{\varepsilon_r} - \frac{1}{\varepsilon_m} = \frac{(T - Tm)^{\gamma}}{C}$$

- C represents the Curie-Weiss constant
- $T_m$  represents the maximum temperature
- $\varepsilon_m$  represents the dielectric permittivity at  $T_m$
- $\gamma$  is the degree of diffusivity ( $1 \le \gamma \le 2$ ), 1 represents normal FE and 2 illustrates ideal relaxor ferroelectrics (RFEs).

The dielectric constant ( $\epsilon$ ) is large for an excellent FE material. The equation relates the  $\epsilon$  and electric polarizability (P),

$$P = \chi \varepsilon E$$

where  $\chi$  is the electrical susceptibility. In most FE materials below  $T_{\rm C}$ , such as BaTiO<sub>3</sub>, the ferroelectricity originated due to the off-centring of (Ti<sup>4+</sup>) cations relative to the (O<sup>2-</sup>) anions. The partial overlapping of the empty d orbital of the Ti<sup>4+</sup> ion with the 2p orbital of the oxygen ion forms the covalent bond and breaks the inversion symmetry. Above  $T_{\rm C}$ , the possibility of the off-centring of cations is lost, hence the ferroelectricity's disappearance in the material. Above  $T_{\rm C}$ , the material is said to be para electric. The lone pair mechanism is the origin of spontaneous polarization in PbTiO3 or BiFeO3. The valency  $6s^2$  electrons of Pb<sup>2+</sup> (or Bi<sup>3+</sup>) ions form hybridization with the 6p orbital of Pb<sup>2+</sup> (or Bi<sup>3+</sup>) and 2p orbital of oxygen [32, 33]. Due to this hybridization, the cations displace relative to the anions, hence the ferroelectricity.

In anti-ferroelectric (AFE) materials, the dipoles are aligned in antiparallel direction; Therefore, they lack any intrinsic spontaneous polarization. An example of an AFE material is the perovskite PbZrO<sub>3</sub> compound. It has recently been reported that at room temperature, The PbZrO<sub>3</sub>-based ceramics that have been chemically altered can exist in either an AFE or FE state, contingent upon their thermal background [34]. In these ceramics, the FE phase can be prompted using an electric field, resulting in a metastable condition that persists even after the field has been disconnected.

#### 1.6.1 Multiferroics

Multiferroics are materials that simultaneously possess at least two kinds of ferroics orders. H. Schmid is acknowledged for introducing the term multiferroic into the scientific literature in 1994 [35]. A ferroic order is described as a spontaneous order that forms small domain regions. Within each domain, the order parameter has a definite sign or direction. An

application of an appropriate field can switch the domain to align in the direction of the field. The term multiferroics is commonly associated with magnetic ferroelectrics. The ability to combine magnetic and ferroelectric properties in one material and its potential functionality has resulted in early work on multiferroics [36]. However, combining these two properties has proven to be complicated. Although many materials exhibit magnetic and ferroelectric properties, ferromagnetic and ferroelectric order parameters are mutually exclusive. The relationship between multiferroic and magnetoelectric materials is illustrated in Figure 1.4.

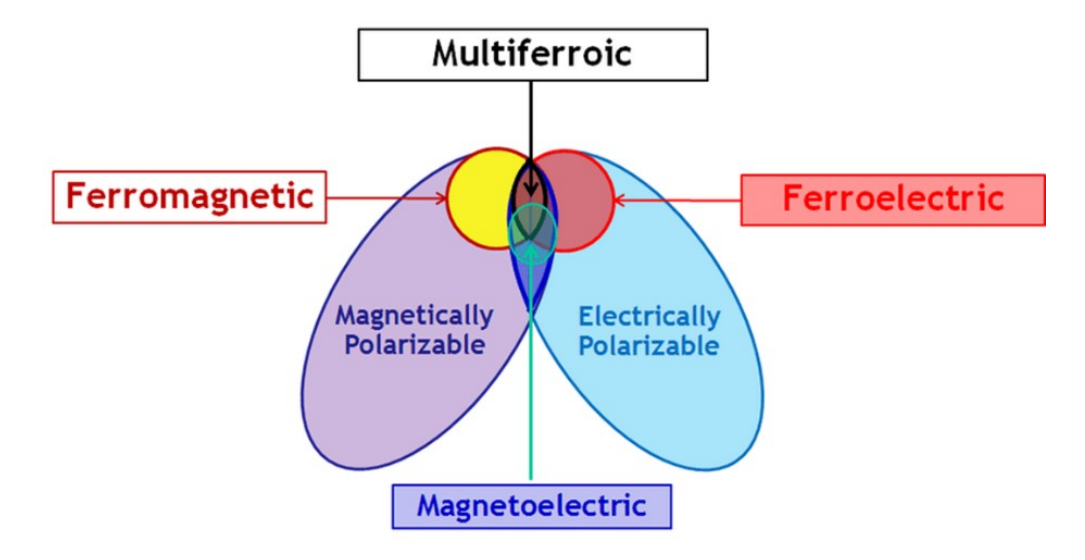


Fig. 1.4 The relationship between multiferroic and magnetoelectric materials [Ref: 10.1002/9781118935743.ch25]

#### 1.7 Bismuth ferrite

BiFeO<sub>3</sub> (BFO) is the most promising and widely studied multiferroic material [37, 38]. It exhibits FE and anti-ferromagnetic (AFM) properties in a similar phase at ambient temperature. It has ferroelectric  $T_{\rm C} = 1103$  K and  $T_{\rm N} = 643$  K. Bi<sup>3+,</sup> and Fe<sup>3+</sup> ions are responsible for the ferroelectric and magnetic properties of BFO, respectively.

#### 1.8 Crystal structure of BFO

The determination of the crystal structure of BFO was carried out by Michel et al. [39] in 1969, employing X-ray diffraction on a single crystal and neutron diffraction on BFO powder. The diffraction peaks of BFO indexed to the Rhombohedral crystal structure with R3c space group symmetry with no traceable impurity within the detection limit of powder XRD. The lattice parameters are a = 5.637 Å and  $\alpha = 59.344^{\circ}$  [40]. The ideal, cubic perovskite structure is also regarded as an aristotype, as shown in Figure 1.5. In the perovskite structure, Fe<sup>3+</sup> ions are located inside an O<sub>6</sub> anion, and Bi<sup>3+</sup> ions are situated at the corner positions. In BFO, the positions occupied by Bi<sup>3+</sup> and Fe<sup>3+</sup> ions are called A-site

and B-site, respectively. The coordination number of A, B-site ions and  $O^{2-}$  ions is 12, 6, and 6 respectively. If the coordination number of A-site ionic size is too small to fill the voids between the BO<sub>6</sub> octahedra, the oxygen octahedral will be tilted to reduce the size of the dodecahedron, and simultaneously A-site ions, which leads to the distortion in the perovskite structure. The crystal structure distortion in terms of ionic size can be studied using Goldschmidt tolerance t. The crystal structure distortion changes the Fe-O-Fe bond angle and Fe-O bond distances, changing the magnetic exchange interactions. And, large displacement of Bi ions relative to the FeO<sub>6</sub> octahedra results in ferroelectricity in BFO. The FE polarization points along the cubic diagonal direction <111>, as shown in Figure 1.5, which leads to eight possible polarization variants.

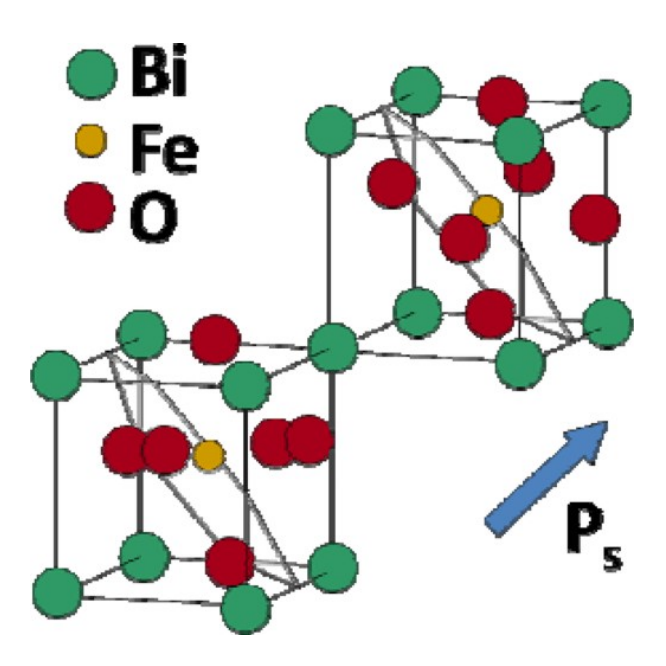


Fig. 1.5 Schematic of BFO crystal structure and ferroelectric polarization (shown by an arrow) and antiferromagnetic ordering (shown in the grey plane) [41]

#### 1.9 Ferroelectric properties

In BFO, ferroelectricity results from the process of blending the stereochemical active Bi 6s² lone pair electrons with the unoccupied 6p⁰ orbital of the Bi³+ ion and the 2p⁶ state of O²- ions have been observed [30]. Theoretical computations have predicted that the movements of cations result in substantial spontaneous polarization [42]. Owing to the presence of active lone pair electrons, Bi ions exhibit comparatively more significant displacements when compared to Fe ions. The high ferroelectric Curie temperature usually refers to the high ferroelectric polarization. However, it is tough to characterize the ferroelectric properties of BFO due to its low electrical resistivity and leakage currents.

Oxygen defects and non-stoichiometric composition cause low resistivity and leakage currents. Recent polarization measurements on high-quality films, single crystals, and polycrystalline ceramics have shown that saturation polarizations are close to  $90 - 100 \,\mu\text{C}$  cm<sup>-2</sup>, in agreement with previous studies [43, 44]. Significant efforts have been undertaken to augment the ferroelectric characteristics of BFO by substituting and making solid solutions of BiFeO<sub>3</sub> with other ABO<sub>3</sub> perovskite materials [45 - 50].

#### 1.10 Electrostatic energy storage in Ceramics

#### 1.10.1 Electrostatic Capacitors

The fundamental structure of a dielectric capacitor is relatively straightforward, involving the arrangement of two metallic plates that run parallel to each other. These plates are separated by an insulating material, which serves as a barrier between them. When an electric field is applied to the capacitor, the insulator undergoes polarization, a phenomenon where its atoms or molecules align themselves in response to the electric field. This polarization behaviour is considered a defining characteristic of dielectric materials. It distinguishes them from other substances not exhibiting this property when subjected to an electric field. Dielectrics are specifically chosen for their ability to store electrical energy efficiently due to their polarized nature. To quantify the storage capacity of a dielectric capacitor, we refer to its capacitance, denoted as C. In an ideal capacitor, the value of C is determined by the ratio of the charge (Q) accumulated on each metallic plate to the applied voltage V. In simpler terms capacitance represents the amount of charge that can be stored on the plates for a given voltage level. This relationship between charge, voltage, and capacitance is fundamental to capacitor functionality, as shown by eq 1.

$$C = \frac{Q}{V}(F) \qquad \longrightarrow (1)$$

Nevertheless, considering a pragmatic perspective, a more valuable formula for calculating the capacitance of an authentic device is depicted in Figure 1.6,

- D (electric displacement)
- P (polarization)
- $\varepsilon_0$  (electric permittivity of free space)

by employing the Gauss law, the relation between the area (A), distance (d), voltage (V), and permittivity (ε) of the dielectric material is expressed in Equation 2

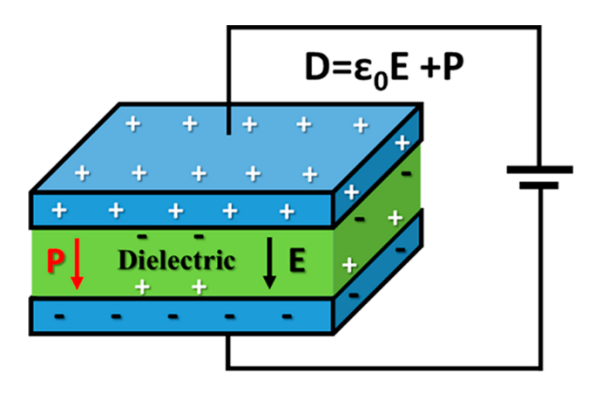


Fig. 1.6 The structural layout of an electrostatic capacitor

$$V = \frac{Qd}{\varepsilon A} \qquad \longrightarrow \qquad (2)$$

The combination of equations 1 and 2 can be modified as follows;

$$C = \frac{A}{\varepsilon d}(F) \longrightarrow (3)$$

Hence, equation 3 represents an explicit dependency of  $\varepsilon$  in energy storage dielectrics.

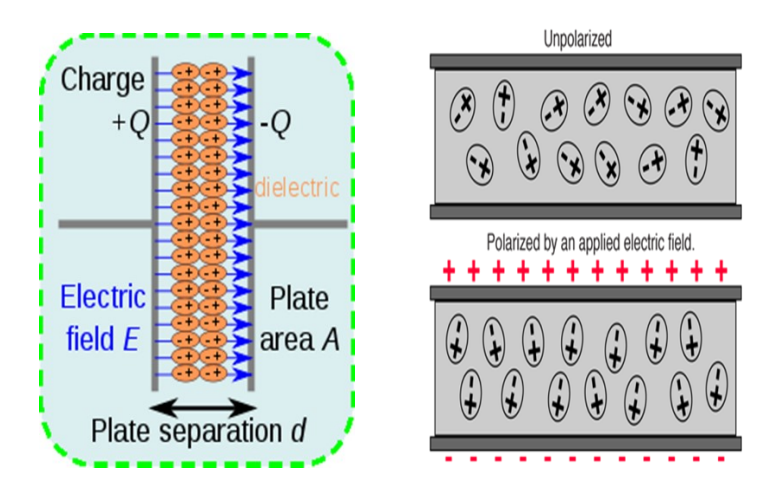


Fig. 1.7 Schematic view of energy storage and dipole alignment in dielectrics up on applying an electric field

#### 1.11 Crucial factors for assessing the properties of energy storage

Through the application of voltage (V), it is possible to estimate the electrostatic energy (W) stored within the dielectric material. This estimation allows for a quantification of the energy content resulting from the application of the voltage from the formula expressed as;

$$W = \int_0^{Q_{max}} V \ dq \ (J)$$

- Q<sub>max</sub> represents the maximum charge attained at the endpoint of the charging cycle
- dq represents the incremental charge.

The volumetric electrostatic energy density (W<sub>st</sub>) calculated from the equation (i.e., W/unit volume (Ad)) which can be represented as;

$$W_{st} = \frac{W}{A d} = \frac{\int_0^{Q_{max}} V dq}{A d} = \int_0^{D_{max}} E dD (J \text{ cm}^{-3})$$

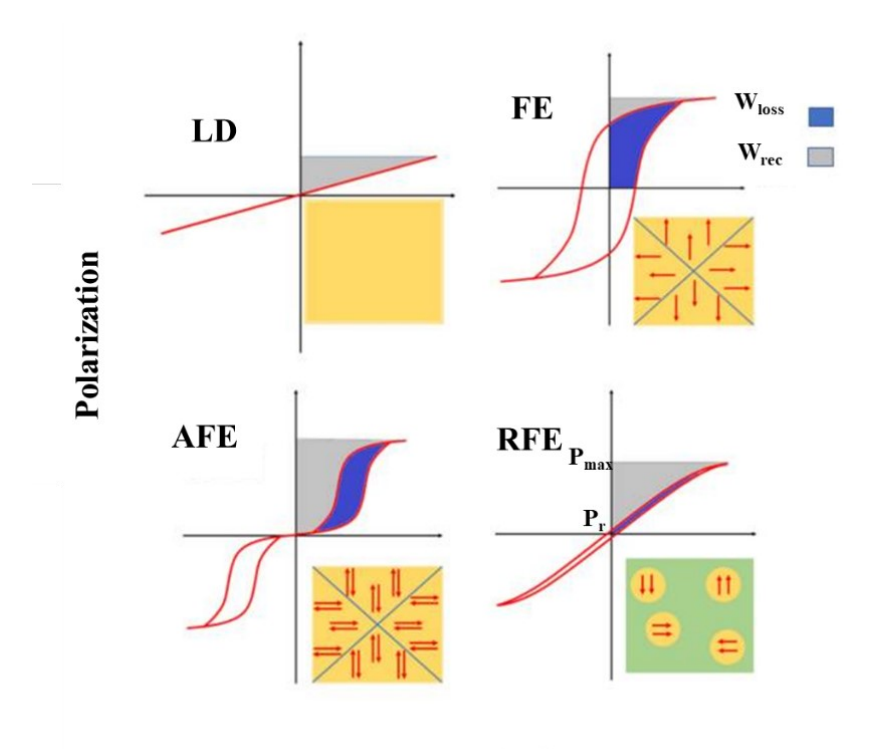
- E represents EF
- $D_{max}$  represents the electric displacement at  $E_{max}$

The electrical displacement (D) corresponds to the charge density (Q/A) on the metallic plates formulated as  $D = \varepsilon_0 E + P$  (shown in Figure 1.6), where P is the polarization. If  $\varepsilon >> \varepsilon_0 E$ , particularly for high  $\varepsilon$ ,  $D \sim P$ , and it follows that  $D = \varepsilon E = \varepsilon_0 \varepsilon_r E$ , (from permittivity of free space  $\varepsilon_0$  and relative permittivity  $\varepsilon_r$ ). These formulae permit the establishment of the static stored energy density by means of variable P,

$$W_{st} = \int_0^{E_{max}} E \varepsilon_0 \varepsilon_r \ dE$$

•  $P_{max}$  denotes maximum polarization at  $E_{max}$ 

Several experiment methods are carried out to calculate energy density from the P up on applied E. In 1961, Jaffe [51], in his analysis, drew attention to an essential aspect regarding recoverable energy ( $W_{rec}$ ). This energy is highlighted by the area located above the discharging P-E curve.  $P_{max}$  determines the upper limit of this area. To calculate  $W_{rec}$ , a mathematical integration is performed on the area above a P-E loop. This integration allows for a graphical visualization, as depicted in Figure 1.8, illustrating the  $W_{rec}$  for four distinct types of polarization response. This analysis provides valuable insights into the potential energy that can be recovered from the system and offers a comprehensive understanding of the different polarization behaviours exhibited.



**Electric field** 

Fig. 1.8 P–E curves for linear dielectrics (LD), FE, AFE, and RFE. Domains are shown in the insets of the schematic layout, which align with applying E. In RFEs, polar nano regions (PNRs) (represented in yellow circular regions) [52]

The  $W_{rec}$  is estimated from the given formula;

$$W_{\rm rec} = \frac{1}{2} \varepsilon_0 \varepsilon_r E^2$$

But when dealing with the LD materials, the  $\varepsilon_r$  remains unaffected by variations in E. From the above equation, the dependence of  $W_{rec}$  on the variables  $\varepsilon_r$  and E is clear from Figure 1.8, specifically FE, AFE, and RFE. Various scenarios are presented where the P responses deviate from linearity. Thus, the computation of  $W_{rec}$  necessitates the utilization of the above equation. Figure 1.8 for FE showcases a response that is commonly observed in classical ferroelectric (FE) materials, such as BT. In these materials, the hysteresis phenomenon is intricately connected to the polarization switching of macroscopic FE domains. This relationship is elaborated upon in detail in the review written by Damjanovic (53). Drawing from the insights of Jaffe (51), it was emphasized back in 1961 that in ferroelectrics, most of the charging energy is primarily absorbed through the process of domain switching. This absorbed energy is subsequently retained as  $P_r$ . Classical FEs tend to exhibit remarkably high levels of remanence. However, through the introduction of chemical doping, an effective means of minimizing this

remanence can be achieved. This phenomenon is clearly demonstrated in Figure 1.8 for RFE, which shows the response characteristics typically associated with RFEs, including doped-BaTiO<sub>3</sub> and Pb(Mg<sub>1/3</sub>Nb<sub>2/3</sub>)O<sub>3</sub> [54].

The behaviour of materials in response to electric fields and their implications for energy storage states that the RFE nature, which is commonly accepted, originates from the response of PNRs up on altering E. RFEs maintain their unsaturated response even at high applied electric fields, meaning that any increase in the electric field contributes to the storage of energy. To achieve high energy storage, it is favourable to use materials that do not possess high P<sub>r</sub>, which refers to the residual polarization that remains in a material after the removal of E. LD materials meets this requirement, but their energy storage capacity is limited due to their low  $\varepsilon_r$ , which is a measure of the ability of a material to store electrical energy. On the other hand, AFEs display low P<sub>r</sub> when subjected to low E. Moreover, under large electric fields, the P-E loop of AFEs opens due to the stabilization of a FE phase in relation to the AFE phase. This leads to saturated polarization, as illustrated in Figure 1.8. The statement suggests that AFEs, as proposed by Jaffe, could offer advantages for high-energy storage. If issues related to dielectric breakdown are eliminated. Dielectric breakdown refers to the failure of a material as a result of excessive electric fields. In this case, the breakdown strength (BDS) should be high enough to induce the phase transition from the AFE to the FE phase. From the above information, it becomes evident that nonlinear dielectric materials such as FEs, RFEs, and AFEs exhibit energy dissipation, referred to as W<sub>loss</sub>. Hence, the amount of energy that can be recovered, known as W<sub>rec</sub>, becomes the most important parameter. This is schematically illustrated in Figure 1.8 (shaded in blue colour), where the red area represents the energy recovery. Therefore, the value of W<sub>rec</sub> assumes utmost significance in the context of energy storage.

$$W_{rec} = \int_{P_r}^{P_{max}} E \ dP$$

The electrostatic capacitor efficiency can be estimated from the following expression

$$\eta = \frac{W_{rec}}{W_{loss} + W_{rec}}$$

• W<sub>loss</sub> represents the energy loss during discharging

The loss factor is represented in Figure 1.8 (shaded in blue color).

## **REFERENCES**

- [1] Key world energy statistics: International Energy Agency; 2018.
- [2] Panwar NL, Kaushik SC, Kothari S. Role of renewable energy sources in environmental protection: A review. Renew Sust Energ Rev. 2011;15:1513-24.
- [3] Guney MS, Tepe Y. Classification and assessment of energy storage systems. Renew Sust Energ Rev. 2017;75:1187-97.
- [4] Ibrahim H, Ilinca A, Perron J. Energy storage systems—Characteristics and comparisons. Renew Sust Energ Rev. 2008;12:1221-50.
- [5] Liu C, Li F, Ma LP, Cheng HM. Advanced materials for energy storage. Adv Mater. 2010;22:E28-62.
- [6] Kousksou T, Bruel P, Jamil A, El Rhafiki T, Zeraouli Y. Energy storage: Applications and challenges. Sol Energy Mater Sol Cells. 2014;120:59-80.
- [7] Gross R, Leach M, Bauen A. Progress in renewable energy. Environ Int. 2003;29:105-22.
- [8] Dincer I. Renewable energy and sustainable development: A crucial review. Renew Sust Energ Rev. 2000;4:157-75.
- [9] Hall PJ, Bain EJ. Energy-storage technologies and electricity generation. Energ Policy. 2008;36:4352-5.
- [10] Chen H, Cong TN, Yang W, Tan C, Li Y, Ding Y. Progress in electrical energy storage system: A critical review. Progress in Natural Science. 2009;19:291-312.
- [11] Kusko A, Dedad J. Stored energy Short-term and long-term energy storage methods. IEEE Ind Appl Mag. 2007;13:66-72.
- [12] Yao K, Chen S, Rahimabady M, Mirshekarloo MS, Yu S, Tay FE, et al. Nonlinear dielectric thin films for high-power electric storage with energy density comparable with electrochemical supercapacitors. IEEE Trans Ultrason Ferroelectr Freq Control. 2011;58:1968-74.
- [13] Yang, L., Kong, X., Li, F., Hao, H., Cheng, Z., Liu, H., Li, J-F., Zhang, S., Perovskite Lead-free dielectrics for energy storage applications, Progress in Materials Science (2018), doi: https://doi.org/10.1016/j.pmatsci.2018.12.005
- [14] Christen T, Carlen MW. Theory of Ragone plots. J Power Sources. 2000;91:210-6.
- [15] M. Reaney, D. Iddles, Microwave dielectric ceramics for resonators and filters in mobile phone networks. J. Am. Ceram. Soc. 89, 2063–2072 (2006). https://doi.org/10.1111/j. 1551-2916.2006.01025.x

- [16] M.T. Sebastian, Dielectric Materials for Wireless Communication, 1st edn. (Elsevier, Amsterdam, 2008)
- [17] S. Manivannan, A. Joseph, P.K. Sharma, K.C. James Raju, D. Das, Effect of microwave and conventional sintering on densification, microstructure and dielectric properties of BZT–xCr2O3 ceramics. Ceram. Int. 41, 10923–10933 (2015). https://doi.org/10.1016/j.ceramint.2015.05.035
- [18] S. Manivannan, V.S. Surya Chandra, P.K. Sharma, K.C. James Raju, D. Das, Effect of flux addition on mechanical and microwave dielectric properties of barium zinc tantalate ceramics. Trans. Ind. Ceram. Soc. 73, 87–89 (2014). https://doi.org/10.1080/0371750X.2014.922419
- [19] K.A. O'Connor, R.D. Curry, High dielectric constant composites for high power antennas. IEEE Pulsed Power Conf. (2011). https://doi.org/10.1109/ppc.2011.6191417
- [20] T.A.T. Sulong, R.A.M. Osman, M.S. Idris, Trends of microwave dielectric materials for antenna application. AIP Conf. Proc. (2016). https://doi.org/10.1063/1.4958779
- [21] D. Dimos, C.H. Mueller, Perovskite thin films for high frequency capacitor applications. Annu. Rev. Mater. Sci. 28, 397–419 (1998). https://doi.org/10.1146/annurev.matsci.28.1. 397
- [22] I.V. Kotelnikov, V.N. Osadchy, R.A. Platonov, A.G. Altynnikov, V.V. Medvedeva, A.K. Mikhailov, A.G. Gagarin, A.V. Tumarkin, A.B. Kozyrev, Separation of the metallic and dielectric losses of tunable ferroelectric capacitors under control dc voltage. Prog. Electromagn. Res. Lett. 73, 127–131 (2018). https://doi.org/10.2528/pierl17111704
- [23] D. Dimos, S.G. Lockwood, T.J. Garino, H.N. Al-Shareef, R.W. Schwartz, Integrated decoupling capacitors using Pb(Zr, Ti)O3 thin films. Mater. Res. Symp. Proc. 433, 305–316 (1996). https://doi.org/10.1557/proc-433-305
- [24] A. Noma, D. Ueda, Reliability study on bst capacitors for gaas mmic. Integr. Ferroelectr. 15, 69–78 (1997). https://doi. org/10.1080/10584589708015697
- [25] M. Raney, D. Iddles, Microwave dielectric ceramics for resonators and filters in mobile phone networks. J. Am. Ceram. Soc. 89, 2063–2072 (2006). https://doi.org/10.1111/j.1551-2916,2006.01025.x
- [26] Whittingham MS. Materials Challenges Facing Electrical Energy Storage. MRS Bull. 2011;33:411-9.
- [27] V.M. Goldschmidt. Geochemische verteilungsgesetze der elemente. Skrifter utg. Av det Norske Viedenskaps-akademi i Oslo, 2, (1926) 1-117.

- [28] A. M. Glazer. Simple ways of determining perovskite structures. Acta Cryst. B 31, (1975) 756-762.
- [29] A. M. Glazer. The classification of tilted octahedra in perovskites. Acta Cryst. B 28, (1972) 3384-3392.
- [30] H. D. Megaw and C. N. W. Darlington. Geometrical and structural relations in the rhombohedral perovskites. Acta Cryst. B 31, (1975) 161-173.
- [31] J. Valasek. Piezo-Electric and Allied Phenomena in Rochelle Salt. Phys. Rev. 17, (1921) 475.
- [32] G.W. Waston, S.C. Parker and G. Kresse. Ab initio calculation of the origin of the distortion of α-PbO. Phys. Rev. B 59, (1999) 8481.
- [33] R. Seshadri and N.A. Hill. Visualizing the role of Bi 6s "Lone Pairs" in the Off-Center distortion in ferromagnetic BiMnO3.Chem. Mater. 13, (2001) 2892
- [34] X. Tan, J. Frederick, C. Ma, W. Jo, and J. Rödel. Can an Electric Field Induce an Antiferroelectric Phase Out of a Ferroelectric Phase? Phys. Rev. Lett. 105, (2010) 255702.
- [35] H. Schmid. Multiferroic Magnetoelectrics, Ferroelectrics 162, (1994) 317-338.
- [36] D.I. Khomskii. Multiferroics: Different ways to combine magnetism and ferroelectricity. Journal of Magnetism and Magnetic Materials 306, (2006) 1-8.
- [37] Rajasree Das and Kalyan Mandal. Effect of Barium substitution on ferroelectric and magnetic Properties of Bismuth Ferrite. IEEE Transactions on magnetics, 47, NO. 10 (2011) 4054-4057.
- [38] Qingyu Xu, Shengqiang Zhou, D. Wu, Marc Uhlarz, Y. K. Tang, Kay Potzger, M. X. Xu, and Heidemarie Schmidt. Cluster spin glass behavior in Bi(Fe0.95Co0.05)O3. J. Appl. Phys. 107, (2010) 093920.
- [39] C. Michel, J.-M. Moreau, G. D. Achenbach, R. Gerson, and W. J. James. The atomic structure of BiFeO3. Solid State Commun. 7, (1969) 701.
- [40] S. Chattopadhyay, S. D. Kelly, V. R. Palkar, L. Fan and C. U. Segre. Investigation of size effects in magnetoelectric BiFeO3. Phys. Scr. T115, (2005) 709-713.
- [41] Chu, Y.H.; Martin, L.W.; Holcomb, M.B.; Ramesh, R. Controlling magnetism with multiferroics. Mater. Today 2007, 10, 16–23.
- [42] J. R. Teague, R. Gerson, and W. J. James. Dielectric hysteresis in single crystal BiFeO3. Solid State Commun., 8, (1970) 1073.
- [43] J. B. Neaton, C. Ederer, U. V. Waghmare, N. A. Spaldin and K. M. Rabe. First-principles study of spontaneous polarization in multiferroic BiFeO3. Phys. Rev. B 71, (2005) 014113.

- [44] P. Ravindran, R. Vidya, A. Kjekshus, H. Fjellvåg and O. Eriksson. Theoretical investigation of magnetoelectric behavior in BiFeO3. Phys. Rev. B 74, (2006) 224412.
- [45] G.L. Yuan, S.W. Or, H.L. Chan, and Z.G. Liu. Reduced ferroelectric coercivity in multiferroic Bi0.825Nd0.175FeO3 thin film. J. Appl. Phys. 101, (2007) 024106.
- [46] Z.X. Cheng, X.L. Wang, H. Kimura, K. Ozawa, and S.X. Dou. La and Nb codoped BiFeO3 multiferroic thin films on LaNiO3/Si and IrO2/Si substrates. Appl. Phys. Lett. 92, (2008) 092902.
- [47] G.D. Hu, S.H. Fan, C.H. Yang, and W.B. Wu. Low leakage current and enhanced ferroelectric properties of Ti and Zn codoped BiFeO3 thin film. Appl. Phys. Lett. 92, (2008)192905.
- [48] F. Gao, C. Cai, Y. Wang, S. Dong, X.Y. Qiu, G.L. Yuan, Z.G. Liu, and J.-M. Liu. Preparation of La-doped BiFeO3 thin films with Fe2+ ions on Si substrates. J. Appl. Phys. 99, (2006) 094105.
- [49] G. Kartopu, A. Lahmar, S. Habouti, C-L. Solterbeck, B. Elouadi, and M. Es-Souni. Observation of structural transitions and Jahn–Teller distortion in LaMnO3 -doped BiFeO3 thin films. Appl. Phys. Lett. 92, (2008) 151910.
- [50] W.-M. Zhu, H.-H. Guo, and Z.-G. Ye. Structural and magnetic characterization of multiferroic (BiFeO3)1–x(PbTiO3)x solid solutions. Phys. Rev. B 78, (2008) 014401.
- [51] Jaffe, B. Antiferroelectric Ceramics with Field-Enforced Transitions: A New Nonlinear Circuit Element. Proc. IRE 1961, 49, 1264–1267
- [52] Bipul Deka, et. al., BiFeO3-Based Relaxor Ferroelectrics for Energy Storage: Progress and Prospects, Materials 2021, 14(23), 7188; https://doi.org/10.3390/ma14237188
- [53] Damjanovic, D. Ferroelectric, Dielectric and Piezoelectric Properties of Ferroelectric Thin Films and Ceramics. Rep. Prog. Phys. 1998, 61, 1267–1324.
- [54] Bokov, A. A.; Ye, Z. G. Recent Progress in Relaxor Ferroelectrics with Perovskite Structure. J. Mater. Sci. 2006, 41, 31–52

## **CHAPTER - 2**

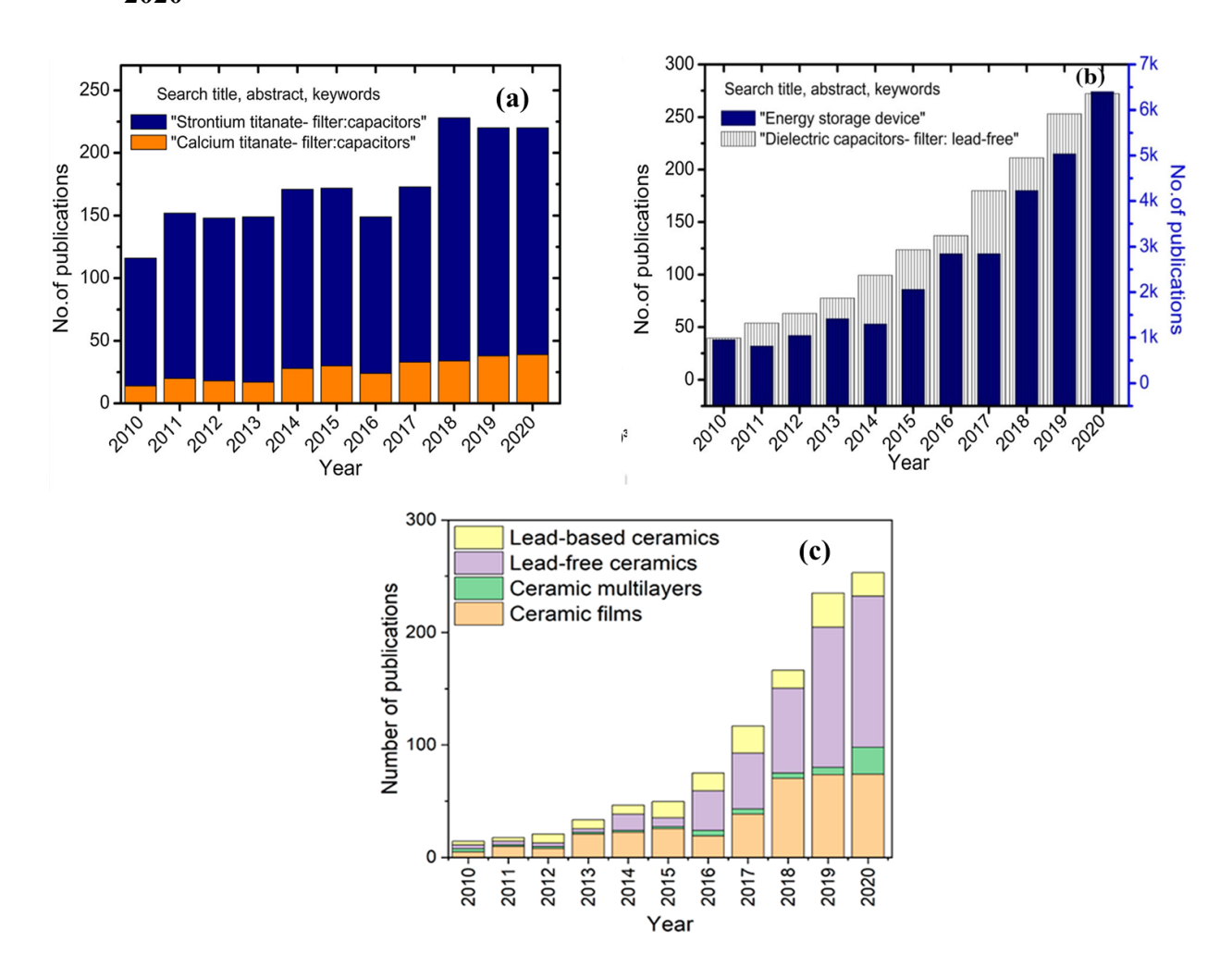
## LITERATURE REVIEW

Considering the importance of dielectric capacitors, significant advancements can be made to enhance the energy density of dielectrics to match or exceed that of batteries, the potential extent of applications for dielectric capacitors (DCs) in energy storage will experience substantial expansion [1]. Moreover, in the current market, commercial capacitors are designed primarily by polymer and ferroelectric dielectrics for high-power density applications. However, these polymer-based energy systems deliver a low energy density of < 2 J/cm 3 [2, 3]. Normally, ferroelectric ceramics possess a high  $\varepsilon$  but a low BDS, whereas polymers possess low  $\varepsilon$  with high BDS. Due to the low  $\varepsilon$  of polymers, these are typically manufactured with a thickness of  $< 1 \mu m$ . Hence multilayer films are manufactured in order to attain high capacitance for commercial applications. Furthermore, polymer-based films cannot sustain higher fields, wherein high filed conduction becomes a limitation to attaining high  $W_{rec.}$  [4]. Furthermore, despite the widespread utilization of polymer-based capacitors, they are unable to sustain at high-temperature conditions. Due to this limitation, polymer-based capacitors cannot be used in oil industries and aviation industries as high-temperature sustaining energy storage devices are required which can operate at a temperature exceeding 150 °C [5, 6].

#### 2.1 Lead-free ferroelectric dielectric ceramics

Ferroelectric dielectric ceramics used for energy storage are divided based on the synthesis and processing, and the thickness (t) of the samples as thin films (t < 1  $\mu$ m), multilayer ceramic capacitors (MLCCs) (t ~ 1 – 10  $\mu$ m), and bulk samples. Thin and MLCCs can afford higher E, exceeding 1MV/cm, owing to their fewer impurities, reduced volume, and defects [7]. As a result, they exhibit higher  $W_{rec}$  [8-13]. However, because of the reduced volume and lower capacitance, the  $W_{total}$  stored in the film is lower compared to the bulk materials. Extensive research has been conducted on lead-based materials as bulk dielectrics, revealing their good  $W_{rec}$  performance. For instance, Pb-based AFE ceramics have achieved an impressive  $W_{rec}$  of 6.4 J cm<sup>-3</sup> [14]. Nevertheless, the toxicity associated with lead (Pb)-based derivatives has raised significant concerns regarding both the environment and human health. Consequently, substantial research has been carried out to explore Pb-free materials as alternatives (Ba-based and Bi-based dielectrics) to overcome this undesired situation [15-17].

# 2.2 Research interest gained towards electrostatic energy storage capacitors from 2010- 2020



Several noteworthy studies have recently focused on lead-free alternatives, (Ba<sub>x</sub>Sr<sub>1-x</sub>)TiO<sub>3</sub> (BST) is a very interesting material system because of its superior loss characteristics at high frequencies, especially in the radio frequency (RF) and microwave bands. Very recently, lead-free BiFeO<sub>3</sub> (BFO) - SrTiO<sub>3</sub> (STO) ceramic capacitor has been proven useful for high-frequency and high-temperature operations [18]. BiFeO<sub>3</sub>-SrTiO<sub>3</sub> (BFSTO) ceramic systems also have the potential to offer high energy density suitable for energy storage applications [19, 20]. The superior energy performance of the BFSTO films is attributed to a microscopic ferroelectric (FE) to relaxor ferroelectric (RFE) phase transition which results from the transformation of the micron scale ferroelectric BFO domains into highly dynamic polar nano-regions (PNR) in the BFSTO matrix [19]. The incorporation of STO in the BFO matrix enhances the breakdown strength significantly resulting in extremely high maximum polarization (P<sub>m</sub>) with reduced remnant polarization (P<sub>r</sub>). Similarly, incorporation of CaTiO<sub>3</sub> (CTO), BaZrO<sub>3</sub> (BZO), SrZrO<sub>3</sub> (SZO), or LaGaO<sub>3</sub> (LGO) in the BFO matrix might result from

similar BFO-based RFEs with interesting high temperature and high-frequency dielectric properties with superior energy performance. Few other investigations have reported impressive results i.e.,  $W_{rec} \sim 37 \text{ J cm}^{-3}$ , and 52 J cm<sup>-3</sup> were achieved for 0.88BT-0.12BMT, and BCT-BZT super-lattices respectively [21, 22]. Furthermore, significant advancements have been made for BZT multilayers to achieve higher  $W_{rec}$  and thermal sustainability. Researchers were able to achieve an extraordinary  $W_{rec} \sim 83.9 \text{ J cm}^{-3}$  and  $\eta \sim 78.4\%$  at ambient temperature for BZT15/BZT35 [23]. BaTiO<sub>3</sub> (BTO) based materials such as thin films of Ba<sub>x</sub>Ca<sub>1-x</sub>TiO<sub>3</sub> – BaZr<sub>x</sub>Ti<sub>1-x</sub>O<sub>3</sub> and xBaTiO<sub>3</sub> – (1-x)Bi(MgTi)O<sub>3</sub> have shown potential for energy storage applications with a large storage density of ~52 J cm<sup>-3</sup> and ~ 37 J cm<sup>-3</sup> respectively [24-26]. Although modified BTO exhibits high energy density, its spontaneous polarization (P<sub>s</sub>) is less (~26  $\mu$ C cm<sup>-2</sup>) compared to that of PbTiO<sub>3</sub> (~80 $\mu$ C cm<sup>-2</sup>). The energy storage properties and ferroelectricity severely degrade at higher temperatures because of its lower Curie temperature (T<sub>c</sub> ~ 120°C), limiting its applications in hybrid electric vehicles and aerospace devices [27-31]

### 2.3 Recent investigations on lead-free materials for energy density and efficiency

An intriguing advancement in energy storage has been observed by implementing interlayer coupling in space-charge dominant hetero-structure ferroelectric thin films composed of BiFeO<sub>3</sub>, BaTiO<sub>3</sub>, and SrRuO<sub>3</sub> [32]. This innovative approach has facilitated the larger enhancement of the film's  $W_{rec}$ ,  $\eta$  capabilities. Specifically, the substantial polarization difference, represented as P<sub>s</sub> - P<sub>r</sub>, has led to an impressive 85% increase in the recoverable electric energy density. This boost in energy density has elevated it from an initial value of approximately 28 J cm<sup>-3</sup> to a remarkable 51 J cm<sup>-3</sup>. Furthermore, lead-free perovskite titanate (BT/ST) thin films have shown great potential when combined with an alloying element, BiFeO<sub>3</sub> (BFO). Adding 25% BFO to the BT composition has yielded highly desirable outcomes. The resulting films exhibit superior crystalline perfection, directly impacting their energy storage properties. These alloyed films have demonstrated exceptional energy storage densities exceeding 52 J cm<sup>-3</sup> when subjected to an E of 2050 kV cm<sup>-1</sup> [33]. Additionally, recent research has uncovered a novel composition based on (Bi<sub>0.5</sub>Na<sub>0.5</sub>)TiO<sub>3</sub> (BNT), termed BNT-Xunzi, x = 0-0.5). This composition exhibits a remarkable  $W_{rec}$ ,  $\eta$ . Incorporating the BNZ dopant into the BNT host material has played a critical role in improving its  $W_{rec}$  capabilities. The introduction of the dopant has facilitated the formation of PNRs, which has made the process of domain switching significantly easier. As a result, the n of the BNT-xBNZ films has

been greatly improved. The energy storage density and efficiency of different ceramic materials are listed below; [21-35]

#### 2.4 Efficiency and recoverable energy density of various lead-free materials

Material		Energy storage density/efficiency
• KNN with (ScNb)O <sub>3</sub>	-	2.48 J/cm <sup>3</sup>
• BaTiO <sub>3</sub> -(ZnNb)O <sub>3</sub>	-	93.50%
• BNBLTZ	-	1.21 J/cm <sup>3</sup> at 100KV/cm
• BaTiO <sub>3</sub> -Bi(MgNb)O <sub>3</sub>	-	$1.13 \text{ J/cm}^3$
(BT-BMN)		
• AgNbO <sub>3</sub> (Mn doped)	-	$6.5 - 5.3 \text{ J/cm}^3$
• BNT	-	2.42 J/cm <sup>3</sup>
• BiFeO <sub>3</sub> – BaTiO <sub>3</sub> - Ba(MgNb)O <sub>3</sub>	-	75.00%
• BNKT-KNN	-	$1.20 \text{ J/cm}^3$
• BNT-KN	-	$1.17 \text{ J/cm}^3$
• KNN-BMT	-	$4.08 \text{ J/cm}^3$
• ST-NBT-BT	-	$1.7 \text{ J/cm}^3$
<ul> <li>BFO-based thin films</li> </ul>	-	70 J/cm <sup>3</sup> , 51 J/cm <sup>3</sup>

Thoroughly studied Pb-free FE ceramics, specifically developed for electrostatic-energy storage applications, primarily revolve around BT materials. It is widely recognized within the scientific community that BT and its derivatives exhibit relatively low levels of saturation polarization and ferroelectric transition temperature. These innate limitations pose challenges when considering their utilization in high-temperature environments requiring enhanced recoverable density and  $\eta$ . Consequently, few research studies have focused on exploring compositions centered around BFO, a well-recognized FE material. This emphasis on BFO is primarily due to its remarkable characteristics, including an exceptionally high level of saturation polarization and a high ferroelectric transition temperature. These properties make BFO-based compositions highly desirable for applications demanding robust performance under demanding conditions.

By shifting attention towards BFO, researchers aim to overcome the limitations of BT and its derivatives, ultimately expanding the potential for Pb-free FE ceramics in various high-temperature applications.

## 2.5 Recent investigations on lead-free BFO-based ceramics and key findings

Authors Correia et al. presented a groundbreaking study on a Pb-free ceramic material composed of BF-ST. This material demonstrated outstanding properties, including a  $\eta$  and reduced losses, making it highly suitable for applications in high-temperature environments [36, 37]. Explicitly, the variants 40BF-60ST and 20BF-80ST showed remarkably low dielectric loss and outstanding thermal stability. Even at temperatures up to 200 °C, these materials maintained their high  $W_{rec}$  and facilitated faster discharge times. This commendable achievement indicates the ability of the material to perform effectively under challenging conditions. The researchers also achieved excellent results in BFO-based film capacitors through domain engineering.

S. No.	Title	Source	Compositi on	Findings	
1	Giant energy density and high efficiency achieved in BFO-based film capacitors via domain engineering.	Nature Communication, 10.1038/s41467- 01 8-04189-6	BFO-STO	Energy density ~70  J/cm <sup>3</sup> STO improves  Insulation, breakdown  strength	
2	A lead-free and high energy density ceramics for energy storage applications.	J. Am. Ceram. Soc.,10.1111/Jace 12508	BFO-STO	Efficiency ~85%, operating temp. up to 200 °C	
3	Lead-free ceramics with high energy density and reduced losses for high- temperature applications.	Adv. engineering Mat.,10.1002/ adem.201700019	BFO-STO	High operating temp. than X8R capacitor	
4	Low-temperature dielectric behaviour of BiFeO3-modified CaTiO3 incipient ferroelectric ceramics.	J. of Applied Physics,10.1063/ 1.4729080	ВБО-СТО	Dielectric behavior is The same as BFO-STO	
5	Remarkable energy- storage performances and excellent stability in CaTiO <sub>3</sub> – doped BiFeO <sub>3</sub> – BaTiO <sub>3</sub> relaxor ferroelectric ceramics	J. of Eur. Car. Soc 10.1016/j.jeurcer amsoc.2022.11.0 01	BiFeO <sub>3</sub> - BaTiO <sub>3</sub> - CaTiO <sub>3</sub>	$W_{rec} \sim 5.03 \text{ J/cm3}, \\ \eta \sim 89.70\%, BDS \sim 380 \\ \text{kV/cm and temperature} \\ \sim 150  ^{\circ}\text{C}$	

S. No.	Title	Source	Composition	Findings
6	Improved structural stability and multiferroic characteristics in CaTiO <sub>3</sub> – Modified BiFeO <sub>3</sub> ceramics	J. Am. Ceram. Soc.,10.1111/j. 1551 -916.20 11.04824x	CaTiO <sub>3</sub> modified BiFeO <sub>3</sub>	Leakage current density reduced, Improved structural stability, enhanced resistivity
7	Outstanding comprehensive energy storage performance in lead-free BiFeO <sub>3</sub> -based RFE ceramics by multiple optimization design	Acta Materialia 10.1016/j.actm at.2022.118286	Bi <sub>0.9</sub> La <sub>0.1</sub> FeO <sub>3</sub> - Ba <sub>0.7</sub> Sr <sub>0.3</sub> TiO <sub>3</sub> - NaNb <sub>0.85</sub> Ta <sub>0.15</sub> O <sub>3</sub>	$W_{rec} \sim 15.90 \ J/cm3,$ $\eta \sim 87.70\%$
8	Optimized electric- energy storage in BiFeO <sub>3</sub> -BaTiO <sub>3</sub> ceramics via tailoring microstructure and nanocluster	J. of Eur. Car. Soc,10.1016/C ar.2022.12.064	BiFeO3-BaTiO3	$\begin{aligned} W_{rec} \sim 4.10 \ J/cm3, \\ \eta \sim 62.10\%, \\ E_{max} = 220 \ kV/cm \end{aligned}$
9	BiFeO3-SrTiO3 thin film as a new lead-free RFE capacitor with ultrahigh energy storage performance	J. of Mat. Chem. A2017, 5, 5920-5926	BiFeO3- SrTiO3	$\Gamma$ = 1.61, low leakage current, BDS ~ 3.6 MV cm <sup>-1</sup>
10	A lead-free and high- energy density ceramic for energy storage applications	J. Am. Ceram. Soc.,10.11 11/jace.12508	BFO-STO	$W_{rec} \sim 18.6 \ J/cm3,$ $\eta \sim 85\%,$ $E_{max} = 972 \ kV/cm$

By implementing this technique, they reached a giant  $W_{rec} \sim 70 \text{ J cm}^{-3}$ , which is a significant achievement. In addition to that, the capacitors exhibited a high  $\eta \sim 85\%$ . These findings highlight the immense potential of BFO-based film capacitors for energy storage applications. One exciting aspect of the study is the incorporation of STO into the BFO structure. This addition resulted in the transformation of the FE micro-domains of BFO into highly-dynamic PNRs. This transition from FE to RFE nature significantly improved the material's  $W_{rec}$  and  $\eta$ . Moreover, the introduction of STO positively impacted the film's electrical insulation and BDS by inhibiting the Fe transition. Overall, the research conducted by Correia et al. highlights the remarkable advancements in Pb-free ceramic materials, specifically the BFO-STO matrix.

Careful examination of the existing literature shows that dielectrics possessing a high  $P_m$ , low  $P_r$ , and maximum achievable BDS are important in achieving superior  $\eta$  performances. Using first principle calculations, recent simulation studies have identified even higher energy densities ranging from 100 to 150 J cm<sup>-3</sup>. This estimation highlights the substantial potential of materials based on BFO as high-energy density dielectric capacitors [38]. Moreover, the investigation of lead-free compositions based on BFO for energy storage applications still needs to be enhanced. Consequently, the present proposal aims to investigate novel lead-free FE materials based on BFO for energy storage applications, specifically focusing on temperatures up to 300 °C. The proposed research will study these prospective materials in bulk and thin films and computational analyses of the electrical properties relevant to energy storage applications.

#### REFERENCES

- [1] Li Q, Han K, Gadinski MR, Zhang G, Wang Q. High energy and power density capacitors from solution-processed ternary ferroelectric polymer nanocomposites. Adv Mater. 2014;26:6244-9.
- [2] Hao X. A review on the dielectric materials for high energy-storage application. J Adv Dielectr. 2013;3:1330001.
- [3] Yao Z, Song Z, Hao H, Yu Z, Cao M, Zhang S, et al. Homogeneous/Inhomogeneous-Structured Dielectrics and their Energy-Storage Performances. Adv Mater. 2017;29:1601727.
- [4] Chen Q, Wang Y, Zhou X, Zhang QM, Zhang S. High field tunneling as a limiting factor of maximum energy density in dielectric energy storage capacitors. Appl Phys Lett. 2008;92:142909.
- [5] Johnson RW, Evans JL, Jacobsen P, Thompson JR, Christopher M. The Changing Automotive Environment: High-Temperature electronics. IEEE Transactions on Electronics Packaging ManIEEE Electrical Insulation Magazineufacturing. 2004;27:164-76.
- [6] Neudeck PG, Okojie RS, Liang-Yu C. High-temperature electronics A role for wide bandgap semiconductors? Proceedings of the IEEE. 2002;90:1065-76.
- [7] McPherson JW. On why dielectric breakdown strength reduces with dielectric thickness. Proceedings of the IEEE International Reliability Physics Symposium (IRPS) 2016, pp. 3A--1-3A--8.
- [8] Correia TM, McMillen M, Rokosz MK, Weaver PM, Gregg JM, Viola G, et al. A Lead-Free and High-Energy Density Ceramic for Energy Storage Applications. J Am Ceram Soc. 2013;96:2699-702.
- [9] Peng B, Zhang Q, Li X, Sun T, Fan H, Ke S, et al. Giant Electric Energy Density in Epitaxial Lead-Free Thin Films with Coexistence of Ferroelectrics and Antiferroelectrics. Advanced Electronic Materials. 2015;1:1500052.
- [10] Wang Y, Hao X, Yang J, Xu J, Zhao D. Fabrication and energy-storage performance of (Pb,La)(Zr,Ti)O3 antiferroelectric thick films derived from polyvinylpyrrolidone-modified chemical solution. J Appl Phys. 2012;112:034105.
- [11] Xie Z, Yue Z, Peng B, Zhang J, Zhao C, Zhang X, et al. Large enhancement of the recoverable energy storage density and piezoelectric response in relaxor-ferroelectric

- capacitors by utilizing the seeding layers engineering. Appl Phys Lett. 2015;106:202901.
- [12] Ma B, Kwon D-K, Narayanan M, Balachandran UB. Dielectric properties and energy storage capability of antiferroelectric Pb0.92La0.08Zr0.95Ti0.05O3 film-on-foil capacitors. J Mater Res. 2009;24:2993-6.
- [13] Chauhan A, Patel S, Vaish R, Bowen C. Anti-Ferroelectric Ceramics for High Energy Density Capacitors. Materials. 2015;8:8009-31.
- [14] Zhang L, Jiang S, Fan B, Zhang G. Enhanced energy storage performance in (Pb0.858Ba0.1La0.02Y0.008)(Zr0.65Sn0.3Ti0.05)O3–
  (Pb0.97La0.02)(Zr0.9Sn0.05Ti0.05)O3 antiferroelectric composite ceramics by Spark Plasma Sintering. J Alloys Compd. 2015;622:162-5.
- [15] Rödel J, Jo W, Seifert KTP, Anton E-M, Granzow T, Damjanovic D. Perspective on the Development of Lead-free Piezoceramics. J Am Ceram Soc. 2009;92:1153-77.
- [16] Saito Y, Takao H, Tani T, Nonoyama T, Takatori K, Homma T, et al. Lead-free piezoceramics. Nature. 2004;432:84-7.
- [17] Shvartsman VV, Lupascu DC. Lead-Free Relaxor Ferroelectrics. J Am Ceram Soc. 2012;95:1-26.
- [18] T. Correia, M. Stewart, A. Ellmore, K. Albertsen, Lead-free ceramics with high energy density and reduced losses for high temperature applications. Adv. Eng. Mater. 19, 1700019 (2017). https://doi.org/10.1002/adem.201700019
- [19] H. Pan, J. Ma, J. Ma, Q. Zhang, X. Liu, B. Guan, L. Gu, X. Zhang, Y.-J. Zhang, L. Li, Y. Shen, Y.-H. Lin, C.-W. Nan, Giant energy density and high efficiency achieved in bismuth ferrite-based film capacitors via domain engineering. Nat. Commun. (2018). https://doi.org/10.1038/s41467-018-04189-6
- [20] T.M. Correia, M. McMillen, M.K. Rokosz, P.M. Weaver, J.M. Gregg, G. Viola, M.G. Cain, A lead-free and high-energy density ceramic for energy storage applications. J. Am. Ceram. Soc. 96, 1–4 (2013). https://doi.org/10.1111/jace. 12508.paper1
- [21] Kwon. D. and Lee M. H., "Temperature-stable high-energy-density capacitors using complex perovskite thin films", IEEE T. Ultrason. Ferr., 59, 1894-99, (2012)
- [22] Sun Z. et al., "Ultrahigh energy storage performance of lead-free oxide multilayer film capacitors via interface engineering", Adv. Mater., 29, 1604427 (2017)

- [23] Q. Fan et al., "Significantly enhanced energy storage density with superior thermal stability by optimizing Ba(Zr0.15Ti0.85)O3/Ba(Zr0.35Ti0.65)O3 multilayer structure", Nano Energy, 51, 539-45, (2018)
- [24] Z. Xie, B. Peng, S. Meng, Y. Zhou, Z. Yue, High-energystorage density capacitors of Bi(Ni1/2Ti1/2)O3-PbTiO3 thin films with good temperature stability. J. Am. Ceram. Soc. 96, 2061–2064 (2013). https://doi.org/10.1111/jace.12443
- [25] Y. Wang, X. Hao, J. Yang, J. Xu, D. Zhao, Fabrication and energy-storage performance of (Pb, La)(Zr, Ti)O3 antiferroelectric thick films derived from polyvinylpyrrolidone-modified chemical solution. J. Appl. Phys. 112, 034105 (2012). h ttps://doi.org/10.1063/1.4742128
- [26] N. Triamnak, R. Yimnirun, J. Pokorny, D.P. Cann, Relaxor characteristics of the phase transformation in (1–x)BaTiO3- xBi(Zn1/2Ti1/2)O3 perovskite ceramics. J. Am. Ceram. Soc. 96, 3176–3182 (2013). https://doi.org/10.1111/jace.12495
- [27] Z. Shen, X. Wang, B. Luo, L. Li, BaTiO3-BiYbO3 perovskite materials for energy storage applications. J. Mater. Chem. A 3, 18146–18153 (2015). https://doi.org/10.1039/C6TA90102F
- [28] C. Ederer, N.A. Spaldin, Effect of epitaxial strain on the spontaneous polarization of thin film ferroelectrics. Phys. Rev. Lett. 95, 257601 (2005). https://doi.org/10.1103/physre vlett.95.257601
- [29] P. Kim, N.M. Doss, J.P. Tillotson, P.J. Hotchkiss, M.-J. Pan, S.R. Marder, J. Li, J.P. Calame, J.W. Perry, High energy density nanocomposites based on surface-modified BaTiO3 and a ferroelectric polymer. ACS Nano 3, 2581–2592 (2009). https://doi.org/10.1103/physrevlett.95.257601
- [30] Y. Zhang, J. Huang, T. Ma, X. Wang, C. Deng, X. Dai, Sintering Temperature dependence of energy-storage properties in (Ba, Sr)TiO3 glass–ceramics. J. Am. Ceram. Soc. 94, 1805–1810 (2011). https://doi.org/10.1111/j.1551-2916.2010. 04301.x
- [31] L. Zhu, B. Zhang, S. Li, L. Zhao, N. Wang, X. Shi, Enhanced piezoelectric properties of Bi (Mg1/2Ti1/2)O3 modified BiFeO3–BaTiO3 ceramics near the morphotropic phase boundary. J. Alloys Compd. 664, 602–608 (2016). https://doi.org/10.1016/j.jallcom.2016.01.003
- [32] H. Zhu et al., "Increasing energy storage capabilities of space-charge dominated ferroelectric thin films using interlayer coupling", Acta Materialia 122, 252-258, (2017)

- [33] S. Cho et al., "Strongly enhanced dielectric and energy storage properties in lead-free perovskite titanate thin films by alloying", Nano Energy, 45, 398–406, (2018)
- [34] N. Sun et al., "Giant energy-storage density and high efficiency achieved in (Bi0.5Na0.5)TiO3- Bi(Ni0.5Zr0.5)O3 thick films with polar nanoregions", J. Mater. Chem. C, 6, 10693-10703, (2018)
- [35] M. Peddigari et al., "Boosting the Recoverable Energy Density of Lead-Free Ferroelectric Ceramic Thick Films through Artificially Induced Quasi-Relaxor Behavior", ACS Appl. Mater. Interfaces, 10, 20720–20727, (2018)
- [36] T. M. Correia et al., "A Lead-Free and High-Energy Density Ceramic for Energy Storage Applications", J. Am. Ceram. Soc., 1–4 (2013)
- [37] T. M. Correia et al., "Lead-Free Ceramics with High Energy Density and Reduced Losses for High Temperature Applications", ADVANCED ENGINEERING MATERIALS 2017, DOI: 10.1002/adem.201700019
- [38] B. Xu et al., "Designing lead-free antiferroelectrics for energy storage", NATURE COMMUNICATIONS | 8:15682 | DOI: 10.1038/ncomms15682

#### **CHAPTER - 3**

#### **OBJECTIVE OF THE WORK**

The energy demand continuously increases day by day as the world population surges and the global economy expands with many environmental challenges. To put this into perspective, the world's total energy consumption substantially increased from 54,207 TWh in 1973 to a staggering 111,125 TWh in 2016. In order to reduce pollution, and global warming to 1.5 °C as proposed by many agencies, national, and international agreements, CO<sub>2</sub> exhausts must be curtailed by ~45% by 2030 and should touch zero by 2050. Regenerative sources, like solar, wind, and geothermal energy, are gradually gaining dominance in the energy landscape, aiming to replace the reliance on fossil fuels. Nevertheless, the transition to renewable energy sources is not without its hurdles. One significant challenge lies in the intermittent nature of most renewable energy sources. Unlike traditional fossil fuels that provide a consistent energy supply, renewables fluctuate in their generation capacity, which poses difficulties in effectively harnessing their full potential. To overcome this hurdle, converting renewable energy, primarily into electricity, a versatile and widely usable form of energy, is imperative. This conversion process necessitates deploying efficient and reliable electrical energy storage solutions. These energy systems are important to ensure that the electricity generated from renewable sources can be effectively captured, stored, and utilized when needed. In order to address the environmental problems associated with currently using conventional energy resources, there is a dire need to move towards green and regenerative energy resources to overcome the environmental issues that the globe is facing now. Moreover, in order to unlock the capability of renewable energy and assure a sustainable and effective energy future, it is most important to develop reliable electrical energy storage systems that can accommodate the intermittent behaviour of most renewable resources.

- ➤ Batteries are good at storing much energy, but they can slowly discharge.
- Flywheels can store a lot of energy and discharge it quickly, but they are expensive.
- > Superconducting magnetic energy storage (SMES), systems are very efficient, but they are also costly.
- Electrochemical capacitors (ECs) offer a good energy and power density balance. They are better than batteries at storing a lot of energy, but they can discharge it much more quickly. ECs are also relatively inexpensive.

Dielectric capacitors and electrostatic capacitors are better suited for high-voltage applications. They are also cost-effective for large-scale projects. Pb-based materials produce high recoverable density but lead is hazardous to human health and the environment. Hence Pb-free materials are strongly recommended.

In the present investigation, lead-free BFO-based materials were chosen and their structural, electrical, dielectric, and ferroelectric properties were explored. The selection of the material is driven by environmental concerns. The studies on BFO-based ferroelectric materials started way back in the 1960s but the improvements in energy storage by enhancing various parameters is a challenging task. RFE nature and PNR creation are still required a thorough investigation.

Considering all the limitations and considerations the research challenges are formulated as;

#### **Research challenges:**

- ✓ Bi is volatile in nature, structurally, and thermodynamically unstable, hence the preparation of high-quality ceramics with enhanced structural integrity and minimal defects.
- ✓ Selection of the secondary compound to substitute without losing the inherent properties of BFO to retain high saturation polarization and recoverable energy density.
- ✓ Obtaining high-densified samples as there is a large difference in sintering temperature conditions between BFO and CTO
- ✓ Enhancing RFE nature (BFO-CTO) by partial substitution of CTO into BFO in order to improve the mobility of the electric dipoles, thereby improving the  $W_{rec.}$

#### Objectives of the current research work

- ✓ Fabrication of good quality ceramics (BFO-CTO)
- ✓ Enhancing RFE nature by introducing CTO into BFO
- ✓ Increasing  $P_s$ , and reduce  $P_r$
- ✓ Slim P-E hysteresis loops with tremendously enhanced  $W_{rec}$ , and efficiency by reducing leakage current densities
- ✓ Minimization of environmental impact by manufacturing high-power density capacitors to store and utilize for commercial applications.

#### **CHAPTER - 4**

#### EXPERIMENTAL PROCEDURE

The good quality and properties of the material are mainly associated with the specific processing methods that are employed. Hence, it becomes important to systematically monitor every step of the synthesis and processing technique and related conditions to obtain outstanding outcomes. This entails a careful and focused approach toward the preparation of ferroelectric ceramics. Considering this priority, the ceramic samples are carefully handled to ensure the best quality sample outcomes. For every parameter, i.e., temperature, pressure, and time optimization, extensive efforts have been taken and carefully monitored the conditions throughout the process. This chapter also discusses the specific techniques used to synthesize and fabricate individual compounds, including mixed compositions. The methodology employed in preparing these ceramics is studied in detail. The provided knowledge in this chapter may guide the researchers and students who prepare the same material with the methodology followed in this present research work.

### 4.1 Synthesis of BiFeO<sub>3</sub> powder using solution combustion route

#### Raw materials:

- BFO powder was prepared using bismuth nitrate pentahydrate (Bi(NO<sub>3</sub>)<sub>3.5</sub>H<sub>2</sub>O) and iron nitrate nonahydrate (Fe(NO<sub>3</sub>)<sub>3.9</sub>H<sub>2</sub>O) of purity ≥ 99.9% procured from Sigma Aldrich, USA.
- Glycine (C<sub>2</sub>H<sub>5</sub>NO<sub>2</sub>)

The raw materials were weighed in a stoichiometric ratio and dissolved in a minimum quantity of deionized water. Glycine ( $C_2H_5NO_2$ ) of purity  $\geq 99.9\%$  was added to the resulting nitrate solution with a Glycine to nitrate ratio of 1:2. Nitric acid (HNO<sub>3</sub>) was added to the solution for complete dissolution till the transparent solution was obtained. The solution was stirred and heated simultaneously at 85°C until a viscous solution was obtained.

The hot plate temperature was increased to 420°C until complete combustion took place with copious evolution of gases and fly ashes. The obtained powder was calcined at 650 °C for 2 h for the complete phase formation.



Fig. 4.1 BiFeO<sub>3</sub> viscous solution before combustion

## 4.2 Synthesis of CaTiO<sub>3</sub> powder using solution combustion route



Fig. 4.2 CaTiO<sub>3</sub> viscous solution before combustion

#### Raw materials:

- Tetrabutyl titanate ([CH<sub>3</sub>(CH<sub>2</sub>)<sub>3</sub>O]<sub>4</sub>Ti) (TBT)
- Calcium nitrate tetrahydrate Ca(NO<sub>3</sub>)<sub>2.</sub>4H<sub>2</sub>O of purity ≥ 99.9% procured from Sigma Aldrich. The raw materials were dissolved in a minimum quantity of deionized water.

A white color solution was obtained upon adding TBT to the aqueous nitrate solution. Glycine was added to the resulting precursor solution with a Glycine to nitrate ratio of 1:2. On adding HNO<sub>3</sub>, a transparent solution was obtained, which on continuous stirring and heating at 85°C, turned into a highly viscous solution.

The hot plate temperature was increased to 420°C until the complete combustion of the viscous solution took place. The obtained powder was calcined at 1250 °C for 4 h.

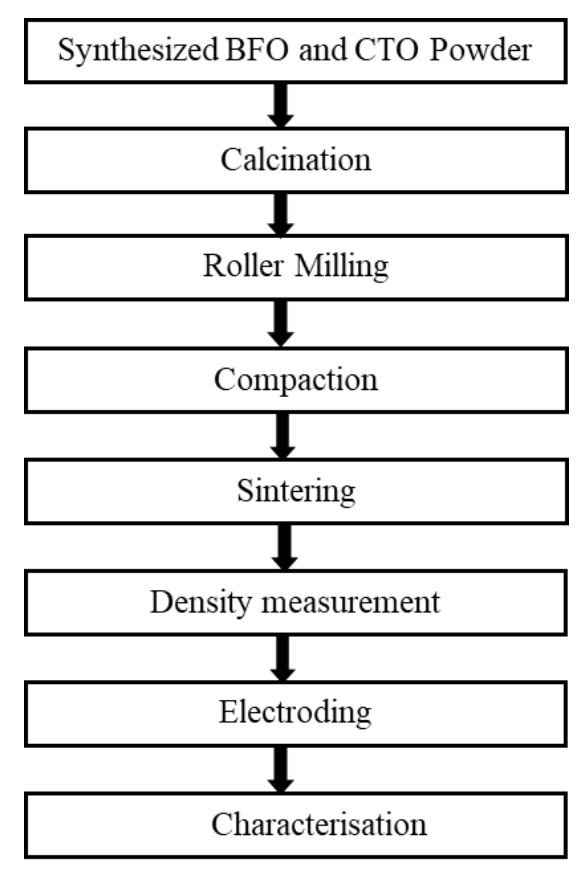


Fig. 4.3 Schematic layout of BFO-CTO synthesis, processing, and characterization

#### 4.3 Calcination

It is the thermal treatment process in which the solid material is subjected to heat treatment (high temperature of a few hundred °C to thousand °C) in the presence or absence of air (O<sub>2</sub>) according to the material interactions and chemical changes. Calcination involves dehydration, decomposition, and chemical and physical changes. As a result, the physical and chemical transformation takes place to form either partial or fully phase pure material. During the calcination process, ions interaction causes a diffusion to attain a homogeneous solid matrix. Calcination parameters are prominent factors that affect the shrinkage volume during the sintering process. The primary prerequisite is that the obtained calcined powder must be homogeneous and as consistent as possible. In the present study, the calcination process was

carried out in closed alumina crucibles using a resistance-heating furnace. Powders were calcined at various temperatures to determine the appropriate calcination temperature. Figure 4.4 shows the calcination profile of synthesized BFO and CTO powders at an optimized temperature condition.

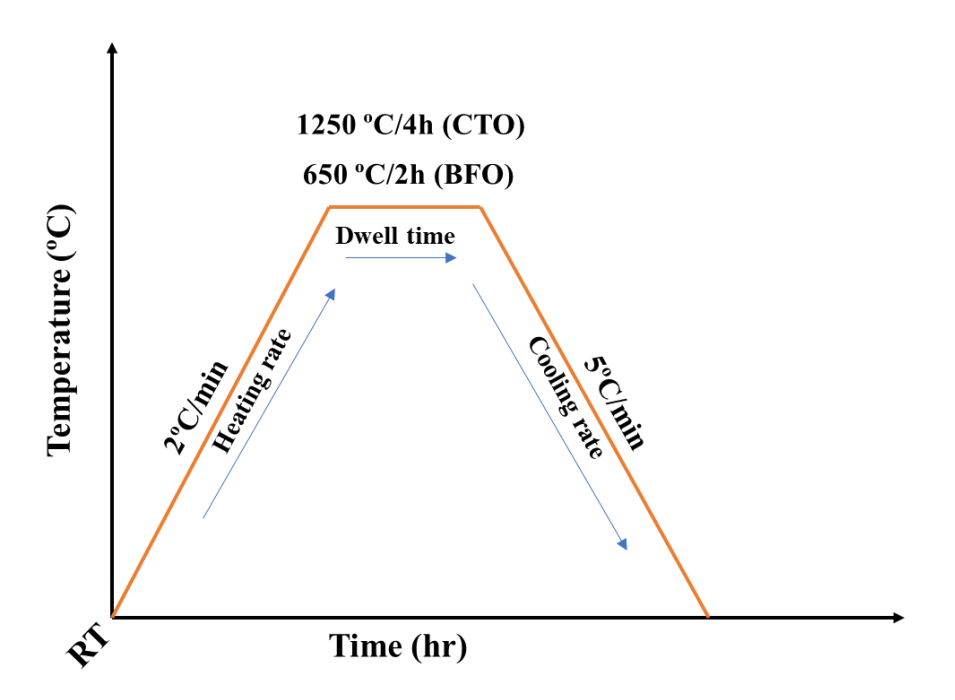


Fig. 4.4 Calcination profile of as-synthesized BFO and CTO powders at an optimized temperature condition

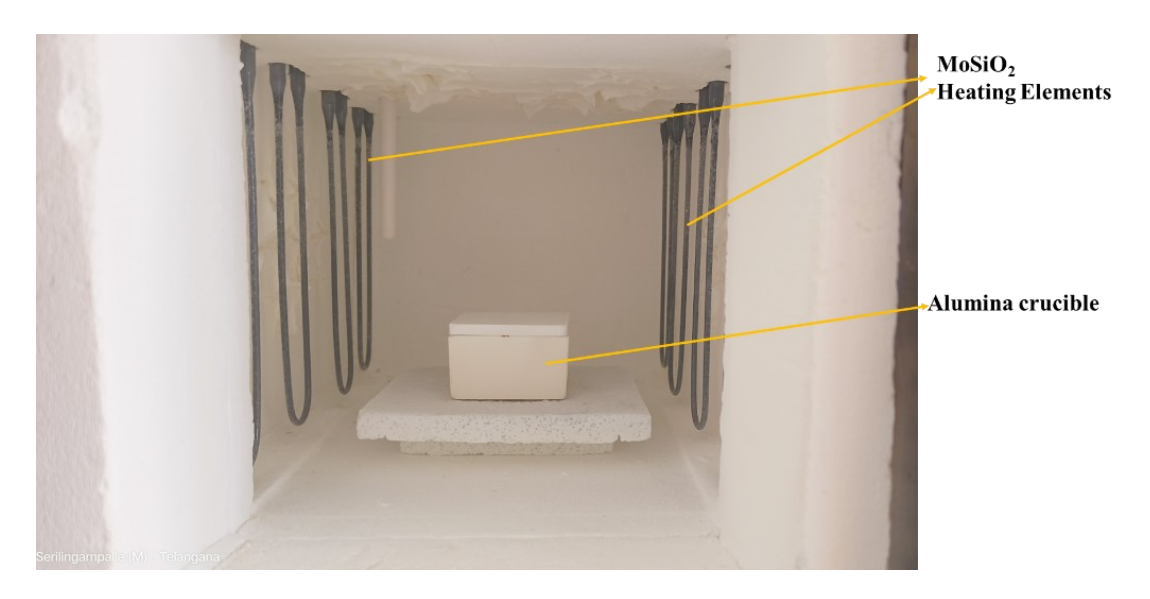


Fig. 4.5 Resistance heating furnace used for calcination representing heating elements and alumina crucible.

#### 4.4 Granulation

The calcined powders formed lumps which resulted in increased particle size. Therefore, the calcined powders were subjected to size reduction, i.e., via manual wet-grinding (using mortar and pestle) and roller milling followed by sieving with a mesh 3 to 4 times to get fine and homogenous size powders. Granulation is an important procedure done to the ball-milled powders. This process is essential to form granules (creating more excellent units of the powder) from fine powder particles. This is done by mixing the powders with appropriate polymer binders in small quantities. Granulated powders have good pressing properties and better flow when compared to finer particles. This procedure of granulation adds strength to the green compacts.

#### 4.5 Pelletization

Pelletization is making powders into a compact pellet shape by applying pressure. This is done by loading the powder in a die of the required shape and size and pressing the die using appropriate pressure. The required amount of powder obtained has been taken to fabricate the green samples with a diameter of 10 mm and thickness (t) of 1 mm using a uniaxial press. A high chromium high carbon hardened steel circular die has been used to press the granules into pellets. The lower punch of the die was kept inside the die before pouring the granules into the die cavity. The granules were then taken into the die cavity, and gentle vibration was applied to the die to ensure uniform distribution of the granules inside the die cavity. After that, the upper punch was placed inside, and a little pressure was applied to avoid the powder splashing out of the die during the load applied by the press. The pressure required to make the compact is an essential factor as it affects the green strength of the compact. Hence the pressure applied was varied to derive the optimum pressure.

Green density increases with increasing load, which is observed in Figure 4.7 with the increase in applied pressure, the green density of the pellets also increased, but for the applied pressure above 562 and 624 MPa, cracks were observed on the surface of the compacted samples. For the load of 312 MPa, the green density is very low and moderate for the pressure between 375 - 437 MPa.

Density, 
$$\rho_{\text{max}} = \frac{\sum_{i=1}^{n} c_i W_i}{\sum_{i=1}^{n} \frac{c_i W_i}{\rho_i}}$$

- n represents the total number of elements
- C represents the molar composition
- W represents the atomic weight

•  $\rho_i$  is the density of the i<sup>th</sup> element.

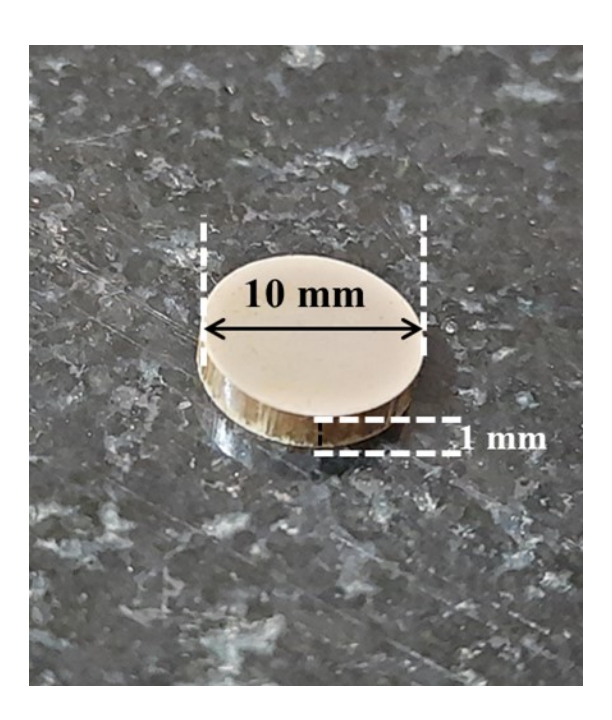


Fig. 4.6 Green pellet with dimensions; diameter ~10 mm, thickness ~1 mm

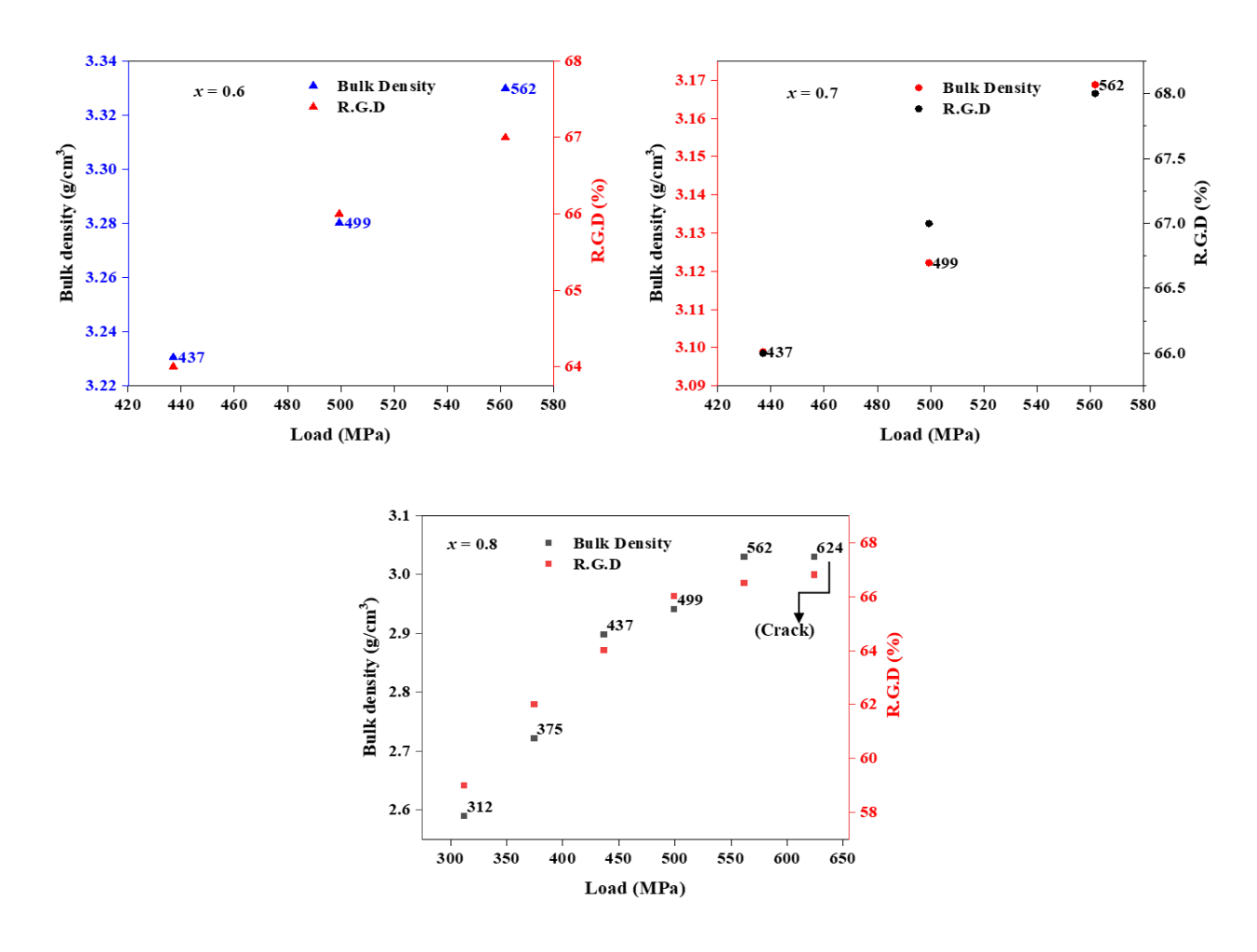


Fig. 4.7 Relative green density and bulk density as a function of applied load

The theoretical density,  $\rho_{mix}$  is estimated using the rule of mixtures formula expressed as; The relative green density percentage is calculated using the following formula;

Relative green density (%) = (Experimentally measured density/theoretical density) \*100



Fig. 4.8 Manual grinding using mortar and pestle



Fig. 4.9 Green pellet making using uniaxial compaction setup and die

BFO and CTO calcined powders were weighed and mixed to prepare the composite powders of  $(BFO)_{(1-x)} - (CTO)_x$  (x = 0.6, 0.7, and 0.8). The powders were mixed in a roller mill for 14

h with isopropyl alcohol (IPA) as the solvent and ZrO<sub>2</sub> balls as the grinding media with a powder to ZrO<sub>2</sub> ball ratio of 1:5. The milled powder was dried, and manually grinded using mortar and pestle to obtain homogeneous grain size and utilised for pelletisation with a dimension of 10 mm in diameter and 1 mm in thickness. The green pellets were dried at 120°C for 8 hrs. The dried samples were subjected to microwave sintering.

Using pellet die powder systems were pressed uniaxially with PVA (8-10 wt.%) as the binder. The uniaxial compaction pressure was optimized concerning sintered density.

## 4.6 Binder burnout and sintering

## 4.6.1 Microwave sintering technique

Binder burnout was done for the green pellets in a microwave sintering furnace. The binder burnout profile is shown in Figure 4.10 along with the sintered profile layout. A very slow heating rate was followed for the binder removal, which will reduce the development of cracks if heated faster. Sintering is a thermal treatment process in which compacted samples are yielded into highly dense polycrystalline aggregates. Green pellets were sintered using different sintering profiles in an electrical resistance heating furnace and microwave sintering furnace. The results obtained through RHF and MWS techniques are discussed in detail in the results and discussion section. Sintering is the control of both densification and grain growth. Densification is the act of reducing porosity in a sample, thereby making it denser [1, 2]. Grain growth is the process of grain boundary motion to increase the average grain size. Many properties (mechanical strength, electrical breakdown strength, etc.) benefit from a high relative density and a small grain size. Sintering occurs by diffusion of atoms through the microstructure. A gradient of chemical potential causes this diffusion, atoms move from an area of higher chemical potential to an area of lower chemical potential. The system's reduction in surface free energy is the driving force for sintering. The decline in energy occurs via densification and grain growth; hence, the material gets densified.

A microwave sintering furnace from Linn High Therm GMBH, (model MKH-4, 8-150/150/150) with maximum working temperature  $\sim$  1850 °C, output power  $\sim$ 4.8 kW and frequency  $\sim$ 2.45 GHz  $\pm$  50MHz was used.

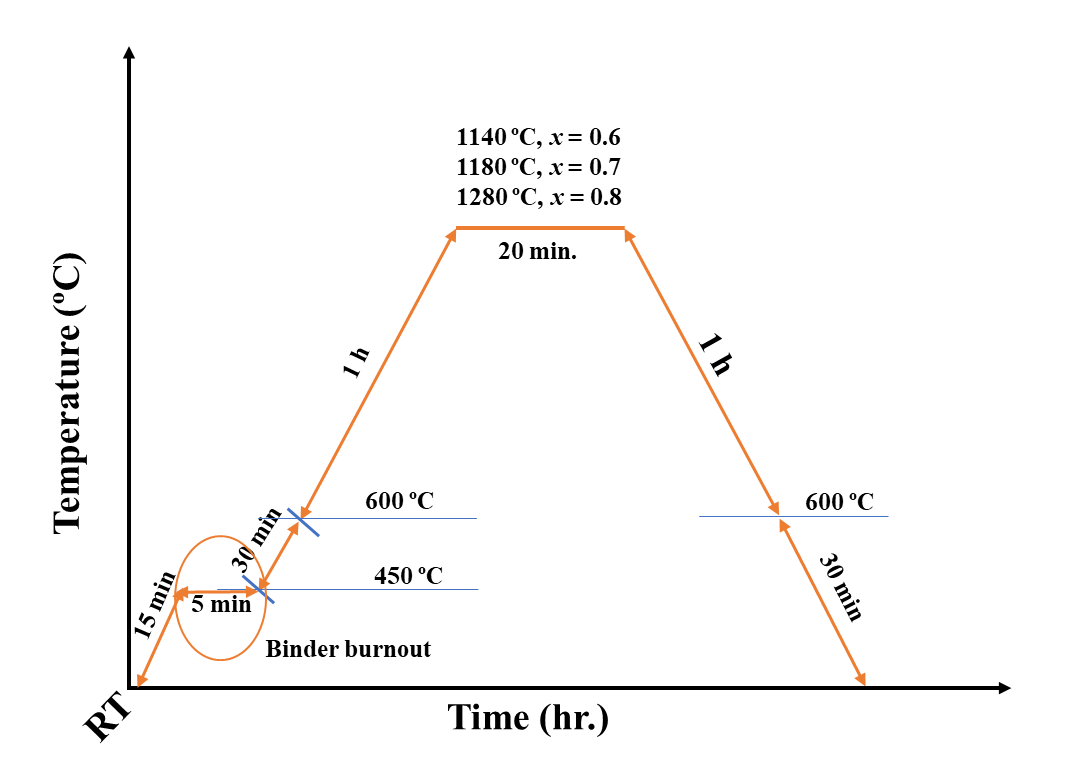


Fig. 4.10 Binder burnout and microwave sintering profile for optimized sintering temperature conditions of (1-x)BFO- xCTO



Fig. 4.11 Microwave sintering furnace setup and sample loading in SiC susceptor

Microwave sintering has been carried out at 1000-1280°C for 20 mins and optimized for sintered density. The optimized conditions (resulting in  $\geq$  95% of the theoretical density) for microwave sintered (MWS) samples were 1140°C, 1180°C and 1280°C/20 mins for x = 0.6, 0.7, and 0.8, respectively. The dimensional method was used to estimate the pellets' relative green density (R.G.D) and relative sintered density (R.S.D).

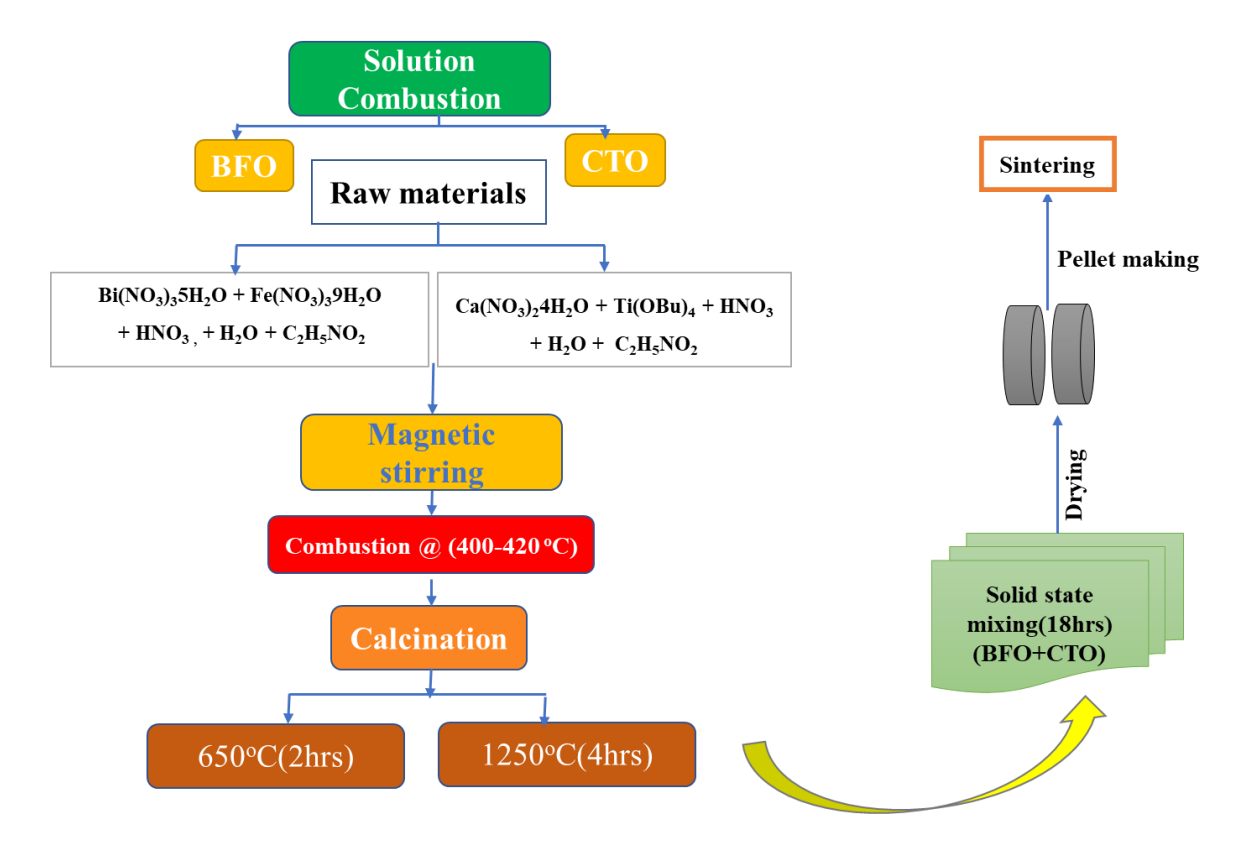


Fig. 4.12 Flow chart for synthesis, and processing of BFO-CTO

### 4.7 Density measurement

The densities of the sintered pellets were calculated using the dimensional method. The dimensions of the sintered samples were measured using a digimatic micrometer of precision 0.001 mm. The average ø and t were estimated from 4 measurements, and the sample volume was calculated. The mass of the sintered pellets was taken from an analytical weighing balance machine of precision 0.1 mg. The weight of the sintered sample was considered as dry weight.

#### 4.8 Electroding

Sintered high-density pellets were polished using fine emery paper to obtain a flat surface. The disks, after polishing were silver (Ag) – palladium (Pd) coated for electrical conductivity. The polished samples were coated with Ag-Pd viscous gel gently on the two sides of the samples, and thermal treatment was carried out at 110 °C for 20 minutes in order to dry the applied Ag-Pd solution. We shall ensure the coating is uniform and stick strongly to the surface of the samples.

The Ag-Pd paste-coated samples were heated at 550°C to dry the silver-palladium paste on the pellets completely. The conductivity of each electrode was measured using a digital multimeter and confirmed the non-contact between the two sides of the electrodes. Magnifying glass (25X)

was also used to see, if there was any contact between the two sides of the samples for further confirmation.

B1: 20BF0+80CTO (RFS)							
Load (T)	Мра	Temp(°C)	R.G.D (%)	Bulk density(g/cc)	R.S.D (%)		
2.5		1140/2hrs	59	2.5901	69		
3	374.586	1140/4hrs	62	2.7218	68		
3.5	437.017	1140/4hrs	66	2.8974	71		
4	499.448	1140/4hrs	67	2.9413	70		
4.5	561.879	1140/4hrs	69	3.0291	73		
5	624.31	1140/4hrs	69	3.0291	67		
Crack •							
B2: 20BF0+80CTO (RFS)							
Load (T)	Мра	Temp(°C)	R.G.D (%)	Bulk density(g/cc)	R.S.D (%)		
3.5	437.017	1200/4hrs	60	2.634	74		
4	499.448	1200/4hrs	64	2.8096	75		
4.5	561.879	1240/4hrs	66	2.8974	76		
		B3: 20BF	0+80CTO (	MWS)			
Load (T)	Мра	Temp (°C)	R.G.D (%)	Bulk density(g/cc)	R.S.D (%)		
3.5	437.017	1100/20min	64	2.8096	77		
4	499.448	1000/20min	66	2.8974	68		
4.5	561.879		66	2.8974			
5	624.31		66				
B4: 20BF0+80CTO (MWS)							
Load (T)	Мра	Temp (°C)	R.G.D (%)	Bulk density(g/cc)	R.S.D (%)		
4.5	561.879	1200/20min	66		84		
4.5	561.879	1240/20min	66		90		
4.5	561.879	1280/20min	66	4.1464344	94.28		
4.5	561.879	1280/20min	66	4.149513	94.35		
4.5	561.879	1280/20min	66	4.2436302	96.49		

B1: 30BF0+70CTO (RFS)							
Load (T)	Мра	Temp(°C)	R.G.D (%)	Bulk density(g/cc)	R.S.D (%)		
3	374.586	1140/4hrs	58	2.7028	78		
3.5	437.017	1140/4hrs	61	2.8426	80		
4	499.448	1140/4hrs	64	2.9824	85		
4.5	561.879	1140/4hrs	66	3.0756	80		
	B2: 30BF0+70CTO (RFS)						
Load (T)	Мра	Temp(°C)	R.G.D (%)	Bulk density(g/cc)	R.S.D (%)		
3.5	437.017	1200/4hrs	66.5	3.0989	86		
4	499.448	1200/4hrs	67	3.1222	87		
4.5	561.879	1200/4hrs	68	3.1688	90		
	B3: 30BF0+70CTO (MWS)						
Load (T)	Мра	Temp(°C)	R.G.D (%)	Bulk density(g/cc)	R.S.D (%)		
3.5	437.017	1100/20min	65	3.029	75		
4	499.448	1200/20min	66	3.0756	93		
4.5	561.879	1140/20min	68	3.1688	85		
B4: 30BF0+70CTO (MWS)							
Load (T)	Мра	Temp(°C)	R.G.D (%)	Bulk density(g/cc)	R.S.D (%)		
4.5	561.879	1180/20min	68	4.41342236	94.52		
4.5	561.879	1180/20min	68	4.436021772	95.004		
4.5	561.879	1180/20min	68	4.53482416	97.12		

B1: 40BF0+60CTO (RFS)							
Load (T)	Мра	Temp(°C)	R.G.D (%)	Bulk density(g/cc)	R.S.D (%)		
3	374.586	1140/2hrs	62	3.0814	75		
3.5	437.017	1140/4hrs	66	3.2802	79		
4	499.448	1140/4hrs	68	3.3796	82		
4.5	561.879	1140/4hrs	68	3.3796	84		
	B2: 40BF0+60CTO (RFS)						
Load (T)	Мра	Temp(°C)	R.G.D (%)	Bulk density(g/cc)	R.S.D (%)		
3.5	437.017	1200/4hrs	65	3.2305	92		
4	499.448	1200/4hrs	66	3.2802	93		
4.5	561.879	1200/4hrs	67	3.3299	93		
		B3: 40BI	F0+60CTO (	MWS)			
Load (T)	Мра	Temp(°C)	R.G.D (%)	Bulk density(g/cc)	R.S.D (%)		
3.5	437.017	1100/20min	64	3.1808	89		
4	499.448	1140/20min	66	3.2802	93		
4.5	561.879	1140/20min	67	3.3299	94.88		
	B4: 40BF0+60CTO (MWS)						
Load (T)	Мра	Temp(°C)	R.G.D (%)	Bulk density(g/cc)	R.S.D (%)		
4.5	561.879	1140/20min	67	4.677816	94.88		
4.5	561.879	1140/20min	67	4.777344	96		
4.5	561.879	1140/20min	67	4.79277084	96.31		

Fig. 4.13 Comparison between resistance furnace sintering (RFS) and microwave sintering (MWS) techniques and optimization of sintering temperature conditions of (1-x) BFO-xCTO (x = 0.6, 0.7, and 0.8)

The reason for choosing the MWS technique is discussed in detail in the results and discussion section.

#### 4.9 The characterization techniques used in the present investigation

- ➤ Thermogravimetric analysis (TGA) of the samples was carried out using a thermal analyser (SDT Q600 V20.9 Build 20 Germany) up to 1200°C at a heating rate of 10°C/min.
- The crystal structure of the samples was identified by powder X-ray diffraction (XRD) using Cu-Kα radiation (λ= 0.154 nm) (Bruker D8 advance, AXS, D76181 Karlsruhe, Germany). The Rietveld refinement of the powder diffraction data analysed the crystal structure. The diffraction patterns were recorded in the 2θ range of 20 to 80° with a step size of 0.02° and a counting time of 0.8s/step.
- ➤ Microstructural analysis was performed using FESEM (FEI Nova Nano SEM 450) and FESEM JEOL JSM7100F. Elemental composition studies were conducted using EDS (EDAX, AMETEK, USA) attached with FESEM.
- Leakage current density (J) measurements were carried out using an I-V characterization system (Keithley 4200-SCS Semiconductor Parameter Analyzer, USA).
- $\triangleright$  Dielectric permittivity and loss tangent (tan  $\delta$ ) were measured using an Impedance analyzer (Agilent- E4990A-010) in the frequency range 20 Hz-10 MHz. AC voltage amplitude of 1 V<sub>(rms)</sub> was used for the dielectric characterizations.
- Frequency dependence of the dielectric properties of ceramics was investigated from 20 Hz to 1MHz using a Hewlett Packard HP4284A LCR meter and from 1 MHz to 1.8 GHz using a HP4291A impedance analyzer, at room temperature. Additionally, a third measurement was done from 20 Hz to 100 MHz with a Keysight E4990A impedance analyser to confirm the dielectric measurement accuracy.
- The chemical valance states of the Fe were determined by X-ray Photoelectron Spectrometer (XPS) (Thermo Fisher Scientific Pvt. Ltd. UK, K-Alpha).
- ➤ The samples' current-voltage (I-V) hysteresis curve characteristics have been carried out using Keithley dual source Meter (Model: 2410-C).
- ➤ Temperature-dependent dielectric permittivity and loss tangent were measured using the impedance analyzers (Agilent- E4990A-010), and high-frequency dependent dielectric properties were measured using broadband dielectric spectroscopy (Alpha/Beta Analyzer 1Hz to 2×10<sup>7</sup> Hz and high-frequency analyzer 10<sup>6</sup> to 10<sup>9</sup> Hz concept 80, Novocontrol Technologies GmbH & Co, Germany).
- ➤ The ferroelectric response of the sintered samples was measured using Premier II Ferroelectric Tester (Radiant Technology, USA).

# **REFERENCES**

- [1] M.N. Rahaman Ceramic Processing and Sintering, 2nd ed., revised and extended. New York: Marcel Dekker; 2003.
- [2] M.N. Rahaman. Sintering of Ceramics. Boca Raton, FL: CRC Press/Taylor & Francis; 2007.

## **CHAPTER - 5A**

#### RESULTS AND DISCUSSIONS

# 5A Structural, and high-frequency dielectric characterization of novel lead-free BFO-CTO, BFO-BZO, and BFO-STO ferroelectric ceramics

#### 5A. 1. Structural characterizations

Figures 5A.1, 5A.2, and 5A.3 show the XRD patterns of calcined powders of BFO, CTO, as received powders of STO, BZO and sintered pellets of BFO-BZO, BFO-CTO and BFO-STO. As evident from the powder diffraction pattern BFO crystallizes in rhombohedral phase (JCPDS card no. 01-086-1518) with very minor presence of Bi<sub>2</sub>Fe<sub>4</sub>O<sub>9</sub> as the impurity phase. CTO crystallizes in pure cubic phase (JCPDS card no. 03-065-3287) with no traceable impurity within the detection limit of powder XRD. The X-ray diffraction pattern of the prepared BFO and CTO powders agrees well with the reported literature [1, 2]. As received polycrystalline STO and BZO powders show phase pure cubic structure and well match with the JCPDS card nos. 00-006-0399 for BZO and 00-035-0734 for STO powder. A closer look at the XRD patterns of the sintered samples, BFO-BZO, BFO-CTO and BFO-STO reveals that they are solid solutions of the component phases with very rare occurrence of the Bi<sub>2</sub>Fe<sub>4</sub>O<sub>9</sub> as the impurity phase.

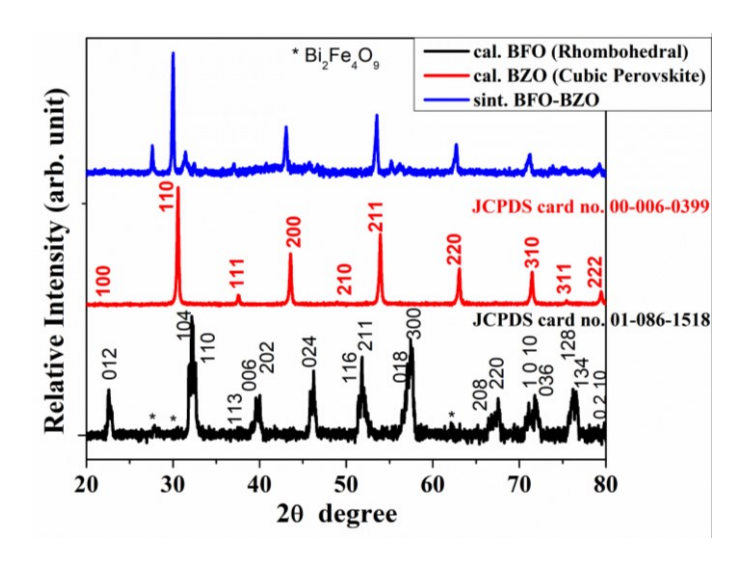


Fig 5A. 1 XRD patterns of calcined powders of BFO, BZO and sintered pellet of BFO-BZO

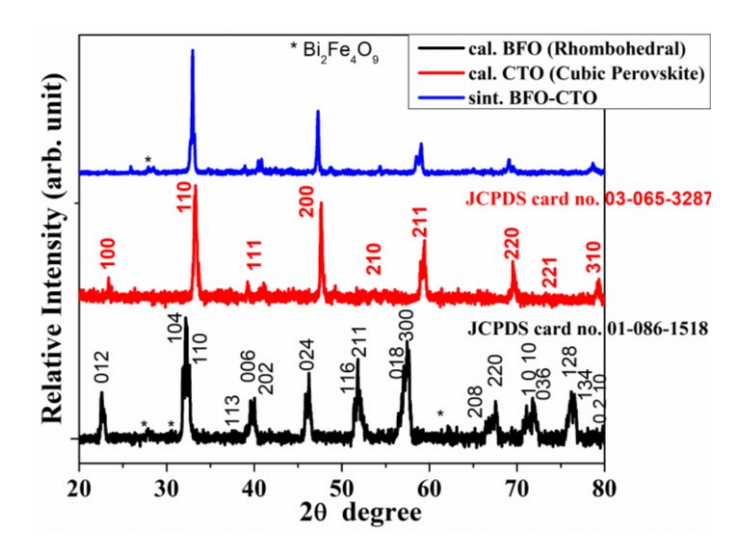


Fig 5A. 2 XRD patterns of calcined powders of BFO, CTO and sintered pellet of BFO-CTO

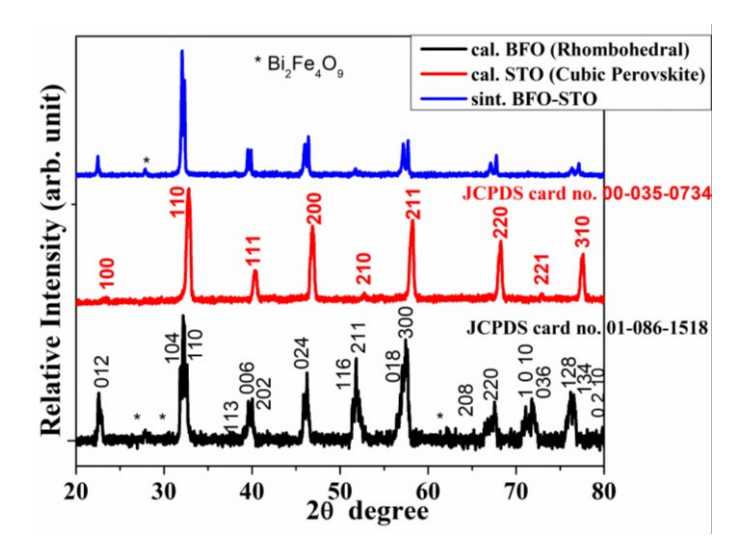


Fig 5A. 3 XRD patterns of calcined powders of BFO, STO and sintered pellet of BFO-STO

While the XRD pattern of BFO-STO contains peaks from diffracting planes of BFO and STO simultaneously, those of BFO-BZO and BFO-CTO are dominated by the peaks from diffracting planes of BZO and CTO, respectively. The shifting and magnitude of shifting of the diffraction peaks of BZO and CTO to lower angles correlates well with the larger ionic radii of  $Ba^{+2}$  and  $Ca^{+2}$  compared to ionic radius of  $Bi^{+3}$  ( $Bi^{+3} = 1.17$  Å (for 8 coordination) while  $Ba^{+2} = 1.61$  Å (for 12 coordination), and  $Ca^{+2} = 1.34$  Å (for 12 coordination)). The different behaviour of BFO-STO, where ionic radius of  $Sr^{+2}$  (1.44 Å for 12 coordination) is in between those of  $Ba^{+2}$  and  $Ca^{+2}$ , is not known to us in this investigation. However, a very careful analysis of the high resolution XRD data of all the three sintered samples show different level of impurity content in them. Whereas, BFO-STO shows very minimal impurity content in the

sintered sample, BFO-BZO and BFO-CTO contain more impurities, as shown in Fig. 5A.4, in them.

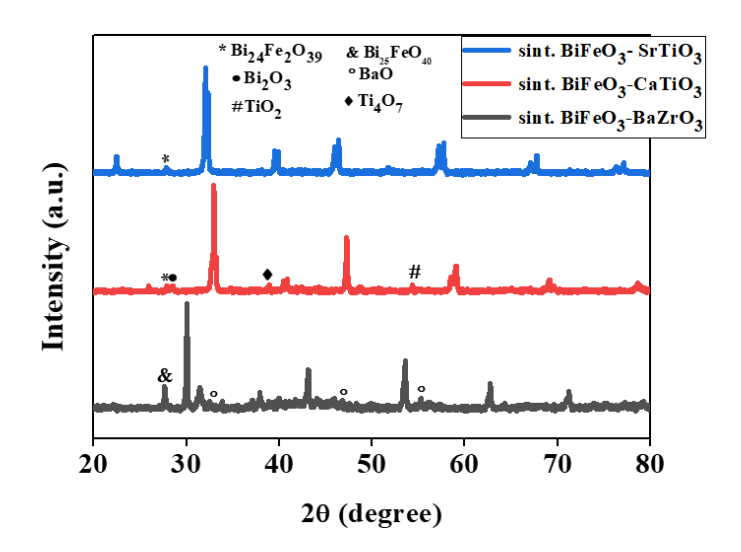


Fig 5A. 4 XRD patterns of sintered pellets of BFO-BZO, BFO-CTO and BFO-STO

#### 5A. 2. Microstructural characterizations

The microstructure of the fractured surface of the sintered pellets is shown in Figures 5A.5, 5A.6, and 5A.7. The grain size distributions have also been shown in the inset of the microstructures. As can be seen in Fig. 5A.5, a nearly bi-modal distribution with spherical morphology of the grains is seen in the sintered microstructure of BFO-BZO sample. A fairly wide grain size distribution, as seen in inset of Fig. 5A.5, with mean grain size  $D_{50} \sim 325$  nm has been observed for sintered BFO-BZO sample.

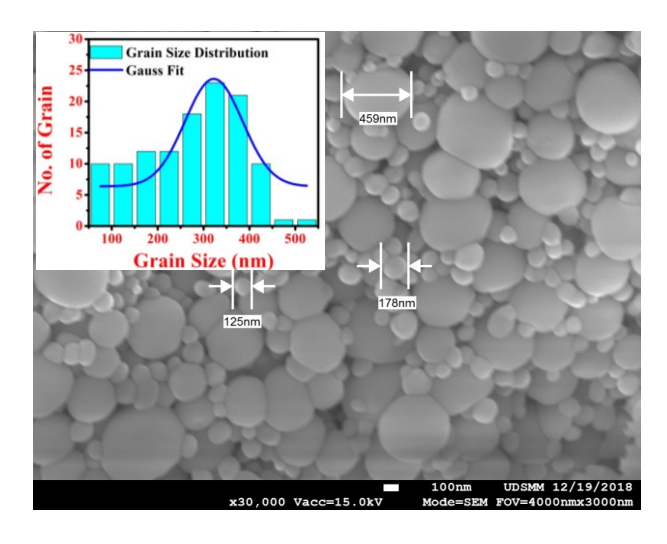


Fig 5A. 5 Microstructure of the fractured surface of the sintered pellets of BFO-BZO. The respective inset shows the mean grain size and the distribution of grain sizes in the sintered pellets.

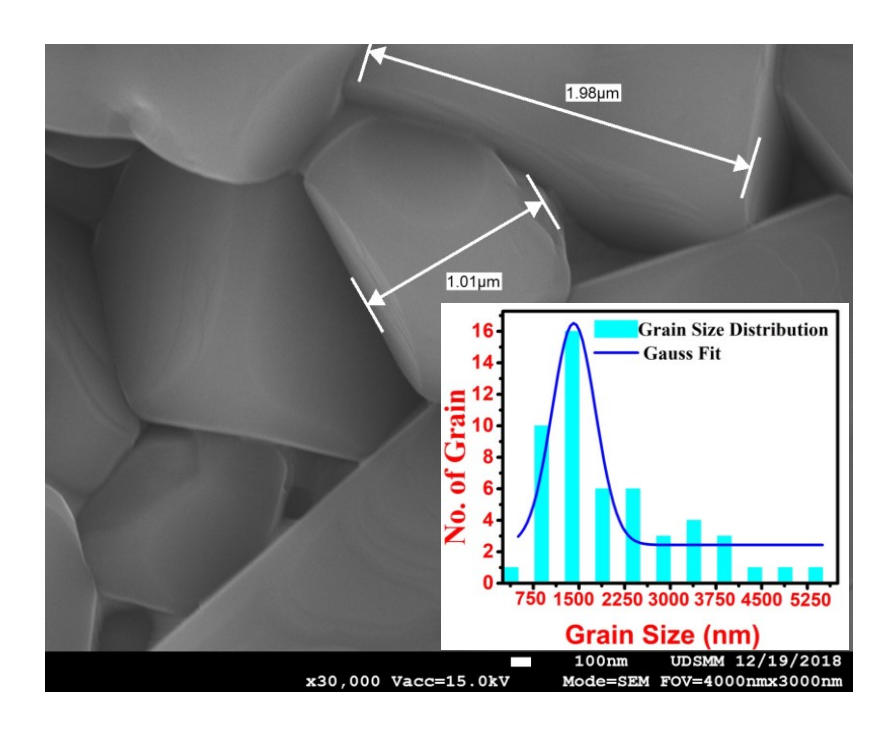


Fig 5A. 6 Microstructure of the fractured surface of the sintered pellets of BFO-CTO. The respective inset shows the mean grain size and the distribution of grain sizes in the sintered pellets.

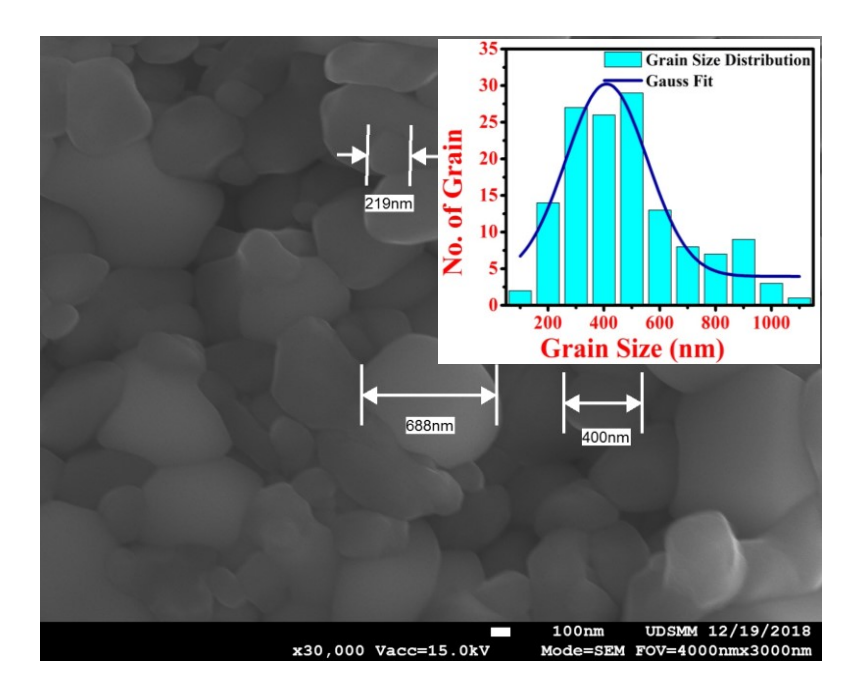


Fig 5A. 7 Microstructure of the fractured surface of the sintered pellets of BFO-STO. The respective inset shows the mean grain size and the distribution of grain sizes in the sintered pellets.

A difference in sintering ability and grain growth kinetics of BFO and BZO phases can lead to such sintered microstructure with nearly bimodal grain size distribution. Microstructure of the sintered BFO-CTO sample, as shown in Fig. 5A.6, is quite different. A nearly

homogeneous structure with faceted grains and relatively narrow grain size distribution, as shown in inset of Fig. 5A.6, are seen in the sintered microstructure. Average grain size,  $D_{50} \sim 1.5 \mu m$ , which is nearly 5 times larger than BFO-BZO sintered grains, is observed. A mean grain size,  $D_{50} \sim 400$  nm with relatively wider grain size distribution has been observed for sintered BFO-STO samples and is shown in Fig. 5A.7. Not much faceting of the grains is observed for this sample. A difference in sintering behavior of BFO and STO might lead to such heterogeneous microstructure with limited densification.

#### 5A. 3. Dielectric characterizations

All the samples were characterized in a large frequency range, 20 Hz to 1.8 GHz. The dielectric properties, i.e. the dielectric constant and the loss tangent were calculated from the measurements of the sample resistance and capacitance. Fig. 5A.8 shows the frequency dependent dielectric constant and loss tangent for BFO-BZO. All the data points, obtained from 3 different impedance analyzers for covering the entire frequency range, are plotted in Fig. 5A.8. At lower frequency, from 20 to 1 kHz, the dielectric constant value slowly decreases from 500 to 100. This behavior at low frequency is commonly observed in ferroelectric ceramics and is generally associated with extrinsic effects related to fabrication parameters such as pellet preparation and sintering conditions. In fact, these parameters influence the final microstructure of the ceramic samples, where holes, pores and large grain boundaries can act as space-charge areas. These space-charge effects can have an important influence on the evolution of the dielectric constant at low frequency because electric carriers can be trapped in structural defects. These space-charge effects generate additional capacitances that increase the measured capacitance of the sample. Dielectric properties of ferroelectric materials are very sensitive to ionic substitution and defects. Holes, pores, and large grain boundaries are the influential parameters of dielectric constant and dielectric loss, from the critical observation of dielectric measurements it can be noticeable that these parameters will act as space-charge areas

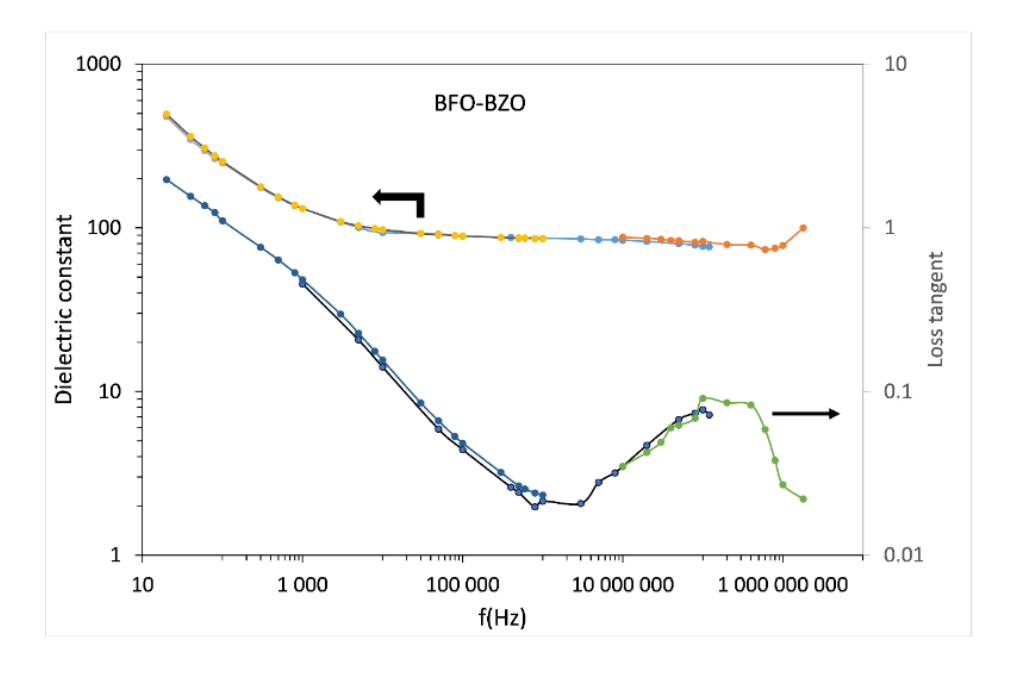


Fig 5A. 8 Frequency dependence of the dielectric constant and loss tangent for BFO-BZO sample sintered at 1100 °C/2h

Beyond 1 kHz, the dielectric constant value becomes quite constant and close to 100 until 1 GHz. This response of the BFO-BZO sample is encouraging because the conditions of the sample preparation have not yet been optimized at this stage of our study. And a better characteristic i.e., almost frequency independent dielectric constant in the entire frequency range studied from 20 Hz to 1.8 GHz could be obtained with a better density of the ceramic.

The loss tangent value sharply decreases from 1 to 0.02 in the frequency range 20 Hz to 5 MHz followed by an increase to 0.08 at f=500 MHz. Beyond 500 MHz, the decrease in loss tangent is due to an artifact. This part of the loss is most probably due to a resonance phenomenon, which is defined by the inductance and capacitance of the measured sample. The resonance frequency is effectively given by the relation,  $f_r=1/\left(2.\pi.L_s.C_s\right)$  where  $L_s$  is the inductance of the measurement device and  $C_s$  is the sample capacitance. The measuring device holds the pellet and makes the connection between the sample and the measurement cables. For minimizing the effect of this resonance, the resonance frequency must be as high as possible. In this way, the electrical connections must be as short in length as possible and the dimensions of the measured sample must be adapted to the frequency range. For high frequency measurements, the pellet diameter must be as low as possible, while the thickness must be high, of the order of few millimetres.

In Fig. 5A.8 the resonance frequency is not completely observed. Instead, the beginning of the resonance effect beyond 500 MHz is observed, which induces a decrease in the loss tangent value at the highest frequencies of the measurement range.

Figure. 5A.9 shows the variation in dielectric constant ( $\epsilon'$ ) and loss tangent as a function of frequency for the sintered BFO-CTO sample. At low frequency, from 20 to 1 kHz, the dielectric constant value slowly decreases from 2000 to 200. Then from 1 kHz to 100 kHz, the  $\epsilon'$  value slowly decreases to 90, which remains almost stable at higher frequencies. Beyond 800 MHz, the  $\epsilon'$  evolution is due to a resonance effect.

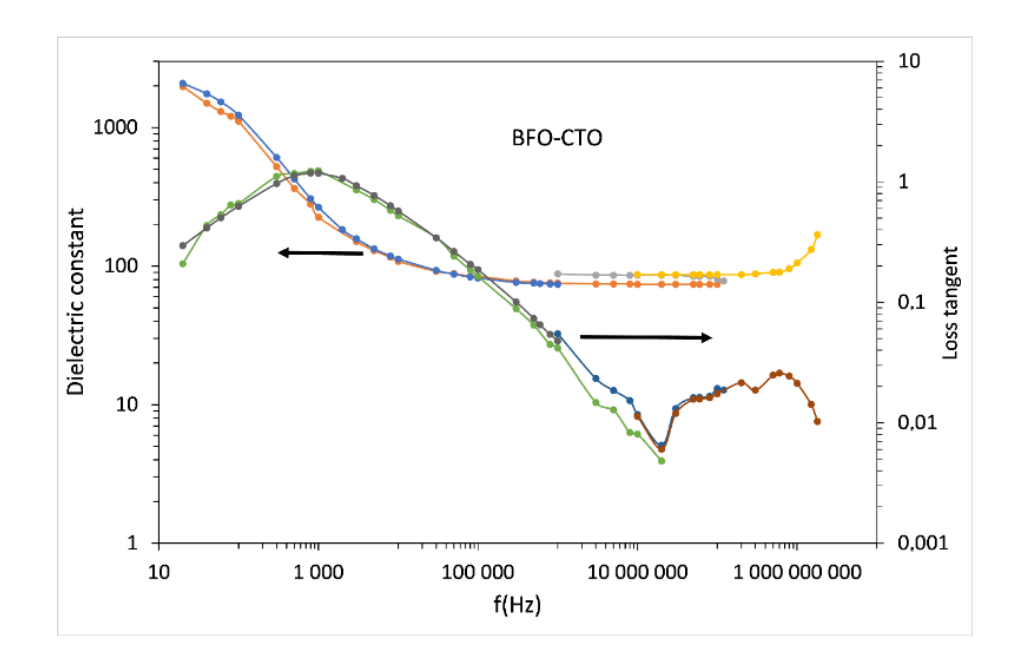


Fig 5A. 9 Variation in dielectric constant and loss tangent as a function of frequency for the sintered BFO-CTO sample.

The loss tangent shows a completely different behaviour. In fact, the loss tangent exhibits a peak in the low frequency part. Beyond this peak, the  $\tan\delta$  value decreases from 1 at 1 kHz to  $5\times10^{-3}$  at 50 MHz. Then at higher frequencies ( $\geq 10$  MHz), the loss tangent increases from 0.01 to 0.028. Beyond 800 MHz, the decrease in the loss tangent is due to the resonance phenomenon, as described previously. From a closer look at the dielectric data in the entire frequency range it is seen that the low frequency loss behaviours are different than those of the BFO-BZO sample. In order to understand the behaviours of the sample at lower frequencies the dielectric data up to 1 MHz were carefully analyzed and is separately given in Fig. 5A.10.

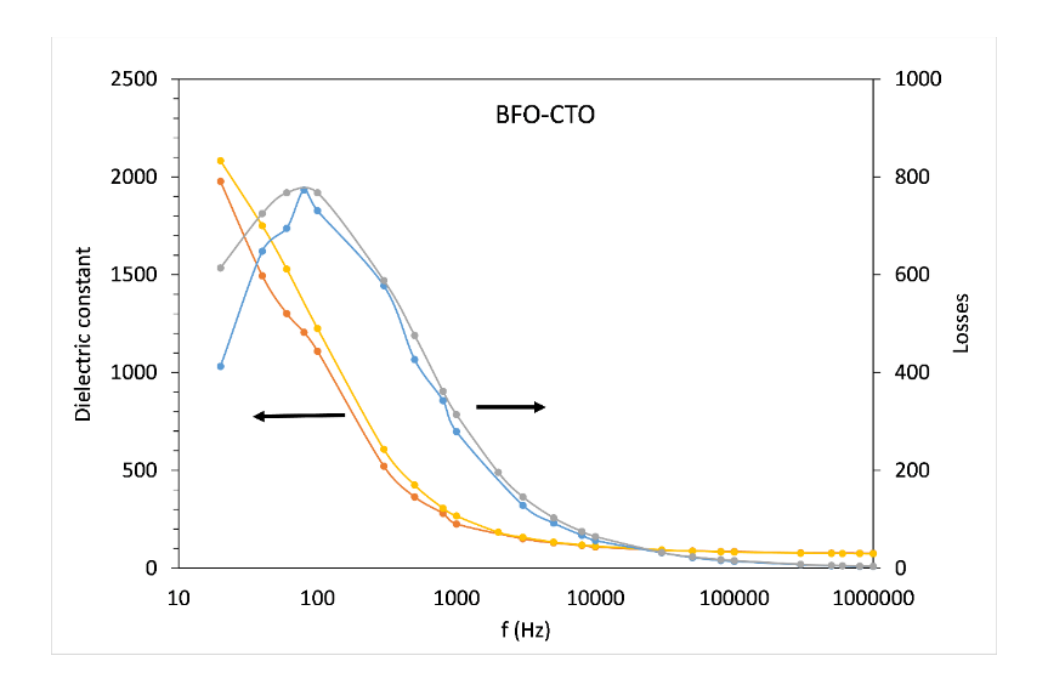


Fig 5A. 10 Low frequency, up to 1 MHz, dielectric behaviours of sintered BFO-CTO sample

The losses  $\varepsilon''$  are the imaginary part of the complex dielectric permittivity. In Fig. 5A.10 the loss peak is observed for BFO-CTO sample which is approximately cantered at  $f \sim 100$  Hz. This kind of behaviours is the characteristic of dielectric relaxation phenomena. At low frequency, this dielectric relaxation is generally associated with the Maxwell-Wagner (MW) type interfacial polarization effect. Maxwell-Wagner effect is related to the displacement and accumulation of electrical charges that significantly influence the dielectric properties. This type of dielectric relaxation is therefore probably due to an extrinsic effect, and not related to the intrinsic property of the material. Electric charges can be accumulated around the defects in the sample, such as grain boundaries, porosities, or areas where the metallic electrode is not in contact with the bulk ceramic, causing space-charge effects at low frequency generally called the Maxwell-Wagner effect. The occurrence of MW type interfacial polarization effect leading to low frequency loss peak in the dielectric spectrum in BFO-CTO sample correlates well with the physical structure of this material. Among the 3 solid solutions studied in this investigation, BFO-BZO, BFO-CTO, and BFO-STO, BFO-CTO has shown the least volume shrinkage (~5%), or in other words the porosity content should be highest in this sample. Presence of porosities, voids and grain boundaries are ideal locations for trapping of electrical charge carriers leading to space charge polarization. The effect becomes more severe if these potential charge carrier traps are located on the surface of the sample. The electrode material gets deposited on those areas making them more vulnerable to produce space change effect.

Fig. 5A.11 presents the variation in dielectric constant and loss tangent as function of frequency for the sintered BFO-STO sample. The dielectric constant slowly decreases from 400 to 200 in the large frequency range 20 Hz  $\leq$  f  $\leq$  500 MHz. Beyond 500 MHz, the change in  $\epsilon'$  is due to the resonance effect. The loss tangent value continuously decreases from 0.4 to 0.05 in changing frequencies from 20 Hz to 100 kHz.

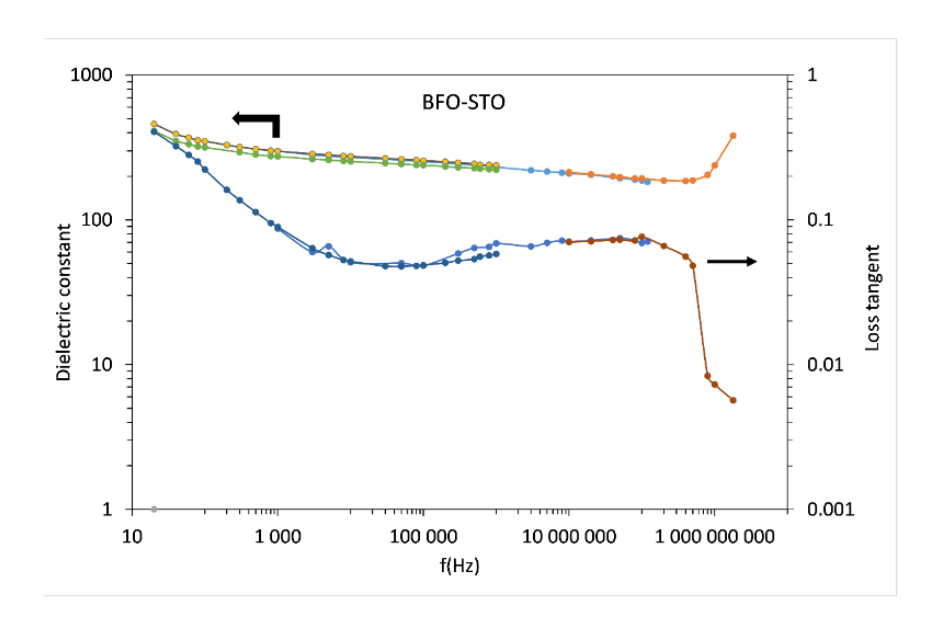


Fig 5A. 11 Frequency dependent dielectric constant and loss tangent variation for the sintered (1100 °C/2h) BFO-STO sample

Then the loss tangent value remains quite stable at 0.07 until 800 MHz. Beyond 800 MHz, the decrease in loss tangent is due to an artifact. This part of the loss tangent curve is due to the resonance phenomenon, as described earlier.

# 5A. 4. Conductivity properties as a function of frequency

Figure. 5A.12 shows the frequency dependent a.c. conductivity of all the sintered samples. The different compositions show values ranging from 10<sup>-7</sup> to 10<sup>-1</sup> S/m from low to high frequency. Below 10 kHz, BFO-CTO shows the highest conductivity due to its high losses caused by the Maxwell-Wagner type interfacial polarization effect shown in Fig. 5A.12. Above 100 kHz, all plots show similar behaviours meaning that the conductivity mechanism is quite similar in all the 3 samples in the medium to high frequency range.

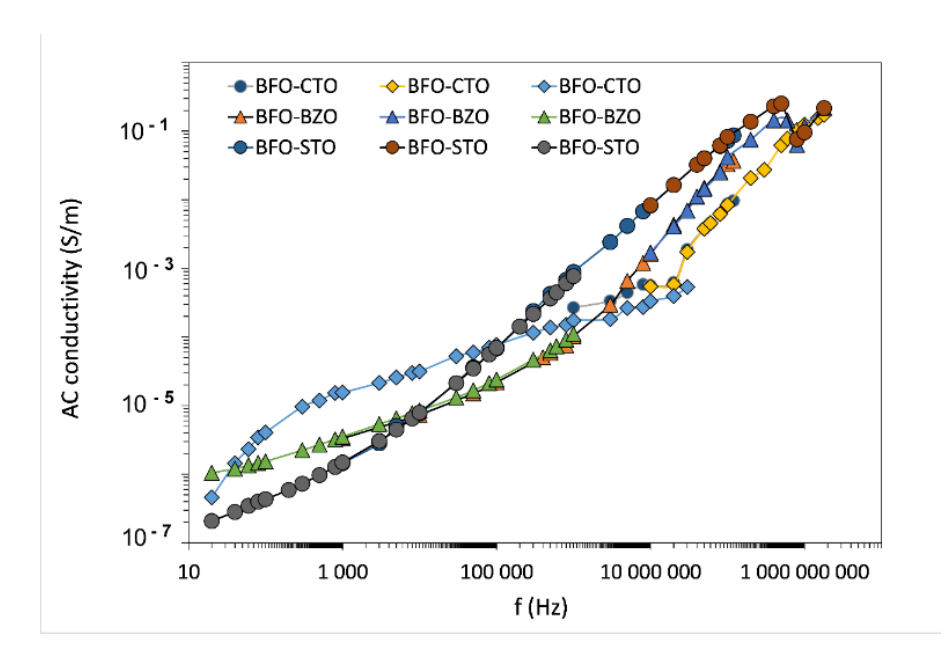


Fig 5A. 12 Frequency dependence of room temperature A.C. conductivity of the sintered BFO-BZO, BFO-CTO and BFO-STO samples. 3 labels of data points of each of the sample indicate that the estimated conductivity from the dielectric data has been collected from 3 different Impedance Analyzer to cover the entire frequency range

# 5A. 5. Discussion

All the compositions studied in this investigation have the potential for electrical energy storage and therefore worth to have a comparison of their suitability. Table 5A.1 below provides some values extracted from the dielectric characterizations of BFO-BZO, BFO-CTO and BFO-STO in the frequency range  $20~\text{Hz} \le f \le 1.8~\text{GHz}$ .

Table 5A. 1 Dielectric properties of BFO-BZO, BFO-CTO and BFO-STO at f = 10 kHz and 10 MHz

	BFO-BZO	BFO-CTO	BFO-STO
ε' (10 kHz)	100	112	255
ε' (10 MHz)	85	85	195
tanδ (10 kHz)	0.15	0.5	0.05
tanδ (10 MHz)	0.08	0.02	0.07

BFO-BZO and BFO-CTO show similar values of dielectric constant at low and high frequencies. Except the low-frequency part, where BTO-CTO shows a Maxwell-Wagner effect, BFO-BZO and BFO-CTO dielectric properties are almost similar in the entire frequency range. But, BFO-CTO gives better performance at higher frequencies with lower loss tangent values.

BFO-STO, on the other hand, shows a quite low dispersion of the dielectric constant value.  $\varepsilon'$  values are almost 2.3 times higher than those of BFO-BZO and BFO-CTO, at both low and high frequencies. The loss tangent value is quite stable in a large frequency range, with  $\tan \delta = 0.05$  at 10 kHz and 0.07 at 100 MHz.

The very different behaviours of BFO-STO can be related to its crystalline structure because its XRD pattern contains peaks from diffracting planes of BFO and STO simultaneously. In comparison, the diffraction patterns of BFO-BZO and BFO-CTO are dominated by the peaks from diffracting planes of BZO and CTO, respectively. The microstructure of the ceramics does not explain the similar behaviours of BFO-BZO and BFO-CTO. Indeed, BFO-BZO is composed of 2 types of grains, i.e., smaller grains ranging from 100 to 150 nm and bigger ones ranging from 400 to 500 nm. A difference in the starting particle sizes of BFO and BZO may lead to such sintered microstructure with heterogeneous grain size distribution. BFO-CTO, on the other hand, is composed of big pseudo-cubic grains with a  $D_{50} \approx 1.5 \ \mu m$ .

Researchers have been studying BZO and CTO ceramics for many years. BZO is well-known for having low dielectric constant values, i.e., in the range 30-40 [3]. But CTO offers higher values with  $\epsilon'\approx 140-160$  [4]. More recently BFO has attracted a great attention due to its numerous properties. Jun Lu et al. have shown from a very low-temperature dielectric measurements on BFO ceramic that the intrinsic value of the dielectric constant is close to 80 [5]. The measurement artifacts and ceramic microstructure, which are extrinsic contributions, have generally an influence on the dielectric properties at low and medium frequencies. So high frequency measurements can reveal the intrinsic properties of the material. Here BFO-BZO and BFO-CTO give a dielectric constant value at high frequency,  $\epsilon'=85$ , which is very close to that of BFO intrinsic value [5]. So, BFO properties seem to have a strong influence on the properties of BFO-BZO and BFO-CTO ceramics.

As highlighted earlier, BFO-STO behaves very differently. In fact, BFO-STO exhibits values of the dielectric constant that are closer to those reported for STO [6]. In fact, STO ceramic shows  $\varepsilon'$  values close to 300 at room temperature. This kind of dielectric constant values have been reported for films studied in the low-frequency range [7].

# REFERENCES

- [1] Wenqian Cao, Zhi Chen, Tong Gao, Dantong Zhou, Xiaonan Leng, Feng Niu, Yuxiang Zhu, Laishun Qin, Jiangying Wang, Yuexiang Huang, Rapid synthesis of single-phase bismuth ferrite by microwave-assisted hydrothermal method, Materials Chemistry and Physics.175(2016)1-5. https://doi.org/10.1016/j.matchemphys.2016.02.067.
- [2] Xianfeng Yang, Ian D. Williams, Jian Chen, Jing Wang, Huifang Xu, Hiromi Konishi, Yuexiao Pan, Chaolun Liang Mingmei Wu, Perovskite Hollow Cubes: Morphological Control, Three-dimensional Twinning and Intensely Enhanced Photoluminescence, Journal of Materials Chemistry. 18 (2008). https://doi.org/10.1039/b808396g.
- [3] H. Padma Kumar, C. Vijayakumar, Chandy N. George, Sam Solomon, R. Jose, J.K. Thomas, J. Koshy. Characterization and sintering of BaZrO3 nanoparticles synthesized through a single-step combustion process, Journal of Alloys and Compounds. 458 (2008) 528–531. https://doi.org/10.1016/j.jallcom.2007.04.032.
- [4] Pashkin, S Kamba, M Berta, J Petzelt, G D C Csete de Györgyfalva, H Zheng, H. Bagshaw, I M Reaney, High frequency dielectric properties of CaTiO3-based microwave ceramics, J. Phys. D: Appl. Phys. 38 (2005) 741–748. https://doi.org/10.1088/0022-3727/38/5/012.
- [5] Jun Lu, A. Günther, F. Schrettle, F. Mayr, S. Krohns, P. Lunkenheimer, A. Pimenov, V. D. Travkin, A. A. Mukhin, A. Loidl, On the room temperature multiferroic BiFeO3: magnetic, dielectric and thermal properties, The European Physical Journal B. 75 (2010) 451–460. https://doi.org/10.1140/epjb/e2010-00170-x.
- [6] J. Petzelt, T. Ostapchuk, I. Gregora, I. Rychetsky, S. Hoffmann-Eifert, A. V. Pronin, Y. Yuzyuk, B. P. Gorshunov, S. Kamba, V. Bovtun, J. Pokorny, M. Savinov, V. Porokhonskyy, D. Rafaja, P. Vanek, A. Almeida, M. R. Chaves, A. A. Volkov, M. Dressel, R. Waser, 2001. Dielectric, infrared, and Raman response of undoped SrTiO3 ceramics, Evidence of polar grain boundaries. Physical Review. 64, 184111. <a href="https://doi.org/10.1103/physrevb.64.184111">https://doi.org/10.1103/physrevb.64.184111</a>.
- [7] Hao Pan, Jing Ma, Ji Ma, Qinghua Zhang, Xiaozhi Liu, Bo Guan, Lin Gu, Xin Zhang, Yu-Jun Zhang, Liangliang Li, Yang Shen, Yuan-Hua Lin1, Ce-Wen Nan, Giant energy density and high efficiency achieved in bismuth ferrite-based film capacitors via domain engineering, Nature Communications, 9 (2018). <a href="https://doi.org/10.1038/s41467-018-04189-6">https://doi.org/10.1038/s41467-018-04189-6</a>.

# **CHAPTER - 5B**

# 5B Investigation of Structural, Electrical, and Dielectric Properties of Lead-Free (BiFeO<sub>3</sub>)<sub>(1-x)</sub> – (CaTiO<sub>3</sub>)<sub>x</sub> Ferroelectric Ceramics

# 5B. 1. Structural characterization of calcined BFO and CTO

X-ray diffraction patterns of the calcined BFO and CTO powder samples in the 2θ range from 20°C to 80°C are shown in Fig. 5B.1. The powder diffractogram of BFO powder calcined at 550°C for 2 h, and 600°C for 2 h revealed the formation of BFO phase along with Bi2Fe4O9 as the impurity phase. The diffraction peaks of BFO calcined at 650°C for 2 h, indexed to the Rhombohedral (matches with JCPDS card no. 01-86-1518) crystal structure with R3c space group symmetry with no traceable impurity within the detection limit of powder XRD is shown in Fig. 5B.1a. The powder diffractogram of CTO powder calcined at 1150°C for 4 h, and 1200°C for 4 h revealed CTO phase along with CaO impurity phase. The diffraction peaks of CTO calcined at 1250°C for 4 h, indexed to the Orthorhombic (matches with JCPDS card no. 88-0790) crystal structure with Pbnm space group symmetry with no traceable impurity within the detection limit of powder XRD is shown in Fig. 5B.1b.

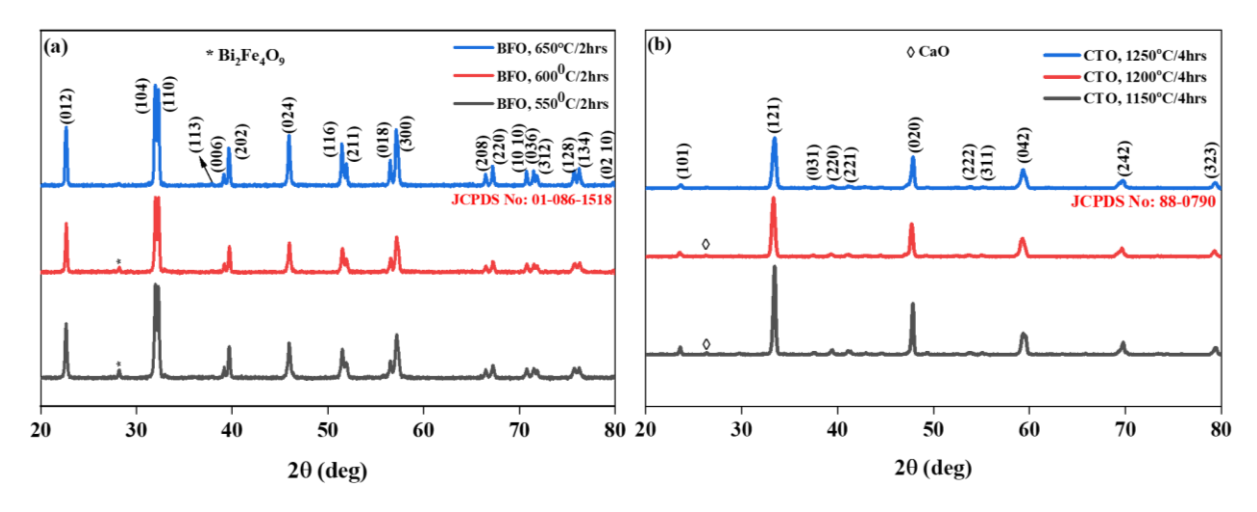


Fig 5B. 1 X-ray diffractogram of calcined (a) BFO and (b) CTO powder samples

# 5B. 2. Thermogravimetry analysis

Fig. 5B.2. Shows the thermogravimetry (TG) results of representative (BFO)<sub>(1-x)</sub> – (CTO)<sub>x</sub> (x = 0.6, and 0.8) samples, in which the mass of the sample is monitored against the temperature change where the powder samples were kept under identical heating atmosphere.

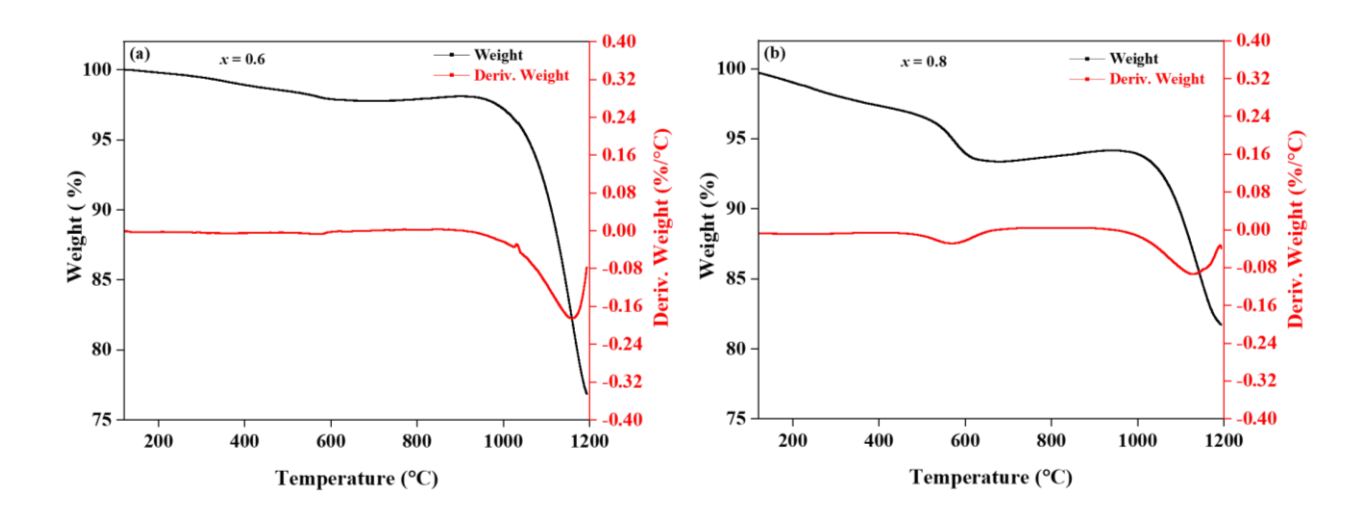


Fig 5B. 2 Thermogravimetric analysis (TGA) of (BiFeO<sub>3</sub>)<sub>(1-x)</sub> – (CaTiO<sub>3</sub>)<sub>x</sub> ceramics: (a) x = 0.6 and (b) x = 0.8

The approximate sintering temperatures were estimated from the derivative weight% curve (endothermic curve), where the significant changes were observed within the temperature ranges from  $1020^{\circ}$ C to  $1200^{\circ}$ C for x = 0.6, as shown in Fig. 5B.2a, and from  $1050^{\circ}$ C to  $1200^{\circ}$ C for x = 0.8 as shown in Fig. 5B.2b. The thermal changes observed at  $580^{\circ}$ C to  $620^{\circ}$ C for x = 0.8 is not known to the authors as of now.

# **5B. 3. Sintering temperature difference of BFO and CTO and choosing the MWS technique**

Whereas BFO is known to be sintered at ~850-900 °C, the sintering temperature for CTO is ~1350 °C. With ~500°C difference in the sintering temperature getting a good sintered density of the BFO-CTO solid solution sintered at a particular temperature by conventional solid-state sintering is quite a challenging task. Conventional sintering in resistive heating furnace was tried in the temperature range 1100-1280 for 4h. Variation in relative sintered density (% RSD) with sintering temperature is shown in Fig. 5B.3 for x = 0.6 (a), 0.7 (b) and 0.8 (c). An increase in RSD from 84-93%, 72-90% and 68-80% has been observed for x = 0.6, 0.7 and 0.8, respectively, with increase in sintering temperature from 1100 to 1280°C. The increase in sintered density with increase in temperature is least for x = 0.8 and highest for x = 0.6, which is due to higher CTO content in the sample which is known to sinter at much higher temperature compared to the sintering temperature employed in the current study. Such poor sintering in the conventional resistive heating furnace resulted in porous microstructure with inhomogeneous grain growth as shown in Figure 5B.4 for two representative samples with x = 0.6 (a) and x = 0.8 (b).

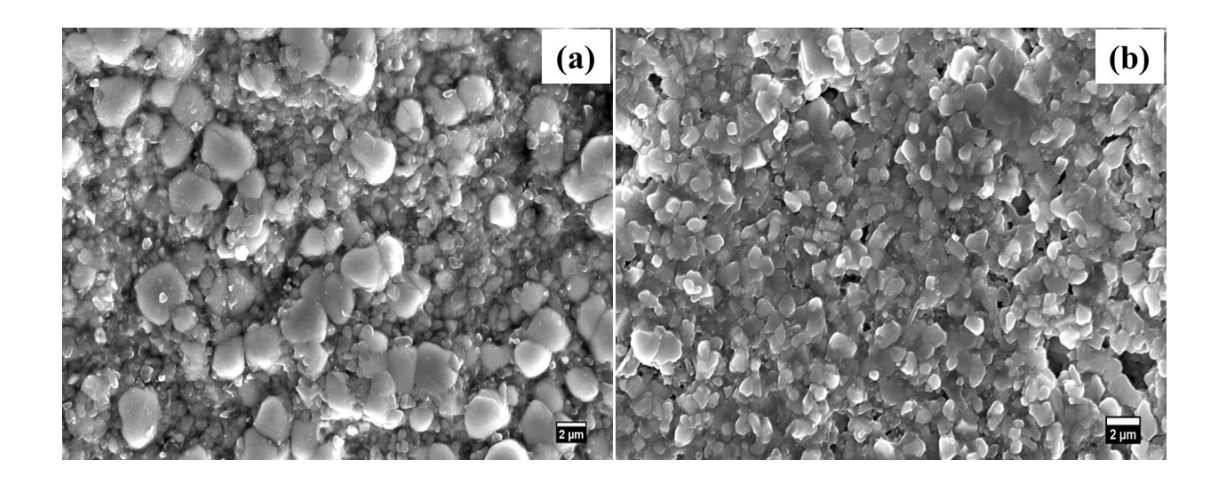


Fig 5B. 3 FESEM micrographs of  $(BiFeO_3)_{(1-x)} - (CaTiO_3)_x$  conventional sintered samples: (a) x = 0.6, and (b) x = 0.8

To overcome this problem of conventional sintering in resistive heating furnace microwave sintering was tried to sinter the samples.

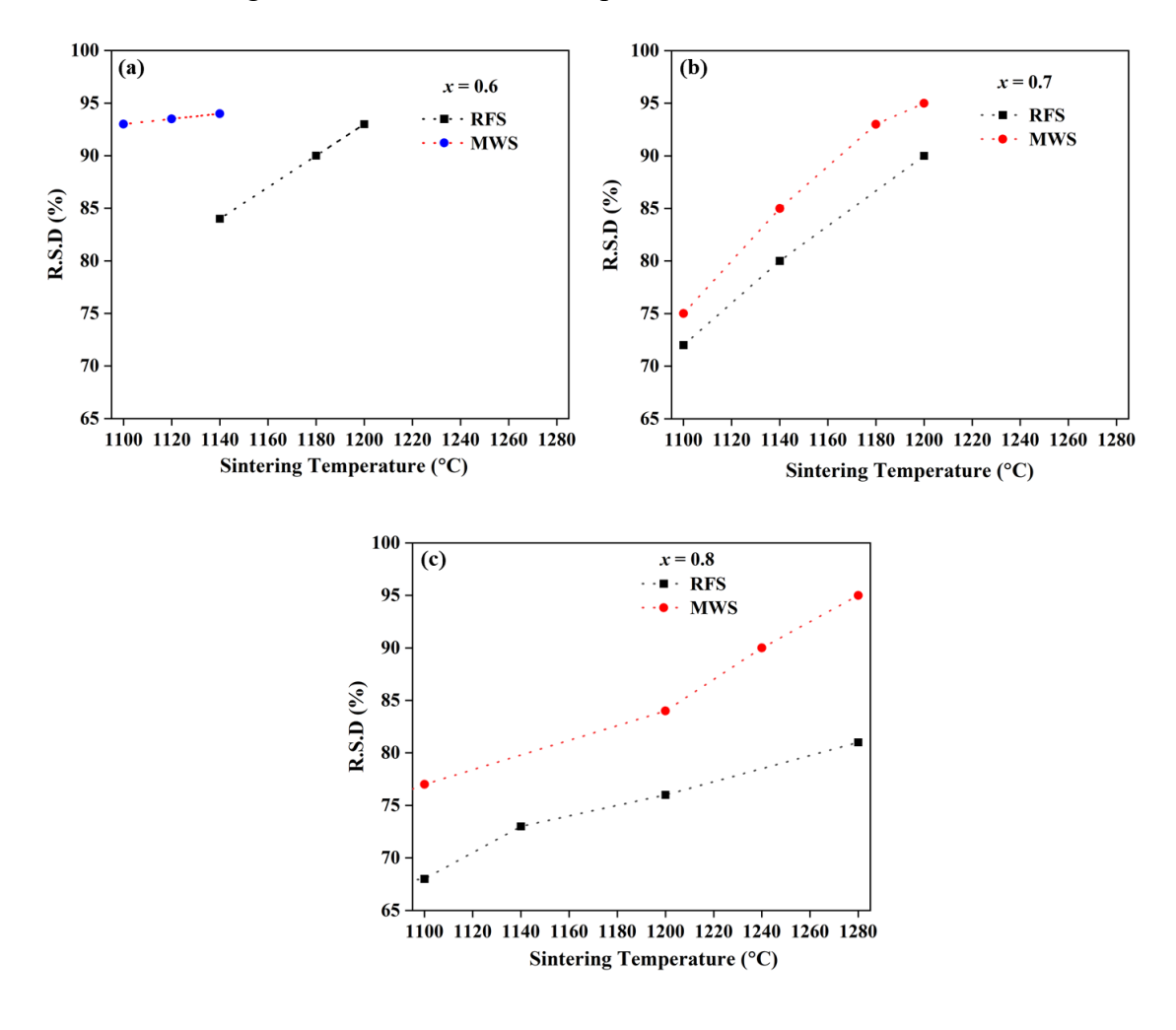


Fig 5B. 4 Relative sintered density of (BiFeO<sub>3</sub>)  $(1-x) - (CaTiO_3) x$ , MWS vs RFS for (a) x = 0.6, (b) x = 0.7, and (c) x = 0.8. Dotted lines are the guide to the eye

Microwave sintering is known to produce volumetric heating of the sample provided the material to be sintered couples effectively with the microwave field. If the material responds well to the microwave radiation, then very high sintered density with dense microstructure is possible in a relatively shorter time than conventional sintering. Microwave sintering was carried out at temperatures  $1100-1280^{\circ}$ C for just 20 mins and the %RSD of the microwave sintered samples has been plotted and compared with those obtained from conventional sintering in Fig. 5B.3. It is interesting to note in figure 5B.3 that microwave sintering resulted in much higher sintered densities than those obtained by conventional sintering. For sample with x = 0.6, 95% of the RSD was achieved only at  $1140^{\circ}$ C sintered for just 20 mins, whereas 95% of the RSD was achieved at 1200 and  $1280^{\circ}$ C for samples with x = 0.7 and 0.8 respectively. One more interesting feature to note is, not much increase in the sintered density was observed for sample with x = 0.6 whereas, %RSDs are seen to have much more temperature dependence for other two samples. Since microwave sintering resulted in much better densifications of the samples, they were used for further studies.

# **5B. 4.** Structural characterization of sintered (BFO)<sub>(1-x)</sub> – (CTO)<sub>x</sub>

Fig. 5B.5. Shows the X-ray diffraction patterns of microwave sintered (BFO)<sub>(1-x)</sub> –  $(CTO)_x$  (x = 0.6, 0.7, 0.8) samples. To identify the crystal system and change in lattice parameters in BFO-CTO solid solution system, Rietveld refinement was carried out using Full Prof software. Rietveld refinement of the X-ray diffraction data has been performed based on the previous preliminary X-ray diffraction results and reported literature [1, 2]. All the structural models were refined with the Pseudo-Voigt peak shape function. Significantly improved goodness of fit was obtained with single-phase perovskite structure (Orthorhombic) for x = 0.6, 0.7, and 0.8 with Pbnm space group symmetry which is shown in Fig. 5B.5a-c. Good agreement between the observed and calculated X-ray diffraction profile can be seen in the figure. Rietveld refinement results have shown that an increase in CTO content from x =0.6 to 0.8 weakens the rhombohedral symmetry of BFO. Shifting of the diffraction peaks to higher angles, broadening and merging of the peaks led to the distorted perovskite structure (orthorhombic), which are in good agreement with the reported literature [1, 2]. It was observed that (104) and (110) diffraction peaks of BFO centred ~32° shifted to higher diffraction angles, broadened, and merged into one peak as shown in Fig. 5B.5d, indicating that the solid solution undergoes a structural phase transformation from rhombohedral to orthorhombic symmetry with increasing CTO content [3]. The shifting of diffraction peaks of BFO to higher angles can

be attributed to the partial substitution of lower ionic radii of  $Ca^{2+}$  (100 pm) for  $Bi^{3+}$  (103 pm), and  $Ti^{4+}$  (60.5 pm) for  $Fe^{3+}$  (64.5 pm) [4].

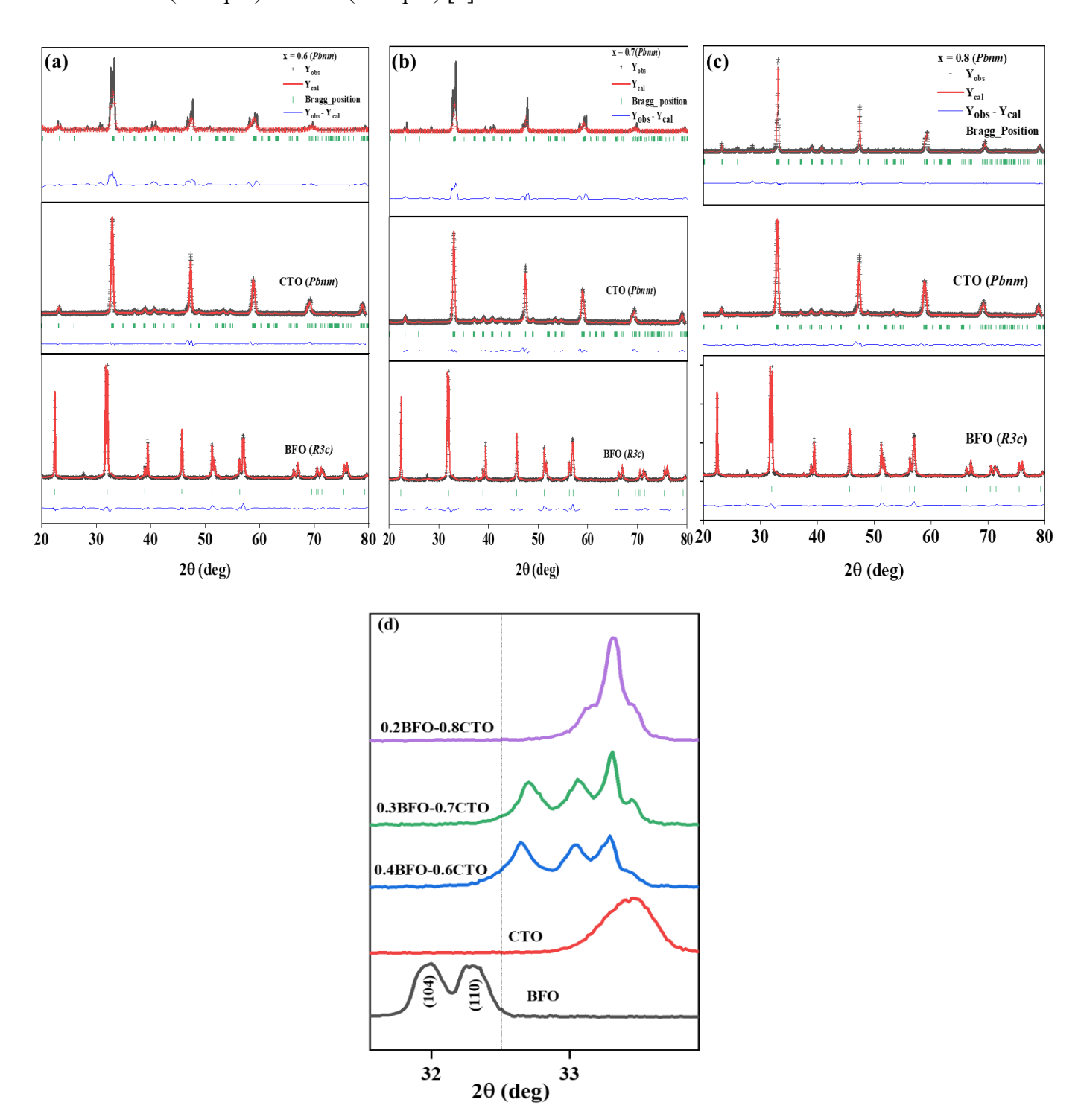


Fig 5B. 5 Rietveld refined analysis results of X-ray diffraction pattern of (BiFeO<sub>3</sub>)(1-x) – (CaTiO<sub>3</sub>)x, (a) x = 0.6, (b) x = 0.7, and (c) x = 0.8. (d) Merged and broadened XRD pattern in the vicinity of  $32^{\circ}$ 

# 5B. 5. Structural tolerance factor (t)

The structural transition was further confirmed by analysing the Goldsmith tolerance factor which is known to describe the stability of the perovskite structure. Fig. 5B.6. Represents the estimated tolerance factor 't' of  $(BFO)_{(1-x)} - (CTO)_x$  (x = 0, 0.6, 0.7, and 0.8) samples, plotted as a function of CTO content (x), and can be obtained using the following expression,

$$t = \frac{[(1-x)R_{Bi^{3+}} + xR_{Ca^{2+}} + R_{O^{2-}}]}{\sqrt{2[(1-x)R_{Fe^{3+}} + xR_{Ti^{4+}} + R_{O^{2-}}]}}$$

The tolerance factor (t) in figure 5B.6 is seen to increase with increasing CTO content of the  $(BFO)_{(1-x)} - (CTO)_x$  (x = 0, 0.6, 0.7, and 0.8) samples, indicating increasing structural symmetry and further confirming the structural phase transition of the BFO-CTO solid solutions. The obtained tolerance factor values agree with the earlier reported literature [1].

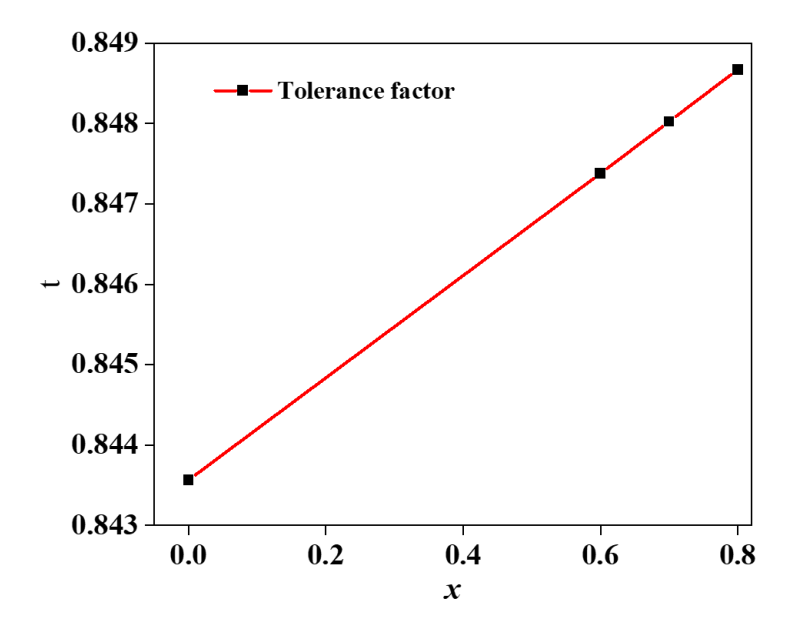


Fig 5B. 6 Tolerance factor of (BiFeO<sub>3</sub>)  $(1-x) - (CaTiO_3) x$  (x = 0, 0.6, 0.7, and 0.8) ceramics as a function of x.

#### 5B. 6. Microstructural characterization

Fig. 5B.7. shows the FESEM micrographs of microwave sintered samples of (BFO)<sub>(1-x)</sub> – (CTO)<sub>x</sub> (x = 0, 0.6, 0.7, and 0.8) ceramics. Pure BiFeO<sub>3</sub> microstructure, microwave sintered at 850°C for 20 minutes, displayed very poor densification (%RSD ~85%) with residual porosities confined mostly in the grain boundary regions. Apart from BFO grains the microstructure also consists of a mullite type (Bi<sub>2</sub>Fe<sub>4</sub>O<sub>9</sub>) secondary phase which appears as

white spots and distributed throughout the BFO matrix as shown in fig. 5B.7a. The distribution of porosities has been shown in larger area of the sample. The microstructures of the BFO ceramics, in presence of CTO, are very different. Highly dense microstructure has been observed for samples with x = 0.6, 0.7 and 0.8 as shown in fig. 5B.7(b-d). Grain size distribution of the samples are shown in the inset of figures 5B.7(a) to 5B.7(d).

Although pure BFO (x = 0) resulted in porous microstructure, the average grain size was  $\sim$ 30  $\mu$ m. But grain refinement has been observed in the BFO-CTO sintered samples. Grain size distribution revealed that the average grain size of the samples with x = 0.6 was  $\sim$ 0.9  $\mu$ m and for x = 0.8 was  $\sim$ 1.5  $\mu$ m. But the average grain size of the sample with x = 0.7 was  $\sim$ 6  $\mu$ m.

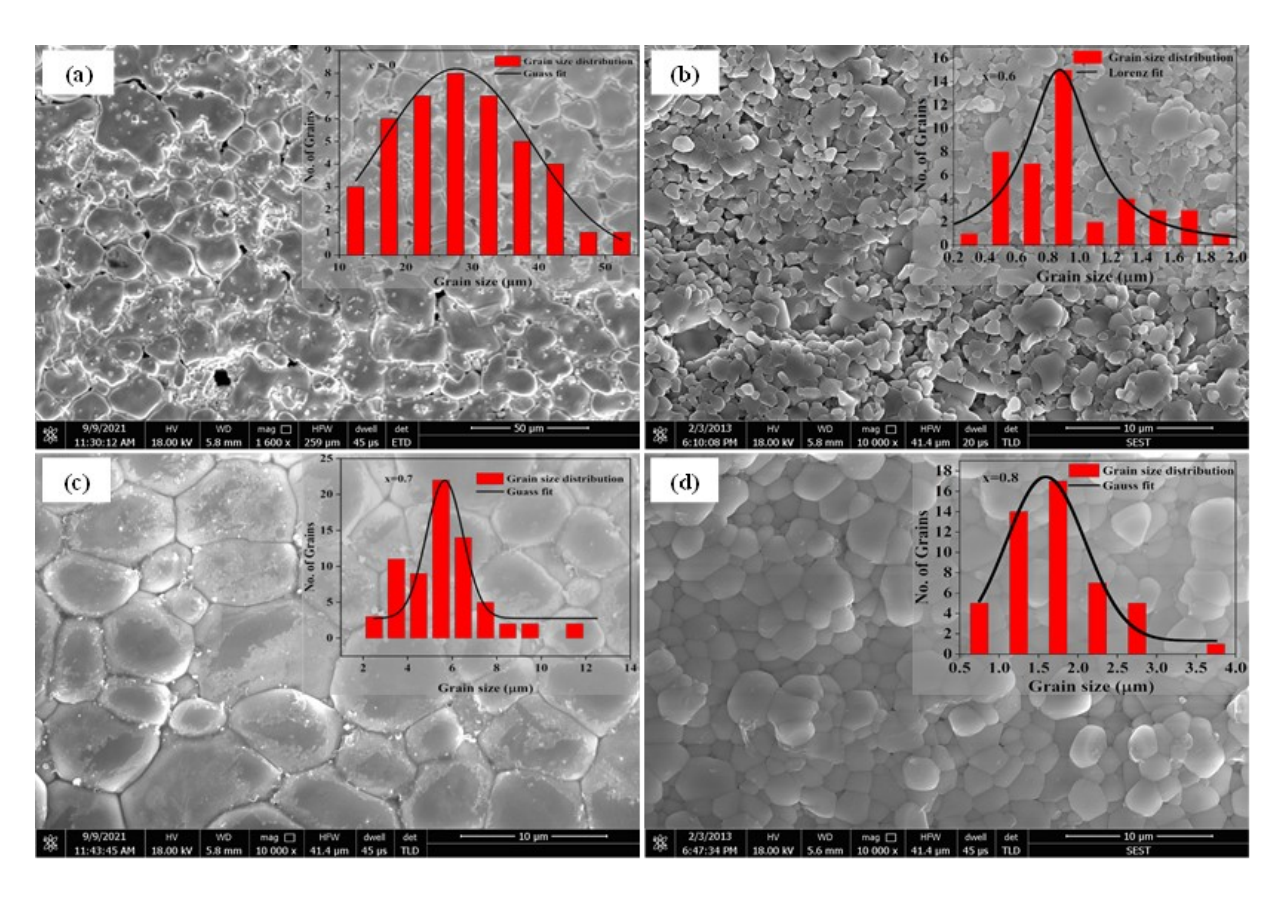


Fig 5B. 7 FESEM micrographs of  $(BiFeO_3)(1-x) - (CaTiO_3)x$  microwave sintered samples: (a) x = 0, (b) x = 0.6, (c) x = 0.7, and (d) x = 0.8. The inset shows the grain size distribution of the samples

Although occasional appearance of few larger grains in the microstructure may result from the presence of lower melting BFO in the BFO-CTO solid solution matrix, but significant enhancement in the average grain size of the sample with x = 0.7 (compared to x = 0.6 and 0.8) is not known to us at the moment.

# 5B. 7. Elemental studies

Elemental compositions were studied by energy dispersive spectroscopic (EDS) analysis of the microwave sintered samples. Although Bi is quite volatile in nature, presence of Bi along with all the other elements were observed in the EDS spectrum of the samples as shown in fig. 5B.8 (a-c) and the estimated wt.% of the elements are shown in table 5B.1.

Table 5B. 1 Elemental analysis of the sintered samples of (BiFeO<sub>3</sub>)  $(1-x) - (CaTiO_3) x$ , (x = 0.6, 0.7, and 0.8)

Element	x = 0.6 (wt%)	x = 0.7 (wt%)	x = 0.8 (wt%)
Ca	22.30	24.77	25.52
Ti	27.35	26.78	24.30
0	23.90	29.23	34.93
Bi	18.23	13.36	8.25
Fe	8.22	5.80	7.00

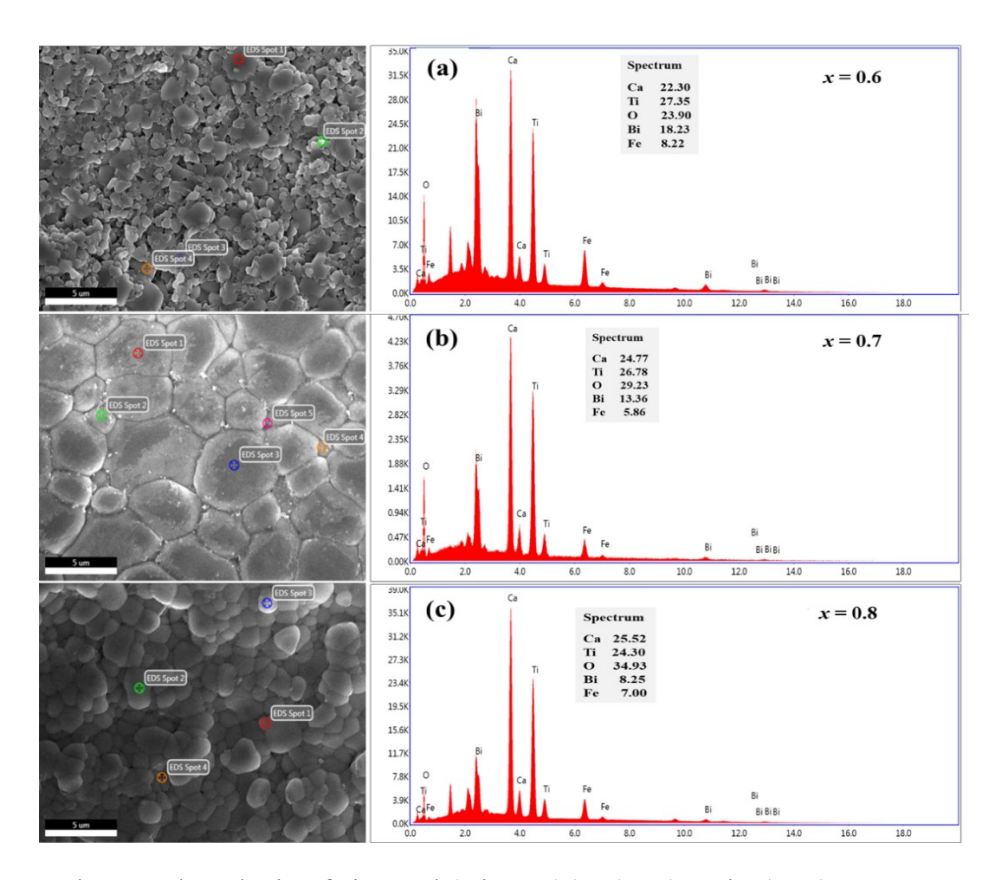


Fig 5B. 8 Elemental analysis of sintered (BiFeO<sub>3</sub>)(1-x) – (CaTiO<sub>3</sub>)x (x = 0.6, 0.7 and 0.8) ceramics

# 5B. 8. Conduction mechanisms in $(BFO)_{(1-x)} - (CTO)_x$ ceramics

Electric field dependent leakage current densities (J) of the samples (BFO)<sub>(1-x)</sub> – (CTO)<sub>x</sub> (x = 0, 0.6, 0.7, and 0.8) have been shown in fig. 5B.9. It is noted that the current densities of the bulk BFO-CTO samples were diminished by several orders of magnitude with increasing CTO content,  $1.9 \times 10^{-1}$  A.cm<sup>-2</sup> for x = 0 to  $7.4 \times 10^{-5}$  A.cm<sup>-2</sup> for x = 0.8 at an applied electric field of 1 kV.cm<sup>-1</sup>. From a careful look at the J-E curves it is seen that all the samples show ohmic behaviour at lower electric fields ( $\log_{10} J \sim S \log_{10} E$ , where the slope  $S \approx 1$ ). With increasing electrical field, the conduction mechanism probably changed to space charge limited conduction ( $\log_{10} J \sim S \log_{10} E$ , where the slope  $S \approx 2$ ) at intermediate fields for pure BFO (x =0), with charge carriers available from various sources. The Schottky or Poole-Frenkel type conduction was observed at higher fields ( $\log_{10} J \sim S \log_{10} E$ , where the slope S > 2) may be due to the highly conductive nature of BFO (x = 0) [5-7]. BFO is known as conductive ceramic due to valence fluctuations of 'Fe-ions.' i.e., Fe<sup>3+</sup> to Fe<sup>2+</sup> transition, where the oxygen vacancies act as charge carriers, which enhances the leakage current. Therefore, suppression of the valence fluctuation of 'Fe' ions might reduce the leakage current. Transition of Fe<sup>3+</sup> to Fe<sup>2+</sup> was reported in BFO based ceramics for partial substitution with analogous ions (Ti, Mn, Al, and Co) or in BFO-ABO<sub>3</sub> (such as STO and BTO) type solid solution compositions [5, 8-11]. It is anticipated that in presence of CTO partial substitution of Ti<sup>4+</sup> ions at 'Fe' sites of BFO should suppress the Fe valence fluctuations, consequently reducing the leakage current. CTO is a highly resistive material, and Ca-O bond energy is higher than Bi-O bond energy. When Ca ions substitute for Bi ions in A site, and Ti ions substitute for Fe in B site the change in valence state of Fe-ions from Fe<sup>3+</sup> to Fe<sup>2+</sup> is suppressed [12-13]. The observed reduction in the leakage current densities in the (BFO)<sub>(1-x)</sub> – (CTO)<sub>x</sub> (x = 0, 0.6, 0.7, and 0.8) solid solutions at all fields studied in this investigation is certainly due to the valence fluctuations of the Fe ions. Electric field dependent conductivity and electrical resistivity of the samples,  $(BFO)_{(1-x)}$  –  $(CTO)_x$  (x = 0, 0.6, 0.7, and 0.8) are shown in fig. 5B.10a (for conductivity) and b (for resistivity) respectively. Almost two orders decrease in the electrical conductivity or increase in the resistivity, from  $1.04 \times 10^5 \Omega$  cm (x = 0) to  $2.16 \times 10^7 \Omega$  cm (x = 0.8) have been observed with increasing CTO content of the samples. Also, the electrical properties, conductivity, or resistivity, have been found to be independent of the applied electric field studied in this investigation. The increased resistivity of the samples helps the material to withstand higher electric fields without undergoing an electrical breakdown, which is essential for higher recoverable energy density.

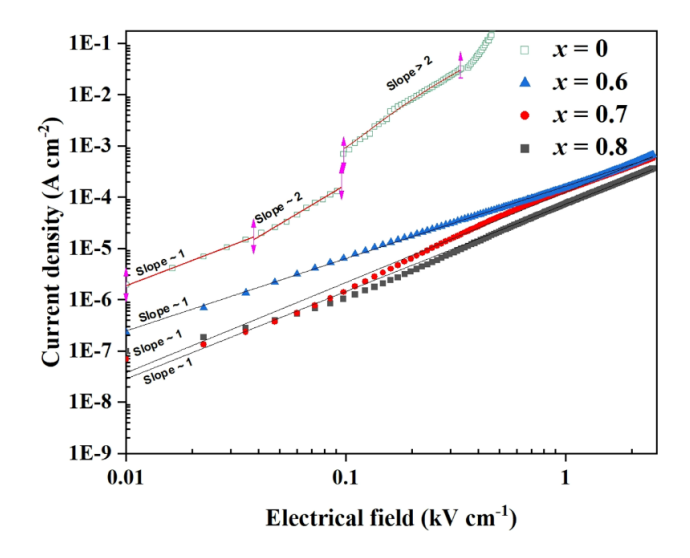


Fig 5B. 9 Leakage current density as a function of electric field at room temperature for sintered (BiFeO<sub>3</sub>)  $(1-x) - (CaTiO_3) x$  samples with x = 0, 0.6, 0.7 and 0.8

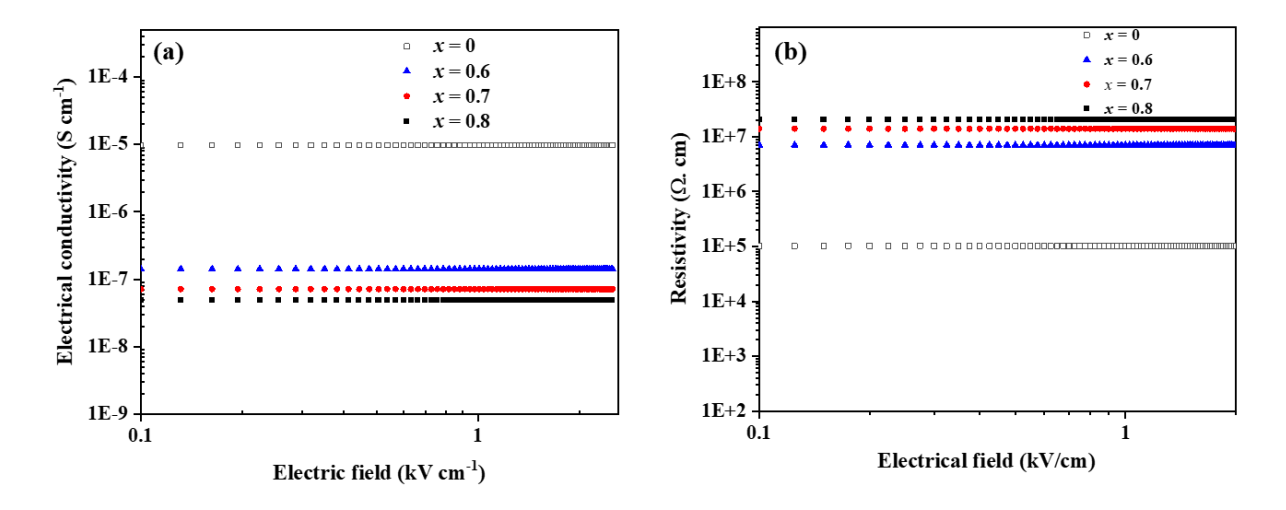


Fig 5B. 10 Variation in electrical conductivity and resistivity of  $(BiFeO_3)(1-x) - (CaTiO_3)x$  ceramics as a function of electric field at room temperature for samples with x = 0, 0.6, 0.7 and 0.8

### 5B. 9. Dielectric properties

Frequency-dependent dielectric permittivity ( $\varepsilon$ ') and loss tangent (tan  $\delta$ ) have been shown in Fig. 5B.11a-b. The permittivity and loss tangent of BFO-CTO samples showed frequency dependence. The dielectric permittivity increased with increasing CTO content (~95 for x = 0.6, ~124 for x = 0.8) at 10 MHz and decreased with increasing frequency (~186 at 1 MHz and ~124 at 10 MHz for x = 0.8). The relatively lower permittivity ~114 at 10MHz of the sample with x = 0.7, compared to x = 0.6 and 0.8, could be related to grain size effect. Loss tangent of the samples is found to reduce with increasing CTO content up to x = 0.7 and a marginal increase for x = 0.8, ~0.38 for x = 0, ~0.27 for x = 0.6, ~0.03 for x = 0.7, and ~0.06

for x = 0.8 at 10 MHz, as shown in fig. 5B.11b. Whereas the samples with x = 0, 0.7 and 0.8 showed relatively weak frequency dependence in the range studied, a sharp rise in the loss tangent with decreasing frequency has been observed for sample with x = 0.6, which could be related to its smaller grain structure. The lowest loss observed for  $x = 0.7 \sim 0.01$  at 5 MHz and higher frequencies could be attributed to grain size effect and correlates well with dielectric permittivity and microstructural data. Therefore, CTO addition in the BFO matrix offers higher  $\varepsilon$ ' and lower tan  $\delta$  which are in good agreement with the earlier reported literature [1, 14-16]. The observed  $\varepsilon$ ' values for our samples (x = 0.6-0.8) is larger than the reported  $\varepsilon$ ' values ( $\sim$ 95 for x = 0.1,  $\sim$ 110 for x = 0.15 and  $\sim$ 100 for x = 0.2) at 10 MHz as reported by Q Q Wang et al. [26] and  $\sim$ 85 at 10MHz as reported by Sreenu et al [42]. The loss tangent value of our sample with x = 0.7 is lower than the reported tan  $\delta$  values ( $\sim$ 0.19 for x = 0.1,  $\sim$ 0.16 for x = 0.15,  $\sim$ 0.17 for x = 0.2 and the lowest loss observed was  $\sim$ 0.03 for x = 0.3) at 10 MHz [26] and  $\sim$ 0.02 at 10 MHz as reported by Sreenu et al [15]. Higher  $\varepsilon$ ' will facilitate miniaturization of the components and lower tan  $\delta$  will prevent energy dissipation in the energy storage devices.

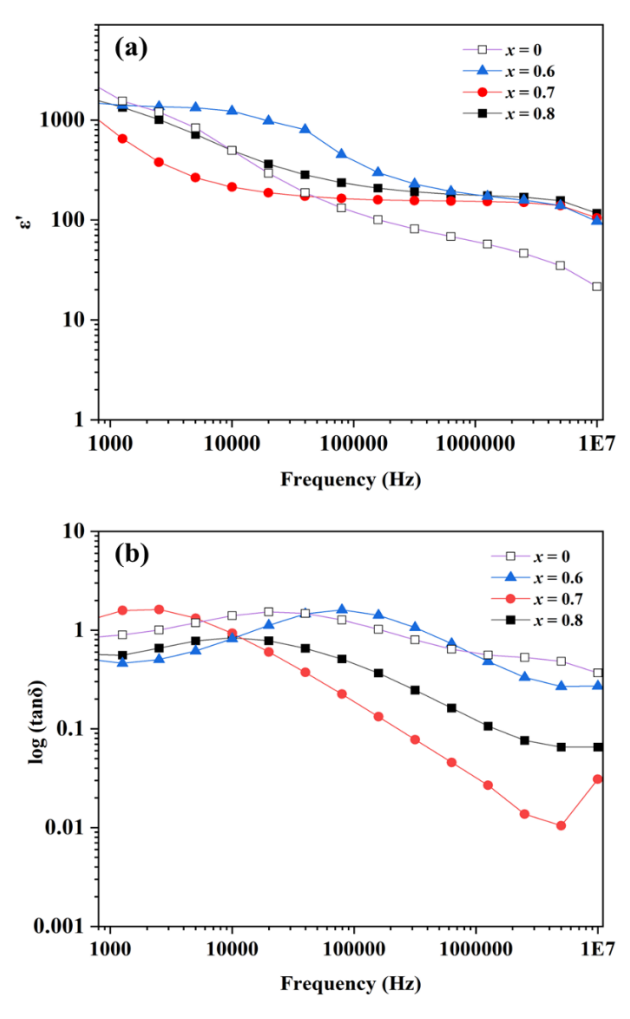


Fig 5B. 11 Room temperature frequency dependent (a) dielectric permittivity ( $\epsilon$ '), and (b) loss tangent (tan  $\delta$ ) of (BiFeO<sub>3</sub>)(1-x) – (CaTiO<sub>3</sub>)x ceramics with x = 0, 0.6, 0.7 and 0.8

# **REFERENCES**

- [1] Qing Qing Wang, Zhuo Wang, Xiao Qiang Liu, and Xiang Ming Chen, "Improved Structure Stability and Multiferroic Characteristics in CaTiO3-Modified BiFeO3 Ceramics", J. Am. Ceram. Soc., 95 [2] 670–675, DOI: 10.1111/j.1551-2916.2011.04824.x (2012)
- [2] K. S. K. R. Chandra Sekhar, M. L. V. Mahesh, T. Sreenivasu, Y. Rama Krishna, K. Chandra Mouli, and Patri Tirupathi, "Structural evolution, dielectric relaxation and modulus spectroscopic studies in Dy substituted NBT-BT ferroelectric ceramics", J Mater Sci: Mater Electron, (2021) 32:8628–8647
- [3] Qing Qing Wang, Hong Jian Zhao, and Xiang Ming Chen, "Low-temperature dielectric behavior of BiFeO3-modified CaTiO3 incipient ferroelectric ceramics", Journal of Applied Physics 111, 126101 (2012), DOI: 10.1063/1.4729080
- [4] Tatiana M. Correia, Mark McMillen, Maciej K. Rokosz, Paul M. Weaver, John M. Gregg, Giuseppe Viola, k and Markys G Cain, "A Lead-Free and High-Energy Density Ceramic for Energy Storage Applications", J. Am. Ceram. Soc., 1–4 (2013), DOI: 10.1111/jace.12508
- [5] Hao Pan, Jing Ma, Ji Ma, Qinghua Zhang, Xiaozhi Liu, Bo Guan, Lin Gu, Xin Zhang, Yu-Jun Zhang, Liangliang Li, Yang Shen, Yuan-Hua Lin & Ce-Wen Nan, "Giant energy density and high efficiency achieved in bismuth ferrite-based film capacitors via domain engineering", Nature communications, DOI: 10.1038/s41467-018-04189-6 (2018).
- [6] Chiu, F., "A review on conduction mechanisms in dielectric films", Adv. Mater. Sci. Eng. 2014, 1–18 (2014), DOI: 10.1155/2014/578168
- [7] Pabst, G. W., Martin, L. W., Chu, Y. & Ramesh, R., "Leakage mechanisms in BiFeO3 thin films", Appl. Phys. Lett. 90, 72902 (2007), DOI: 10.1063/1.2535663
- [8] Ishiwara, H., "Impurity substitution effects in BiFeO3 thin films—From a viewpoint of FeRAM applications", Curr. Appl. Phys. 12, 603–611 (2012), DOI: 10.1016/j.cap.2011.12.Wang, Y. & Nan, C., "Enhanced ferroelectricity in Ti-doped multiferroic BiFeO3 thin films", Appl. Phys. Lett. 89, 52903 (2006), DOI: 10.1063/1.2222242
- [9] Guo, Y. et al., "Critical roles of Mn-ions in enhancing the insulation, piezoelectricity and multiferroicity of BiFeO3-based lead-free high temperature ceramics", J. Mater. Chem. C. 3, 5811–5824 (2015), DOI: 10.1039/C5TC00507H
- [10] Khan, M. A., Comyn, T. P. & Bell, A. J., "Leakage mechanisms in bismuth ferrite-lead titanate thin films on Pt/Si substrates", Appl. Phys. Lett. 92, 72908 (2008), DOI: 10.1063/1.2839598

- [11] J.W. Kim, C.M. Raghavan, S.S. Kim, "Structural and electrical properties of 0.7 BiFeO3–0.3 CaTiO3 solid solution thin films deposited from solutions", J. Sol Gel Sci. Technol. 76, 693-698 (2015)
- [12] W. Cai, C.L. Fu, R.L. Gao, W.h. Jiang, X.L. Deng, G. Chen, "Photovoltaic enhancement based on improvement of ferroelectric property and band gap in Ti-doped bismuth ferrite thin films", J. Alloys Compd. 617, 240-246 (2014), https://doi.org/10.1016/j.jallcom.2014.08.011
- [13] Hongyong Liu, Yongping Pu, Xuan Shi and Qibin Yuan "Dielectric and ferroelectric properties of BiFeO3 ceramics sintered in different atmospheres", Ceramics International 39 (2013) S217– S220, DOI: 10.1016/j.ceramint.2012.10.065
- [14] Gomasu Sreenu, Mahfooz Alam, Didier Fasquelle, and Dibakar Das, "High-frequency dielectric characterization of novel lead-free ferroelectrics", (2020), DOI: 10.1007/s10854-020-04391-7
- [15] H.P. Kumar, C. Vijayakumar, C.N. George, S. Solomon, R. Jose, J.K. Thomas, J. Koshy, "Characterization and sintering of BaZrO3 nanoparticles synthesized through a single-step combustion process", J. Alloys Compd. 458, 528–531 (2008), https://doi.org/10.1016/j.jallcom.2007.04.032
- [16] A. Pashkin, S. Kamba, M. Berta, J. Petzelt, G.D.C. Csete-de- Gyo"rgyfalva, H. Zheng, H. Bagshaw, I.M. Reaney, "High-frequency dielectric properties of CaTiO3-based microwave ceramics", J. Phys. D 38, 741–748 (2005), https://doi.org/10.1088/0022-3727/38/5/012

# **CHAPTER - 5C**

# 5C Influence of CTO on Structural, Microstructural, Electrical and Dielectric Properties of BFO-based Lead-Free Ceramics Through Microwave Sintering

## 5C. 1. Structural analysis

XRD was utilized to determine the crystal structure of the sintered BFO<sub>(1-x)</sub> - CTO<sub>x</sub> (x = 0, 0.1, 0.3, 0.5 and 1) materials which are illustrated in Figure 5C.1(a-e). Rietveld refinement fitting mode was employed to identify the samples' weighted phase fraction, lattice parameters and volume variations for different stoichiometric compositions (e.g., x = 0, 0.1, 0.3, 0.5 and 1). In this analysis, the Pseudo-Voigt profile function is utilised to accurately describe peak shape, as it considers the broadening due to instrumental effects (Gaussian) and intrinsic broadening caused by crystalline properties (Lorentzian). Figure 5C.1a shows the Rietveld refined characteristic diffraction pattern of pure BFO (x = 0), revealing that the pure BFO exhibits a rhombohedral (R) crystal structure with R3c space group symmetry. Figure 5C.1b displays the partial substitution of CTO into BFO matrix and exhibits orthorhombic (O) (85% weighted phase fraction corresponding to Bi<sub>0.6</sub>Ca<sub>0.4</sub>Fe<sub>0.6</sub>Ti<sub>0.4</sub>O<sub>3</sub>) + R (15% corresponding to BFO) crystal structure with Pbnm + R3c symmetry for 0.1 of x. Figure 5C.1(c-e) was displayed 'O' crystal structure for x = 0.3 (Fig 5C.1c), x = 0.5 (Fig 5C.1d) and x = 1.0 (Fig 5C.1e). These results are in accordance with the previous reports [1, 2]. The observed and calculated intensities are very well fitted and the corresponding lattice parameters, goodness of the fit, weighted phase fraction and volume variations yielded by Rietveld refinement are represented in Table 5C.1.

Figure 5C.1f shows enlarged XRD peaks at the concentration of 32°, it was noticed that the diffraction peaks (104) and (110) shifted towards the larger angles with merging, splitting, and broadening, resembling the occurrence of phase transition from 'R' to 'O' with increasing CTO concentration and the reduction in the volume from 237.29 (ų) (x = 0.1) to 231.23 (ų) (x = 0.5) (ref. Table 5C.1) which is attributed to the partial substitution of lower ionic radii of Ca²+ (100 pm), Ti⁴+ (60.5 pm) for A site (Bi³+, 103 pm) and B site (Fe³+, 64.5 pm) respectively.

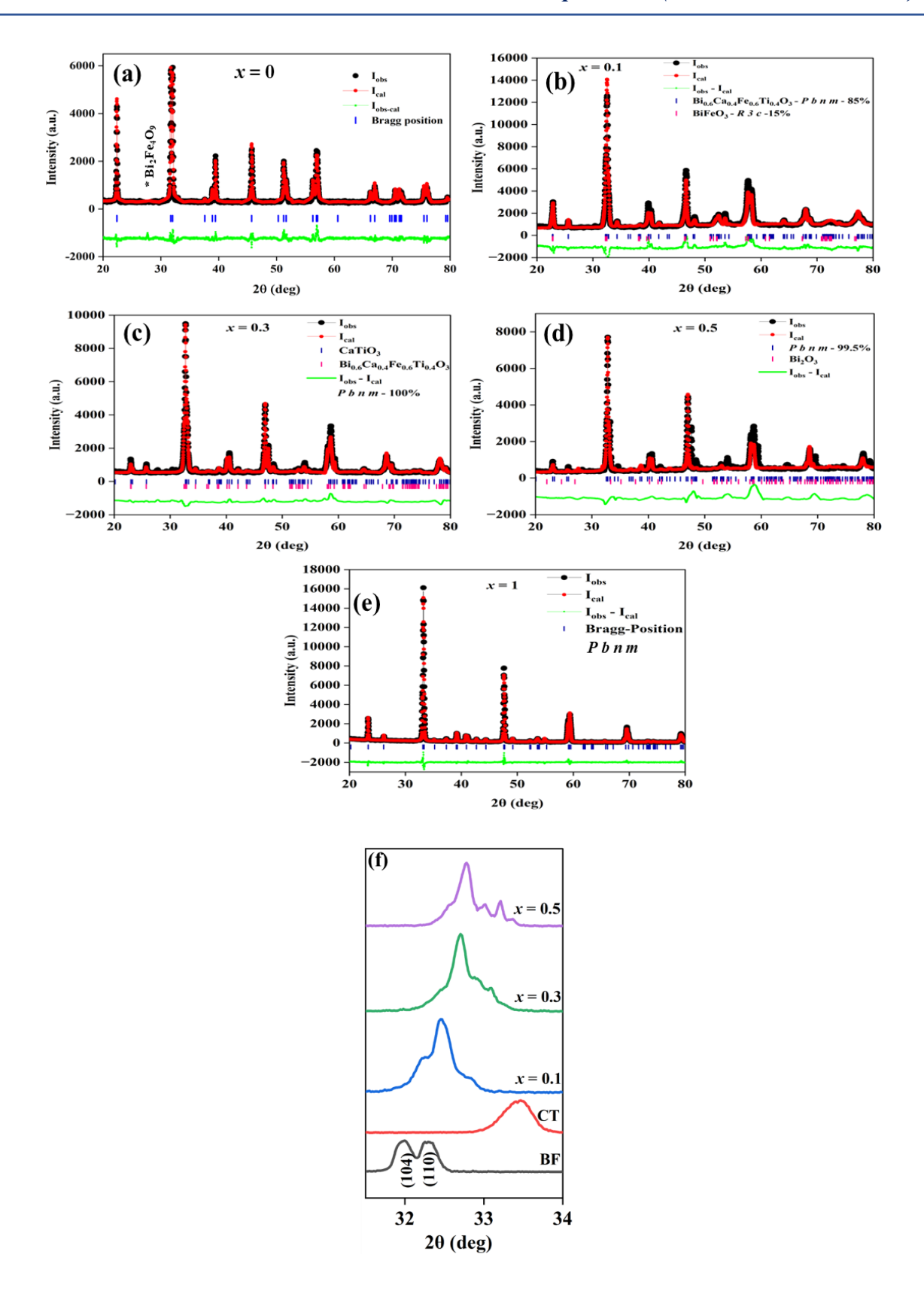


Fig 5C. 1 The outcomes of Rietveld refinement analysis of the X-ray diffraction pattern of  $(BFO)_{(1-x)} - (CTO)_x$ , (a) x = 0, (b) x = 0.1, (c) x = 0.3, (d) x = 0.5, and (e) x = 1 (f) Enlarged XRD pattern in the vicinity of  $32^\circ$ 

Table 5C. 1 Structural parameters of (1-x)BFO - xCTO yielded by the Rietveld refinement of the XRD results.

CT concentration (x)	0.1	0.3	0.5	1
Orthorhombic Phase Fraction (%)	85	100	99.5	100
a(Å)	5.556302	5.506796	5.512434	5.432196
b(Å)	7.811051	7.727080	7.754039	7.644456
c(Å)	5.467569	5.438356	5.434211	5.386050
$V(Å^3)$	237.29560	232.45310	231.23540	223.66210
$\chi^2$	4.00	1.31	2.69	1.66

# 5C.1.1 Graphical representation of BFO-CTO samples

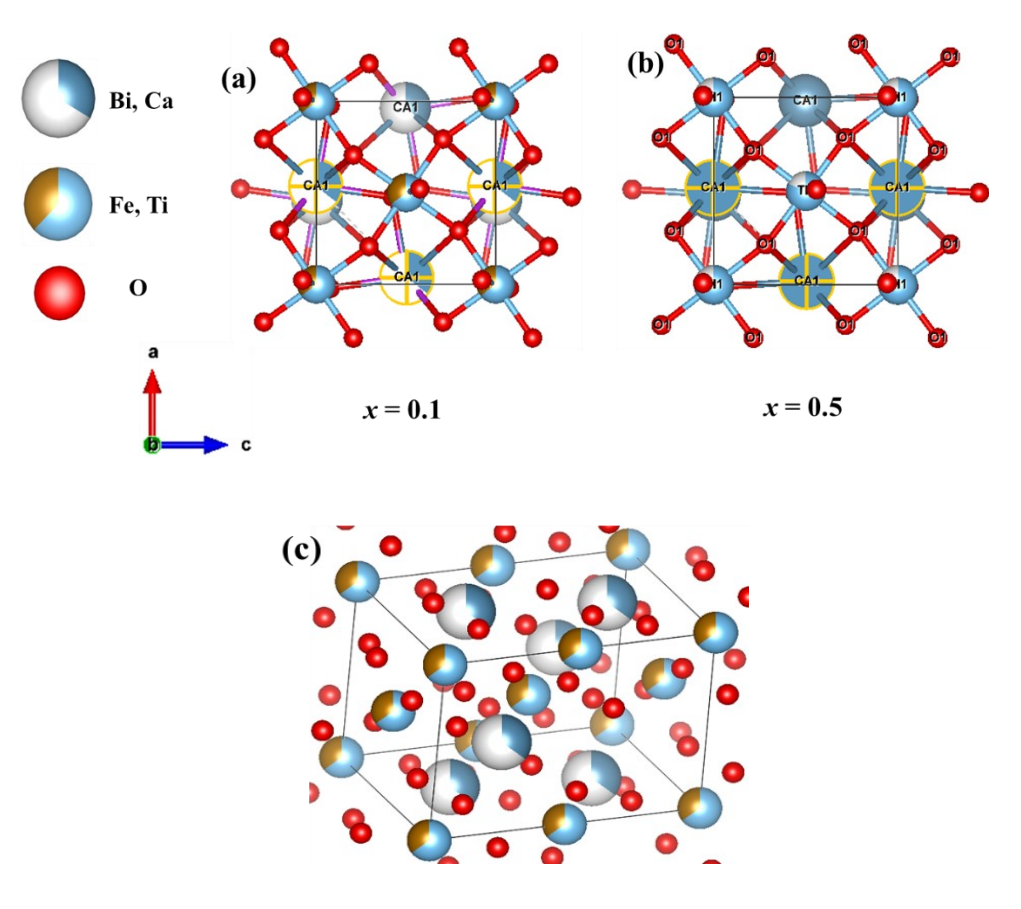


Fig 5C. 2 Schematic visualization of  $(BFO)_{(1-x)} - (CTO)_x$  ceramics for (a) x = 0.1, (b) 0.5, and (c) distorted perovskite structure.

Figure 5C.2 illustrates the schematic of the crystalline structure of the BFO-CTO representative samples for x = 0.1 and x = 0.5 (ref. Figures 5C.2a, 5C.2b). VESTA tool was utilised to measure the angles between the atoms and visualization of Bi, Ca, Fe, Ti, and O positions using different colours. The measured angles for different compositions (e.g., x = 0, 0.1, 0.3, 0.5 and 1.0) are illustrated in Table 5C.2. The deviation in angles (e.g., 54.32° for x = 0 and 56.31° for x = 0.1) between the atoms is ascribed to the partial substitution of CTO into the BFO matrix (Ca<sup>2+</sup> (100 pm for A site (Bi<sup>3+</sup>, 103 pm) and Ti<sup>4+</sup> (60.5 pm) for B site (Fe<sup>3+</sup>, 64.5 pm)) due to which a distorted perovskite structure is attained (ref. Figure 5C.2c).

Composition	Bi1Fe1O1	Bi1Fe1Fe1	Bi1Bi1Bi1	CalTi1O1	Ca1Ti1Ti1	CalCalCal
BFO	54.32	41.03	89.41	-	-	-
0.9BFO-0.1CTO	56.31	52.85	85.45	56.31	52.85	85.45
0.7BFO-0.3CTO	52.64	52.35	84.90	52.64	52.35	84.90
0.5BFO-0.5CTO	53.76	55.82	89.21	53.76	55.82	89.21
СТО	-	-	-	57.06	56.73	93.24

Table 5C. 2 Angles between the atoms

# 5C. 2. Microstructural characterization

The surface morphology of as-sintered (BFO)<sub>(1-x)</sub> - (CTO)<sub>x</sub> ceramics for x = 0, 0.1, 0.3, 0.5, and 1 is shown in Figure 5C.3 along with the grain size distribution plots illustrated in the inset of the microstructures. It was observed that all the samples show irregular grain shapes. A significant number of white spots are visible in the surface morphology of the pure BFO (x = 0). These white spots are mostly located near the grain boundaries, and they most likely represent the existence of a secondary phase of Bi<sub>2</sub>Fe<sub>4</sub>O<sub>9</sub>. Along with white spots, FESEM image of the pure BFO indicates a high level of porosity leading to the lower densification of the sintered solid matrix. The grain size distribution of the microstructure (x = 0) revealed that the average grain size (AGS) was ~ 27 µm (ref. Fig 5C.3a). It was identified that the porosity was reduced with increasing CTO content and the dense microstructures were seen for  $x \ge 0.3$ . The AGS was decreased with increasing CTO content i.e., ~1.25 µm for x = 0.1 and ~1.1 µm for x = 0.5 (Fig 5C.3(b, d)).

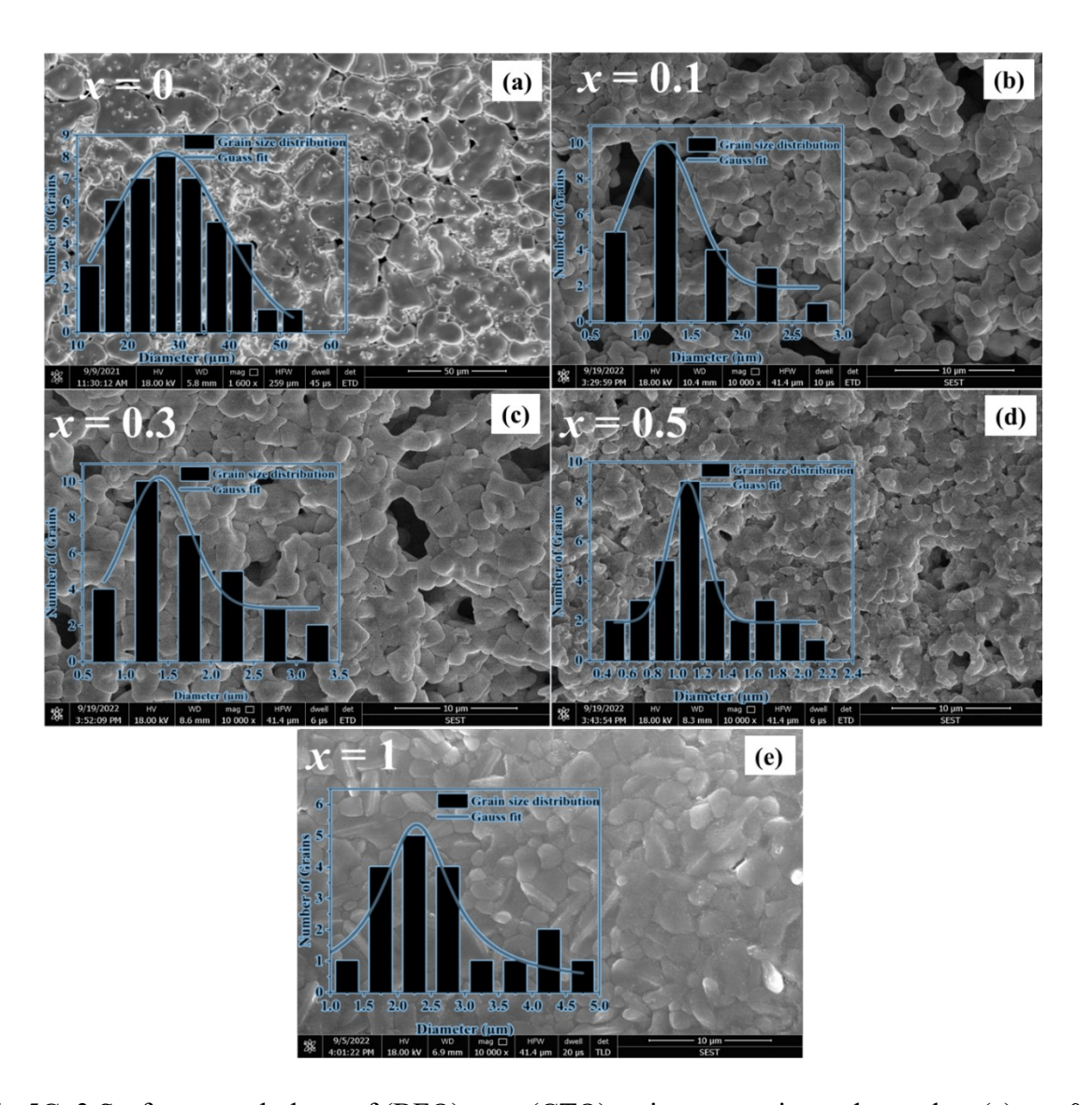


Fig 5C. 3 Surface morphology of  $(BFO)_{(1-x)} - (CTO)_x$  microwave sintered samples: (a) x = 0, (b) x = 0.1, (c) x = 0.3, (d) x = 0.5, and (e) x = 1. The inset graphs show the grain size distribution of the samples.

# 5C. 3. Electrical properties of BFO-CTO ceramics

Electric field dependence of electrical resistivity ( $\rho$ ) and conductivity ( $\sigma$ ) of (BFO)<sub>(1-x)</sub> - (CTO)<sub>x</sub> ceramics (for x = 0, 0.1, 0.3, 0.5, and 1.0) are depicted in Figures 5C.4a and 5C.4b. All electrical measurements were carried out at room temperature (T = 25 °C). A significant drop in the  $\rho$  was observed for x = 0 at an applied electric field of 0.5 kV cm<sup>-1</sup>. There is no significant variation of ( $\rho$ ) or ( $\sigma$ ) over the entire range of the applied electric field (~0.1 kV cm<sup>-1</sup> to ~0.5 kV cm<sup>-1</sup>) for  $x \ge 0.1$ . However, a significant increase in the ( $\rho$ ) was observed as we increase the CTO concentration, with the value increased by two orders of magnitude *i.e.*, from  $2.21 \times 10^3 \Omega$  cm (x = 0) to  $8.80 \times 10^5 \Omega$  cm (x = 0.5). The increased resistivity is ascribed to the incorporation of CTO (x = 1.0 shows strong electrical resistivity of nearly  $4.30 \times 10^9 \Omega$  cm at

an electric field of ~0.5 kV cm<sup>-1</sup>) into the BFO matrix. Moreover, it has been determined that the electrical properties, either ( $\rho$ ) or ( $\sigma$ ), remain unaffected by the applied electric field of 0.5 kV cm<sup>-1</sup> at this point of investigation. The enhanced ( $\rho$ ) exhibited by the samples enables the material to withstand higher electric fields without causing electrical breakdown, a crucial characteristic for achieving lower losses and higher electrostatic energy storage densities.

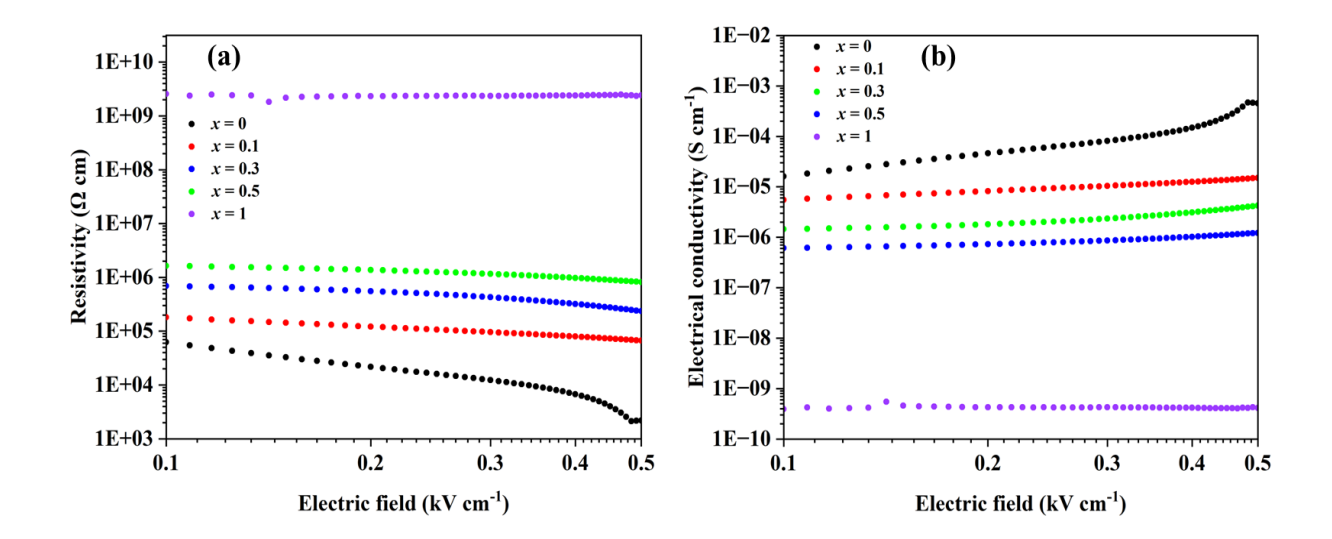


Fig 5C. 4 Electrical resistivity and conductivity of  $(BFO)_{(1-x)} - (CTO)_x$  (x = 0, 0.1, 0.3, 0.5, and x = 1) ceramics as a function of the electric field at room temperature. (a) Resistivity and (b) Electrical conductivity.

Figure 5C.5 shows the leakage current density (J) as a function of the electric field (E) for  $0 \le x \le 1$  at an electric field of 2 kV cm<sup>-1</sup>. Line fitting mode was employed to fit the obtained ( $\log_{10} J$ ) vs ( $\log_{10} E$ ) results. The (E) range is divided into three segments, and the conduction mechanisms are studied based on the slope of the fitted line. Segment (I) represents the ohmic conduction behaviour ( $\log_{10} J \sim S \log_{10} E$ , slope (S)  $\sim 1$ ) at lower E, segment (II) represents the space charge limited conduction (SCLC) behaviour ( $S \sim 2$ ) in the intermediate range of E, and segment (III) displayed the Poole-Frenkel conduction mechanism (S > 2) at higher E (for all the BFO-CTO composition except pure CTO only). The conductivity behaviour of the BFO-CTO solid solution can be ascribed to the higher conducting nature of BFO material [3-5].

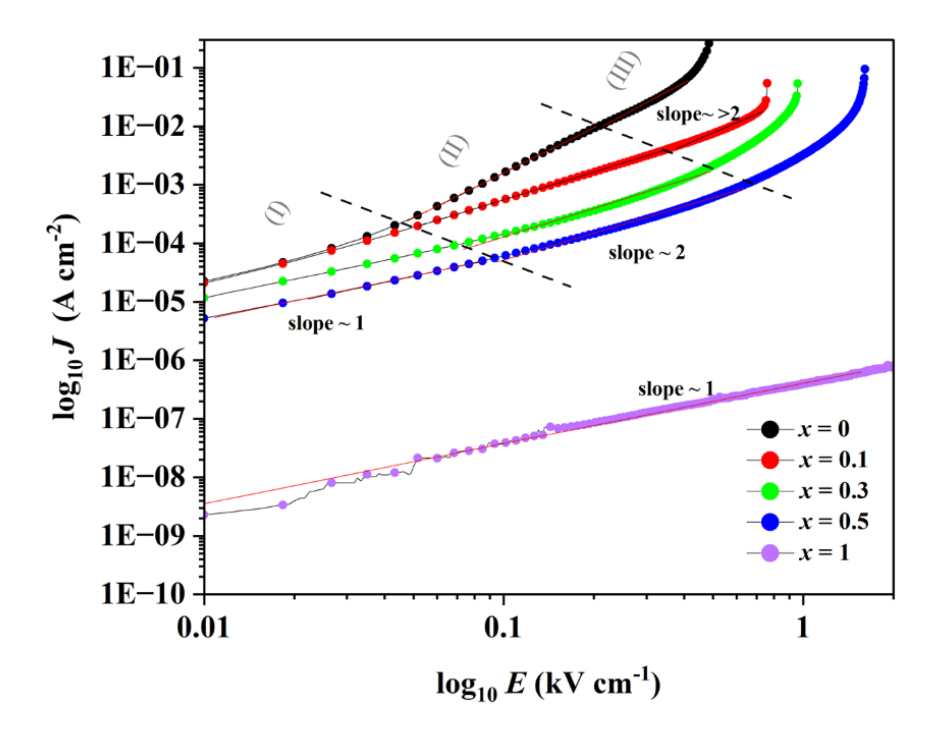


Fig 5C. 5 The variation of leakage current density with respect to the applied electric field at room temperature of microwave sintered (BFO)(1-x) – (CTO)x (x = 0, 0.1, 0.3, 0.5, and x = 1) samples.

The higher conducting nature of BFO is owing to the volatile nature of Bi at higher sintering temperature conditions and Fe fluctuations [6, 7] which leads to the formation of oxygen vacancies according to the following expression:

$$2Fe_{Fe} + O_O \longrightarrow 2Fe_{Fe}' + V\ddot{o} + \frac{1}{2}O_2$$

As CTO (x = 1.0) possesses strong resistivity, an ohmic conduction mechanism was observed throughout the applied electric field range with  $S \sim 1$ . The J is reduced by nearly two orders of magnitude from  $\sim 2.60 \times 10^{-1}$  A cm<sup>-2</sup> (x = 0) to  $\sim 2.50 \times 10^{-3}$  A cm<sup>-2</sup> (x = 0.5) at an electric field of 1 kV cm<sup>-1</sup>. The reduced J is attributed to the partial substitution of CTO ( $J \sim 4.04 \times 10^{-7}$  A cm<sup>-2</sup> at an electric field of 1 kV cm<sup>-1</sup>) into the BFO matrix (Ca<sup>2+</sup>, Ti<sup>4+</sup> into A, B sites of Bi<sup>3+</sup> and Fe<sup>3+</sup> respectively) which stabilizes the valance states Fe leading to the suppression of the formation of oxygen vacancies as reported in the previous investigations. [6, 8, 9]

# 5C. 4. Dielectric properties

# **5C.4.1** Dielectric properties at room temperature

Frequency-dependence dielectric constant  $(\varepsilon_r)$  and loss tangent  $(\tan \delta)$  are shown in Figures 5C.6a and 5C.6b. A strong frequency dependence was observed for  $\varepsilon_r$  and  $\tan \delta$  at lower frequencies up to 100 kHz. At lower frequencies up to 10 kHz, the dielectric constant sharply drops from  $\sim 1600$  (at 1 kHz, for x = 0) to  $\sim 497$ , and subsequently gradually decreases to  $\sim 60$ (at 1 MHz, for x = 0). The higher dielectric constant at lower frequencies is connected to the Maxwell-Wagner (MW) phenomenon. The Maxwell-Wagner effect is characterized by the movement and accumulation of electrical charges that significantly impact the dielectric properties of the materials. It is important to note that this type of MW effect is considered as an extrinsic effect rather than an intrinsic property of the material itself. This effect arises from imperfections like grain boundaries, porosities, voids, and incomplete electrode contact, where charges gather and generate space-charge effects. There is a weak frequency dependence for all the samples between 1 MHz to 10 MHz. Table 5C.3 represents the dielectric properties (both  $\varepsilon_r$  and  $\tan \delta$ ) of (BFO) (1-x) - (CTO)x,  $0 \le x \ge 1$ . The measurements revealed that the  $\varepsilon_r$  increased with increasing CTO content e.g.,  $\sim 24$  for x = 0.1 and  $\sim 51$  for x = 0.5 at a frequency of 10 MHz (ref. Table 5C.3). The  $\tan\delta$  is reduced by increasing CTO concentration e.g.,  $\sim 1.39$  (at 10 kHz, x = 0) to  $\sim 0.35$  (at 10 kHz, x = 0.5) and  $\sim 0.37$  (at 10 MHz, x = 0) to 0.17 (at 10 MHz, x = 0.5) (ref. Table 5C.3).

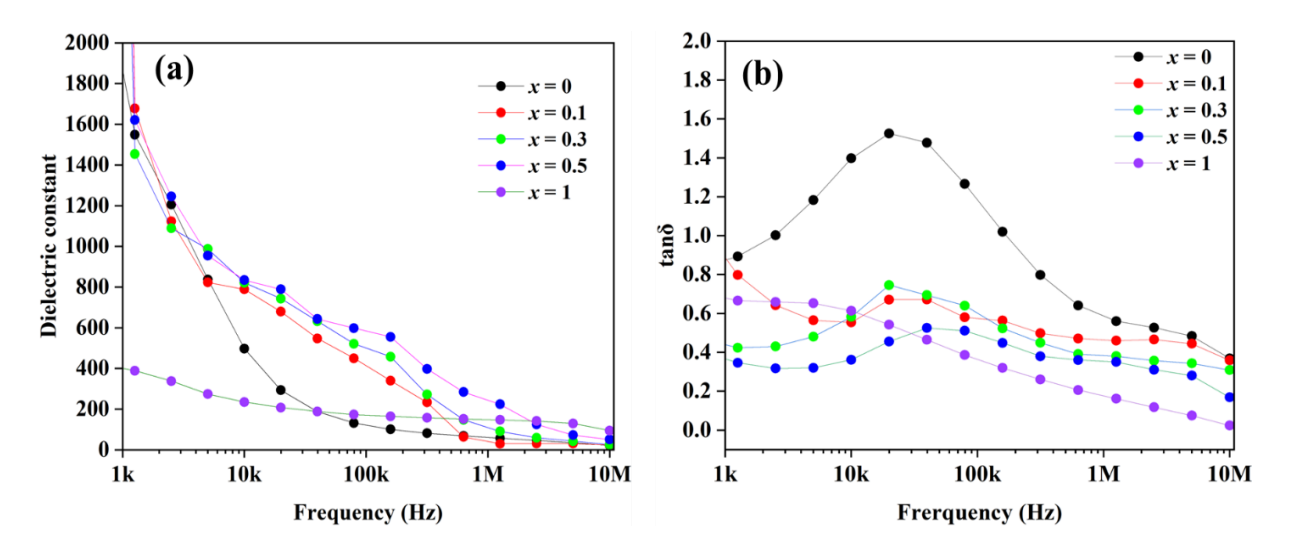


Fig 5C. 6 Frequency-dependent (a) dielectric constant, and (b) loss tangent ( $\tan \delta$ ) of (BFO)(1-x) – (CTO)x (x = 0, 0.1, 0.3, 0.5, and x = 1) ceramics.

The increased  $\varepsilon_r$  and reduced  $\tan\delta$  with increasing CTO concentration are ascribed to the ultrahigh dielectric strength (4.2 MV cm<sup>-1</sup>) of the CTO ceramic material [10]. The highest  $\tan\delta \sim 1.56$  (for x=0) was noted at a frequency of 20 kHz because of the high leakage current density (J) of the pure BFO sample.

Table 5C. 3 Frequency-dependent dielectric properties of the sintered (BFO)(1-x) – (CTO)x samples for x = 0, 0.1, 0.3, 0.5, and 1

	x = 0	x = 0.1	x = 0.3	x = 0.5	x = 1
ε' (10kHz)	497	783	816	835	237
ε' (10MHz)	21	24	26	51	95
$ an\delta (10  ext{kHz})$	1.39	0.54	0.57	0.35	0.61
$\tan\delta$ (10MHz)	0.37	0.35	0.30	0.17	0.02

# **5C.4.2** Dielectric properties as function of temperature

Dielectric constant ( $\varepsilon_r$ ) plotted against temperature in the frequency range of 20 kHz  $\leq$   $f \leq 10$  MHz as displayed in Figure 5C.7(a-c). It is noted that the  $\varepsilon_r$  declined with increasing frequency is the primary reflection of the transition from ferroelectric (FE) to relaxor-ferroelectric (RFE) behaviour [11, 12]. Double and triple dielectric anomalies were seen for x = 0.1 at 225 °C, 275 °C, and 285 °C also at 205 °C and 245 °C for x = 0.3, the anomalies that have been noticed could be for two reasons; the heterogeneous distribution of the electrical/core-shell microstructure and the response of the grain boundaries within the sample (BFO-based). This leads to the accumulation of the electrical field in certain microstructure regions. Peak broadening was observed with increasing CTO concentration.

# 5C.4.3 Relaxor nature behaviour through Curie-Weiss law

Curie-Weiss law is employed to calculate the degree of diffusivity ( $\gamma$ ), the equation can be expressed as;

$$\frac{1}{\varepsilon_r} - \frac{1}{\varepsilon_m} = \frac{(T - Tm)^{\gamma}}{C}$$
; C - constant

 $\gamma$  range  $1 \le \gamma \le 2$ , where  $\gamma = 1$  indicates normal FEs and 2 indicates ideal RFEs [13].  $\gamma$  values are computed using  $\ln\left(\frac{1}{\varepsilon_r} - \frac{1}{\varepsilon_m}\right)$  vs  $\ln\left(T - T_m\right)$  functions as shown in the inset of Figures 5C.7a,

5C.7b, and 7c.  $\gamma = 1.20$ , 1.21, and 1.61 were estimated using linear fit of the inset graphs for x = 0.1, 0.3, and 0.5 respectively. Looking at the increasing trend of the  $\gamma$  values (by increasing the x) it is anticipated that the RFE nature could be improved for  $x \ge 0.5$ .

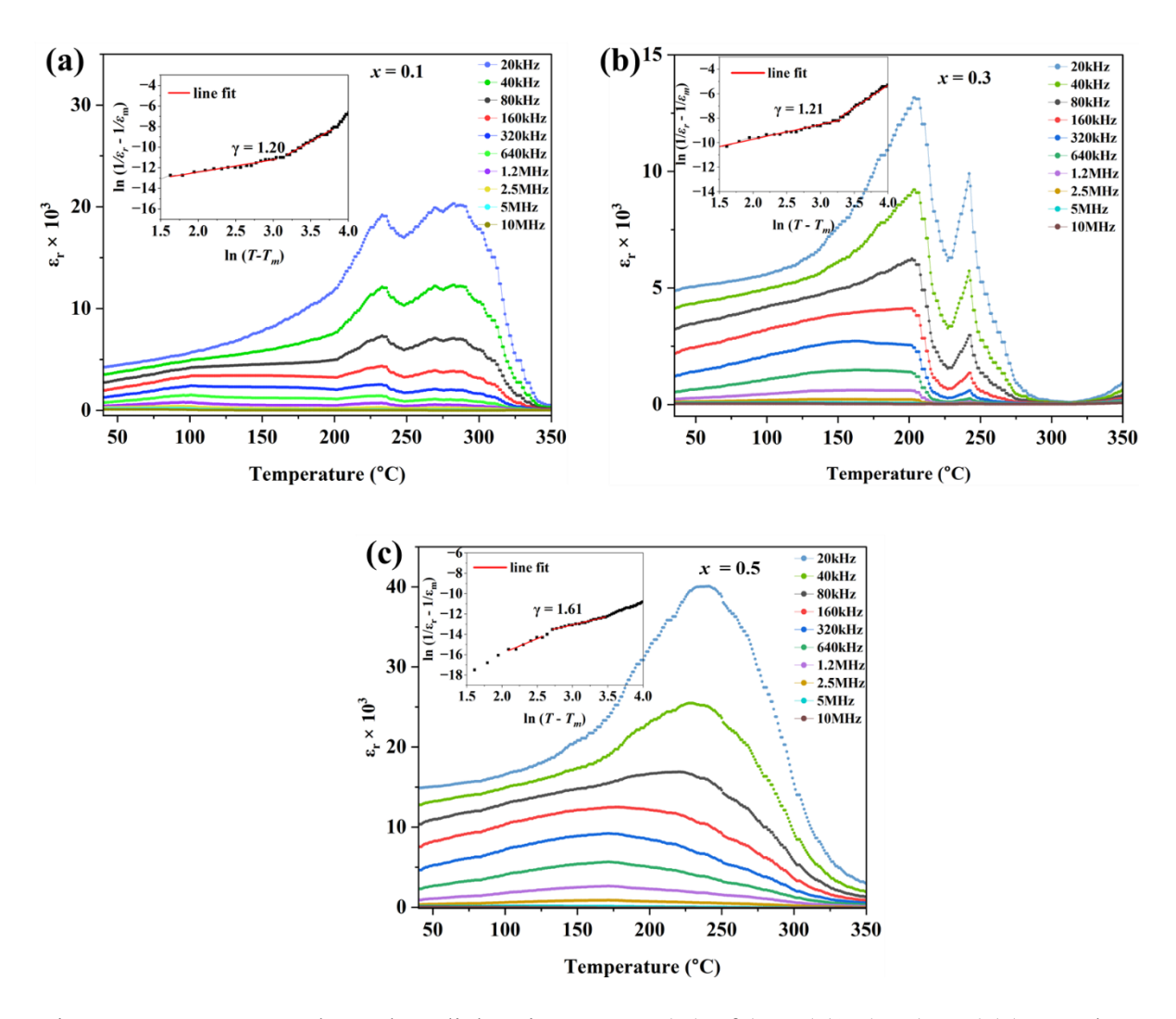


Fig 5C. 7Temperature-dependent dielectric constant ( $\epsilon r$ ) of (BFO)(1-x) – (CTO)(x) samples measured at 20 kHz – 10 MHz and Curie-Weiss law fitting as shown in the inset of figures (a) x = 0.1, (b) x = 0.3, and (c) x = 0.5

# **REFERENCES**

- [1] Q. Qing Wang, Z. Wang, X. Qiang Liu, X. Ming Chen, Improved structure stability and multiferroic characteristics in CaTiO<sub>3</sub>-modified BiFeO<sub>3</sub> ceramics. J. Am. Ceram. Soc. 95(2), 670–675 (2012). https://doi.org/10.1111/j.1551-2916. 2011.04824.x
- [2] Gomasu Sreenu, S. Saha, R.N. Bhowmik et al., Investigation of structural, electrical, and dielectric properties of lead-free (BiFeO3)(1-x) (CaTiO3)x ceramics. J. Mater. Sci: Mater. Electron. 33, 24959–24971 (2022). https://doi.org/10.1007/s10854-022-09205-6
- [3] H. Pan, J. Ma, Ji. Ma, Q. Zhang, X. Liu, Bo. Guan, Gu. Lin, X. Zhang, Y.-J. Zhang, L. Li, Y. Shen, Y.-H. Lin, C.-W. Nan, Giant energy density and high efficiency achieved in bismuth ferrite-based film capacitors via domain engineering. Nat. Commun. (2018). https://doi.org/10.1038/s41467-018-04189-6
- [4] F. Chiu, A review on conduction mechanisms in dielectric films. Adv. Mater. Sci. Eng. 2014, 1–18 (2014). https://doi. org/10.1155/2014/578168
- [5] G.W. Pabst, L.W. Martin, Y. Chu, R. Ramesh, Leakage mechanisms in BiFeO3 thin films. Appl. Phys. Lett. 90, 72902 (2007). https://doi.org/10.1063/1.2535663
- [6] Ishiwara, H. Impurity substitution effects in BiFeO3 thin films. From a viewpoint of FeRAM applications. Curr. Appl. Phys. 12, 603–611 (2012).
- [7] D. Wang, Z. Fan, D. Zhou, A. Khesro, S. Murakami, A. Feteira, Q. Zhao, X. Tan, I.M. Reaney, Bismuth ferrite-based lead-free ceramics and multilayers with high recoverable energy density, J. Mater. Chem. A 6 (2018) 4133–4144.
- [8] Guo, Y. et al. Critical roles of Mn-ions in enhancing the insulation, piezoelectricity and multiferroicity of BiFeO3-based lead-free high-temperature ceramics. J. Mater. Chem. C. 3, 5811–5824 (2015).
- [9] H. Pan, J. Ma, Ji. Ma, Q. Zhang, X. Liu, Bo. Guan, Gu. Lin, X. Zhang, Y.-J. Zhang, et. al., Giant energy density and high efficiency achieved in bismuth ferrite-based film capacitors via domain engineering. Nat. Commun. (2018) https://doi.org/10.1038/s41467-018-04189-6 (67) Khan, M. A., Comyn, T. P. & Bell, A. J. Leakage mechanisms in bismuth ferrite-lead titanate thin films on Pt/Si substrates. Appl. Phys. Lett. 92, 72908 (2008).
- [10] Haoguang Yang, et.al., Enhanced breakdown strength and energy storage density in a new BiFeO3-based ternary lead-free relaxor ferroelectric ceramic, Journal of the European Ceramic Society Volume 39, Issue 8, July 2019, Pages 2673-2679, https://doi.org/10.1016/j.jeurceramsoc.2019.03.001

- [11] Hao Pan, Yi Zeng, Yang Shen, Yuan-Hua Lin, Jing Ma, Liangliang Li and Ce-Wen Nan, BiFeO3–SrTiO3 thin film as a new lead-free relaxor-ferroelectric capacitor with ultrahigh energy storage performance, Journal of Materials Chemistry, A 5(12):5920—5926, April 2017, https://doi.org/10.1039/C7TA00665A
- [12] Rhys Montecillo, et. al., Optimized electric-energy storage in BiFeO3–BaTiO3 ceramics via tailoring microstructure and nanocluster, Journal of the European Ceramic Society. 43, 5, 1941-1951, (2023). https://doi.org/10.1016/j.jeurceramsoc.2022.12.064
- [13] Z. Shen, X. Wang, B. Luo, et.al., BaTiO3–BiYbO3 perovskite materials for energy storage applications, J. Mater. Chem. A, 2015, 3, 18146–18153, https://doi.org/10.1039/C5TA03614C

# **CHAPTER - 5D**

# 5D Study of High-Energy Density in Lead-Free BiFeO<sub>3</sub>-CaTiO<sub>3</sub> Relaxor-Ferroelectric Ceramics for High-Temperature Energy Storage Applications

# 5D. 1. Structural analysis

The crystallographic structures of the sintered samples of (1-x) BFO-xCTO (x = 0, 0.6, 0.7, 0.8, and 1) were identified using X-ray diffraction (XRD). The Rietveld fitting mode was employed using the X'Pert Highscore Plus software tool to classify the crystal structure and to identify the change in volume and lattice parameters. The data was refined using the Pseudo-Voigt profile function for all the structural models.

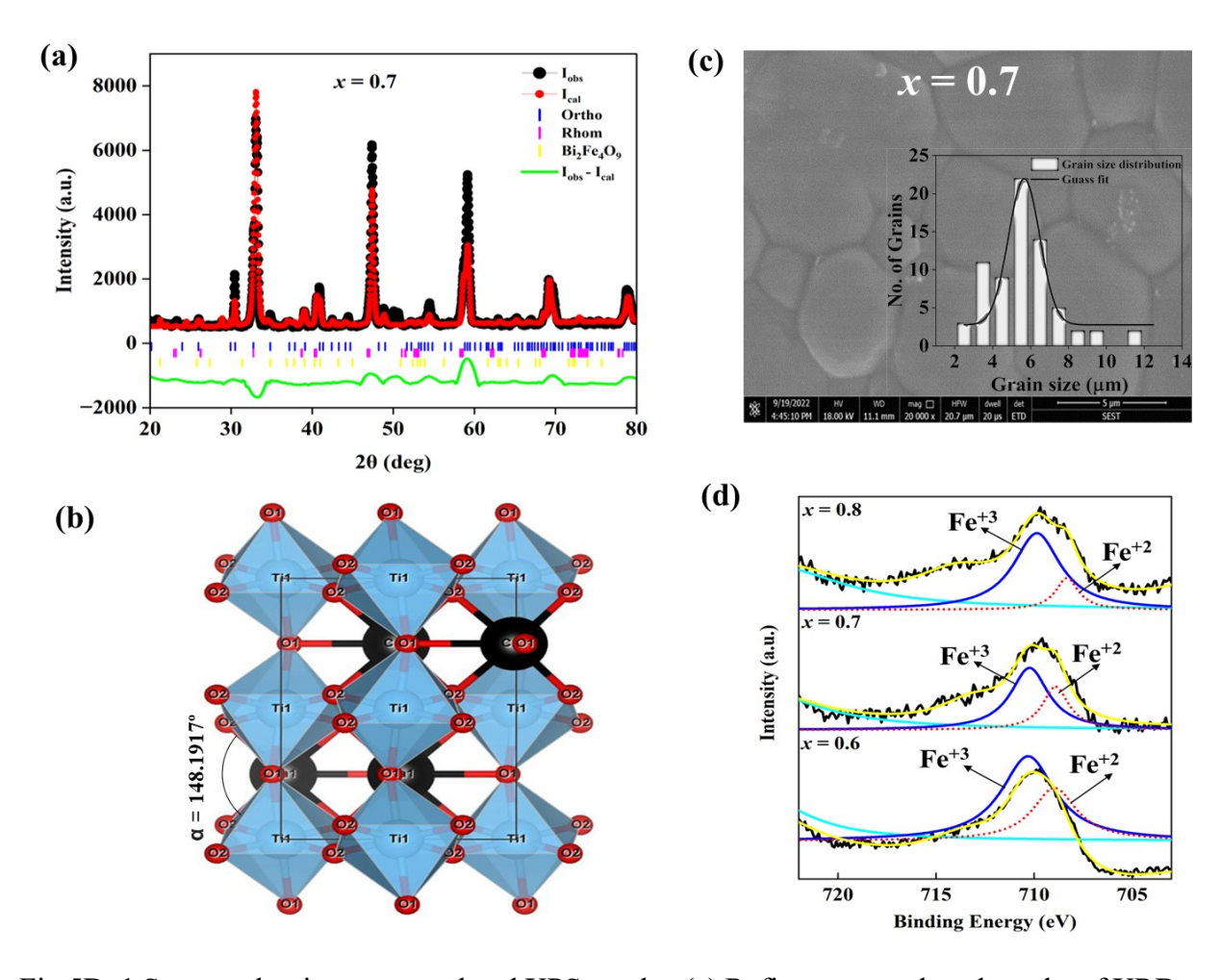


Fig 5D. 1 Structural, microstructural and XPS results. (a) Refinement analyzed results of XRD for 0.7 of x. (b) Schematic geometrical visualization of Ti-Ti plane. (c) FESEM micrograph for 0.7 of x, inset shows the grain size distribution. (d) XPS fitting results for chemical valence states of Fe

Figure 5D.1a represents the Rietveld refined XRD results for x = 0.7, orthorhombic (97.30%) crystal structure was identified with *Pbnm* space group symmetry and 2.40% of Bi<sub>2</sub>Fe<sub>4</sub>O<sub>9</sub> secondary phase was observed. Rietveld refined data revealed that a single-phase rhombohedral (R) crystal structure with *R3c* space group symmetry was identified for pure BFO (x = 0), (matches with ref. JCPDS no. 98-002-8027) shown in Figure 5D.2a. Refined data shows that the phase fraction is 10.20% rhombohedral and 89.30% orthorhombic (O) for x = 0.6 with R3c + Pbnm space group symmetry respectively [1] with a minimal impurity phase of BiO<sub>2</sub> (0.50%) as shown in Figure 5D.2b.

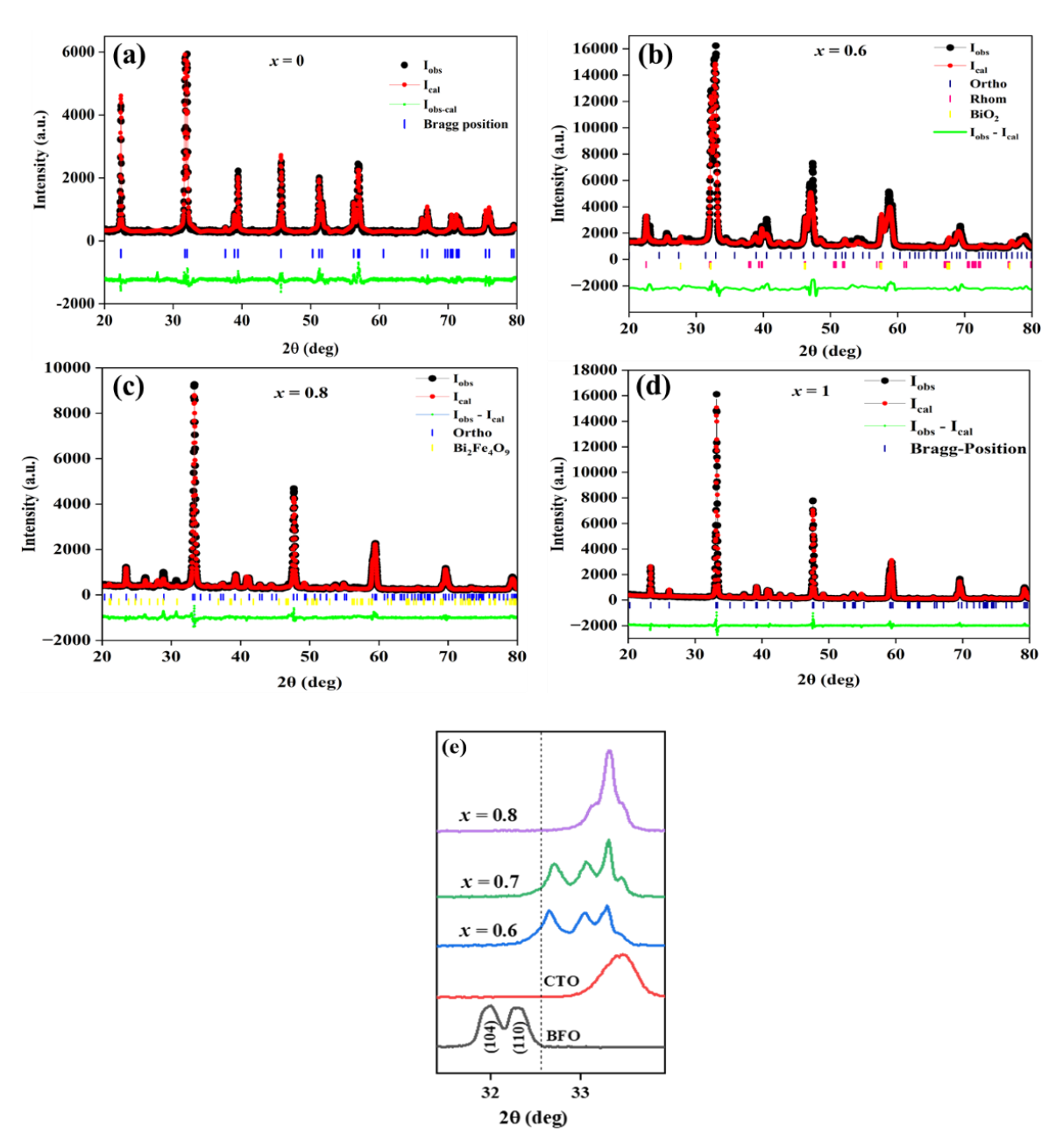


Fig 5D. 2 Refinement analyzed results of XRD for 0 of x (a), 0.6 of x (b), 0.8 of x (c), 1 of x (d), and (104), (110) peaks shifting, broadening, and merging in the vicinity of 33°.

The single-phase orthorhombic crystal structure was identified for x = 0 and 1.0, as shown in Figure 5D.2(c-d). Structural parameters, the goodness of fit, and the phase fractions of (1-x) BFO–xCTO (x = 0, 0.6, 0.7, 0.8,and 1) yielded by the Rietveld refinement of the XRD results are presented in Table 5D.1. It was noted that there is a volume reduction with increasing CTO content from 227.40 Å<sup>3</sup> (x = 0.6) to 224.18 Å<sup>3</sup> (x = 0.8). Though CTO possesses high structural stability, secondary phases like Bi<sub>2</sub>Fe<sub>4</sub>O<sub>9</sub> are prone to form due to the volatile nature of Bi at high-temperature sintering conditions [2-3]. Figure 5D.2e shows the XRD pattern of BFO in the vicinity of 32° where the diffraction peaks (104) and (110) shifted towards higher diffraction angles with splitting, broadening, and merging into a single peak which states that the solid ceramics undergo a phase transformation from R to O. The reduction in volume and shifting of BFO diffraction peaks to higher diffraction angles is ascribed to the partial substitution of lower ionic radii of Ca<sup>2+</sup> (100 pm) for A site (Bi<sup>3+</sup>, 103 pm) and Ti<sup>4+</sup> (60.5 pm) for B site (Fe<sup>3+</sup>, 64.5 pm) [4].

Table 5D. 1 Structural parameters of (1-x)BFO - xCTO yielded by the Rietveld refinement of the XRD results.

	Ortho	Lattic	attice parameters (Å)		(ų)	Rhom	Lattice p	arameters (Å)	(ų)	D' E O	2
<i>x</i>	(%)	a	b	c	V	(%)	a	c	V	Bi <sub>2</sub> Fe <sub>4</sub> O <sub>9</sub>	χ²
0	-	-	-	-	-	100	5.5845	13.8841	375.0010	-	1.82
0.6	89.8	5.4933	7.6500	5.4111	227.4003	10.2	5.5245	13.5572	358.3344	-	4.46
0.7	97.3	5.4742	7.6656	5.3977	226.5107	0.3	5.9802	14.2999	442.9047	2.4	4.61
0.8	97.0	5.4411	7.6461	5.3885	224.1844	-	-	-	-	3	1.76
1	100	5.4321	7.6444	5.3860	223.6621	-	-	-	-	-	1.66

# **5D.1.1 Geometrical representation of BFO-CTO**

The schematic geometrical representation of (1-x) BFO–xCTO for x = 0.7 is depicted in Figure 5D.1b. VESTA tool was used to visualise and measure angles between the planes and atoms. The angle between the Ti1-Ti1 plane was identified as  $\alpha = 147.9539^{\circ}$  for x = 1 and  $\alpha = 148.1917^{\circ}$  for x = 0.6, 0.7, and 0.8 shown in Figure 5D.3. Interestingly, there is a slight deviation in the angles between the planes and atoms, resulting in a distorted perovskite crystal structure with the incorporation of CTO into the BFO matrix. The variation of angles between the planes and atoms is illustrated in Table 5D.2.

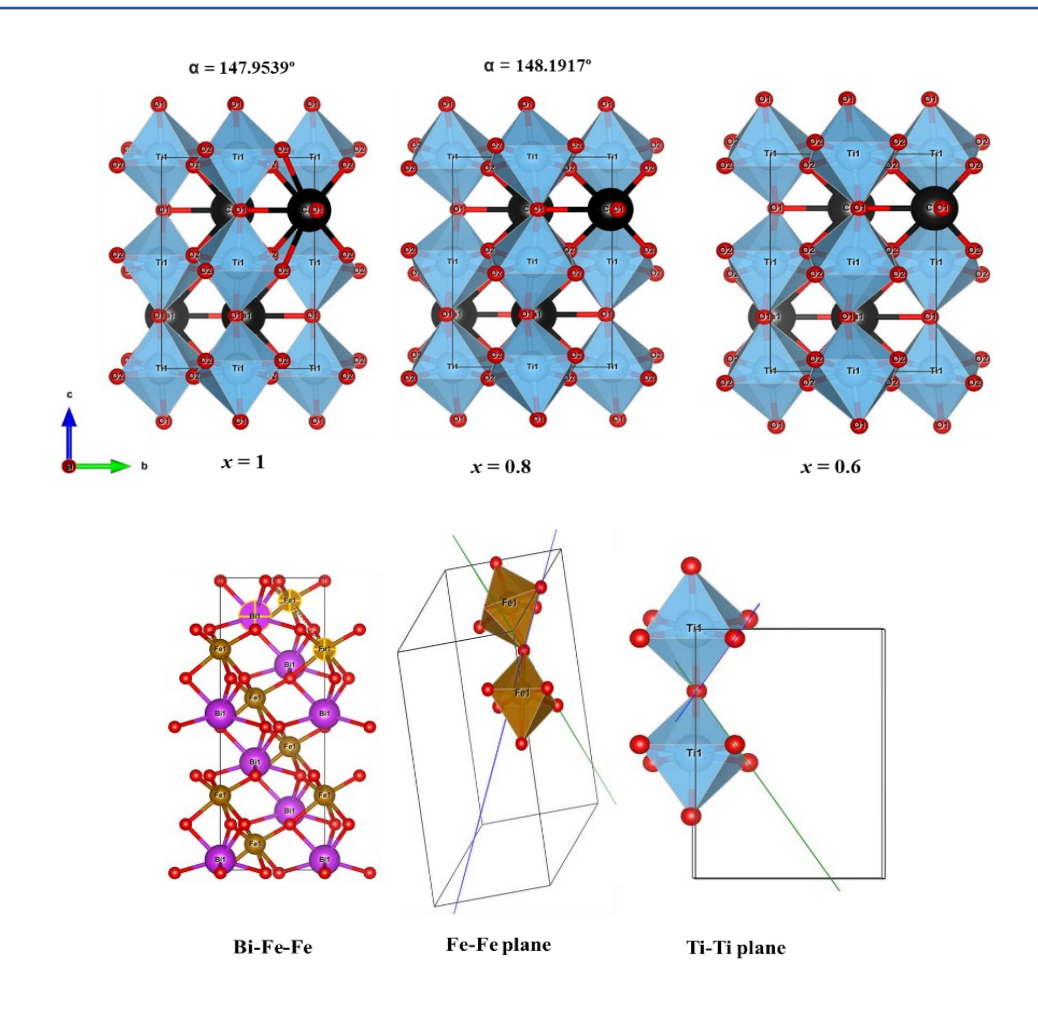


Fig 5D. 3 Schematic geometrical visualization of the Ti-Ti plane and Fe-Fe plane of (1-x) BFO - xCTO (x = 1, 0.8, 0.6, and 0)

Table 5D. 2 Angles between planes and atoms yielded from the geometrical representation of (BiFeO3) (1-x) - (CaTiO3)(x) for x = 0, 0.6, 0.7, 0.8 and 1

x	Angle between planes (°)	Ti1-O1-Ca1	Ti1-Ca1-Ti1	Ti1-Ti1-Ti1	Ti1-Ti1-Ca1	Ca1-Ca1-Ca1
1	147.9539	90.64	74.169	60.419	88.271	46.219
0.8	148.1917	93.7315	71.3304	60.3461	89.4699	44.8477
0.7	148.1917	93.7315	71.3304	60.3461	89.4699	44.8477
0.6	148.1917	93.7315	71.3304	60.3461	89.4699	44.8477

x = 0	Angle between the atoms (°)
Bi1-Fe1-Fe1	58.1215
Fe1-Bi1-Bi1	118.5026
Bi1-Bi1-Bi1	54.6018

#### 5D. 2. Microstructural analysis

The microstructure of the sintered (1-x) BFO– xCTO for x = 0.7 is shown in Figure 5D.1c. The homogeneous and highly dense microstructure was observed with an average grain size (AGS) of ~5.8 µm. The grain size distribution data is fitted to the Gauss function and shown in the inset of Figure 5D.1c. The FESEM microstructure of pure BFO exhibits poor densification with many pores confined substantially near the grain boundaries [Fig 5D.4(a)]. Even though pure BF exhibits the porous microstructure in larger surface areas, due to the incorporation of CTO, BFO-CTO solid-solution exhibits relatively porosity-free and dense micrograph and fractured surface microstructure is visible for x = 0.6 and 0.8 [Fig 5D.4 (b-c)] and for x = 0.7 [Fig 5D.4(g)]. The grain size distribution data is fitted to the Gauss function and shown in Figure 5D.4(d-f) inset.

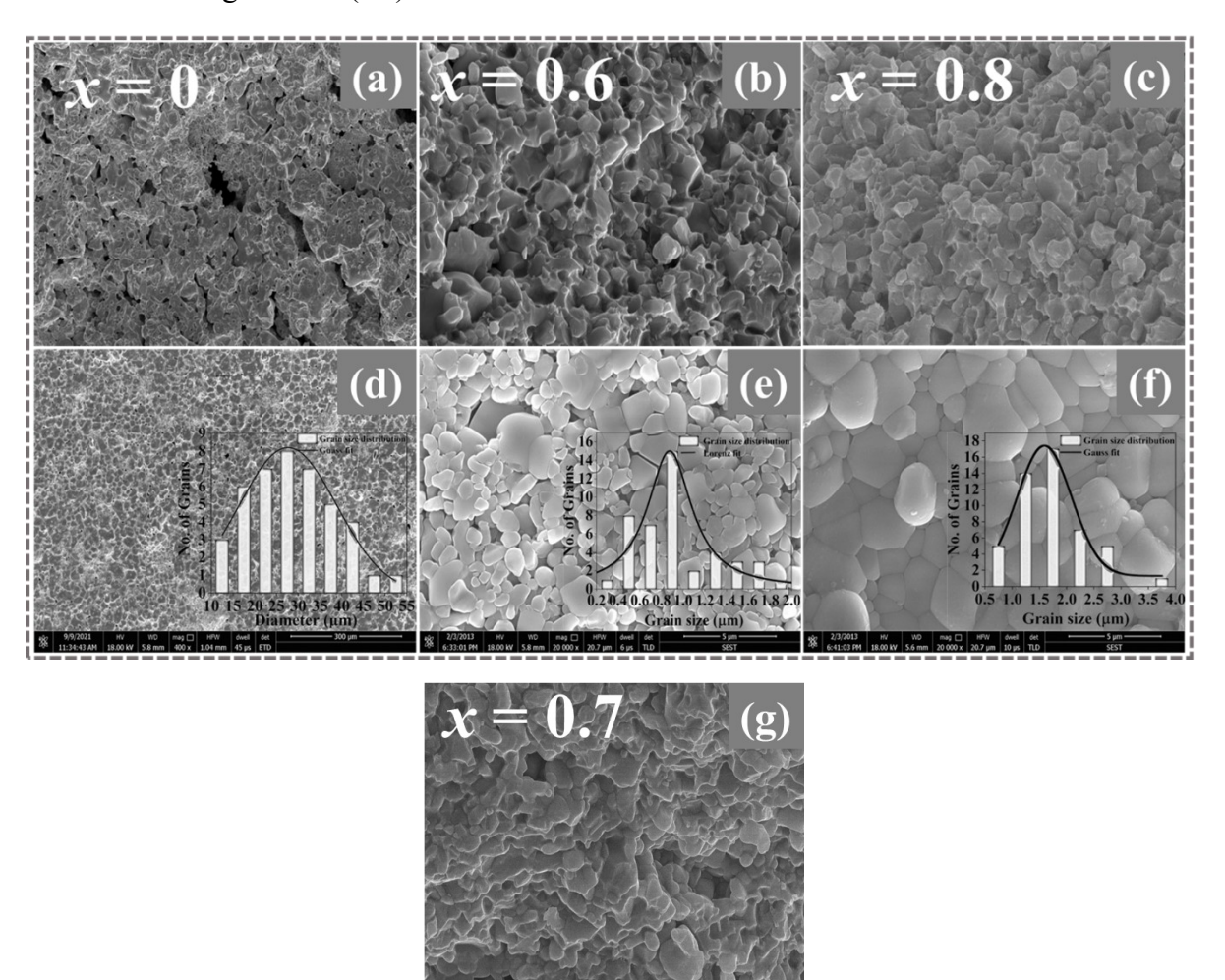


Fig 5D. 4 FESEM micrographs of fractured surface for (a) x = 0, (b) x = 0.6, (c) x = 0.8 of, and (g) x = 0.7. The surface morphology for (a) x = 0, (b) x = 0.6, and (c) x = 0.8 insets show the grain size distribution

The AGS of pure BFO was identified as  $\sim 30~\mu m$ ; due to grain refinement there is a large deviation in the AGS of BFO-CTO solid-solution samples. It was identified as  $\sim 0.9~\mu m$ , and  $\sim 1.5~\mu m$  for x=0.6, and x=0.8 respectively. It was observed that the microstructure for x=0.7 is more homogeneous compared to x=0.6, and x=0.8. This could be attributed to the grain growth and the diffusion rate of CTO in the BFO-CTO solid solution matrix at high-temperature sintering conditions.

#### 5D. 3. X-ray photoelectron spectroscopy (XPS)

BFO-based ceramics are known to exhibit large leakage current density (J) and high dielectric loss due to the formation of Oxygen (O<sub>2</sub>) vacancies which act as charge carriers within the material prompted by chemical valence fluctuations of Fe ions [5-7].

The corresponding equation can be expressed as;

$$2Fe_{Fe} + O_O \longrightarrow 2Fe_{Fe}' + V\ddot{o} + \frac{1}{2}O_2$$

Therefore, to overcome these limitations, the best way to reduce the J is to suppress the transition of Fe<sup>3+</sup> to Fe<sup>2+</sup>. Previous investigations have demonstrated different chemical modifications to suppress the Fe transition by 1) substitution of different transition metal ions in A (Bi) site (e.g., Nd-doped BFO) [8], B (Fe) sites (namely Co, Al, Mn, and Ti etc.) [5-9] and 2) preparation of the BFO-based ABO<sub>3</sub> solid solutions mixing with other transition metal perovskites (i.e., PbTiO<sub>3</sub>, SrTiO<sub>3</sub>, and BaTiO<sub>3</sub> etc.) [10-13] Similarly, in the current investigation, the XPS results revealed that the incorporation of CTO in the BFO-CTO solid solution significantly suppressed the Fe<sup>3+</sup> to Fe<sup>2+</sup> transition by inhibiting the valency fluctuations of Fe ions, which is shown in Figure 5D.5. The Lorentzian function was used to fit  $2p_{3/2}$  peaks, and the corresponding Fe<sup>3+</sup> and Fe<sup>2+</sup> peaks were located at 710.29 eV and 708.98 eV respectively, as shown in Figure 5D.1d. An integral line technique was used to calculate the area under the fitted peaks, and the corresponding results revealed that the percentage of Fe<sup>2+</sup> declined from  $\sim 35\%$  for x = 0.6 to  $\sim 17\%$  for x = 0.8. Hence, significant inhibition of Fe<sup>3+</sup> to Fe<sup>2+</sup> is achieved by stabilizing the Fe ions' chemical valance states, thereby suppressing O<sub>2</sub> vacancies. Thus, the electric insulation of BFO-CTO is enhanced, improving recoverable energy storage performance for composite functional material.

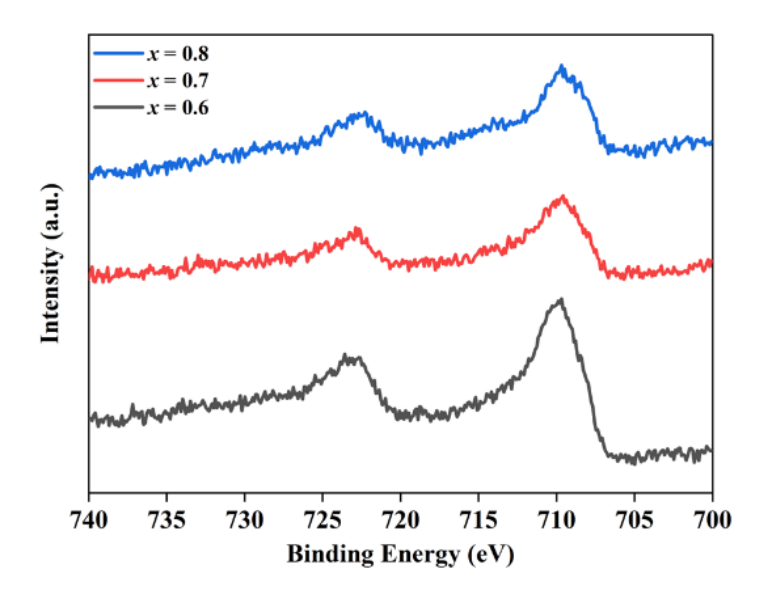


Fig 5D. 5 XPS results of BFCT ceramics for chemical valency states of Fe

#### 5D. 4. Current-Voltage (I-V) characteristics

Temperature-dependent I-V characteristics of sintered (1-x) BFO - xCTO (x = 0.6, 0.7, and 0.8) samples are represented in Figure 5D.6(a-c) and Figure 5D.7(a-c). All the samples were observed to have hysteresis behaviours starting from +voltage to -voltage. The voltage sweep is performed in a series of five parts starting from 0 to +V, +V to 0 and 0 to -V, -V to 0 and finally, 0 to +V. It was noted that the BFO-CTO exhibits a non-linear electrical behaviour throughout the voltage sweep. It was identified that the current increases with increasing temperature due to the ionization of atoms, leading to a drop in the material's resistivity [14]. Our investigation revealed that three orders of magnitude dropped the current with increasing CTO content, i.e.,  $5.53 \times 10^{-3}$ A for x = 0 (shown in Figure 5D.8) to  $9.78 \times 10^{-6}$  A for x = 0.8 at 20V at a temperature of 40°C. As we increased the temperature, the current was increased, e.g.,  $4.99 \times 10^{-6}$ A at 40 °C to  $1.54 \times 10^{-4}$ A at 200 °C for x = 0.7.

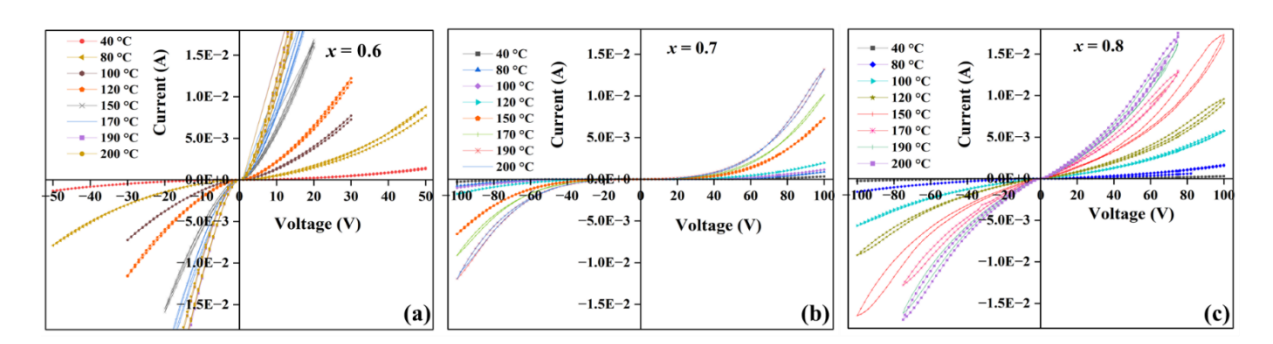


Fig 5D. 6 Temperature-dependent current-voltage hysteresis curves for 0.6 of x (a). 0.7 of x (b). 0.8 of x (c).

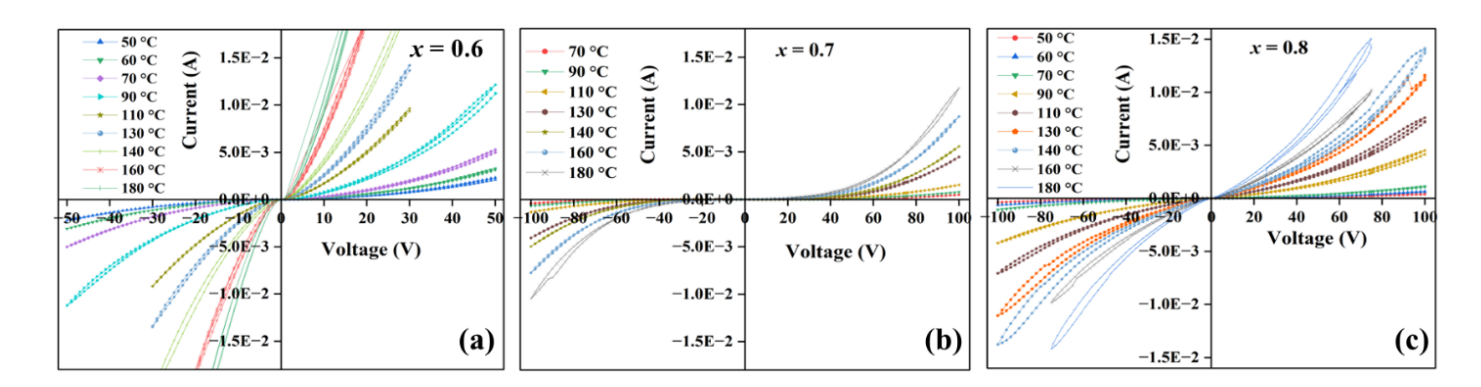


Fig 5D. 7 Temperature-dependent current-voltage hysteresis curves for 0.6 of x (a), 0.7 of x (b), and 0.8 of x (c).

Temperature-dependent current values at 20V for all the BFO-CTO solid solutions (x = 0 to x = 0.6, 0.7 & 0.8) are displayed in Table 5D.3, which fulfilled the theoretical concept of ionization in insulating ceramic materials.

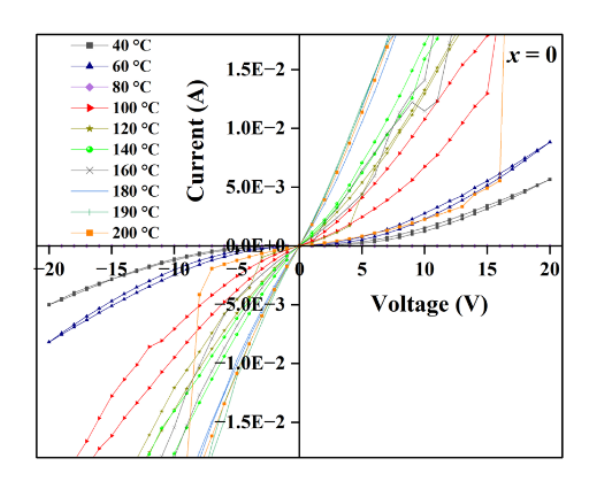


Fig 5D. 8 Temperature-dependent current-voltage hysteresis curves for 0 of x

Table 5D. 3 I-V characteristics of (	(1-x) BFO-x CTO ceramics
--------------------------------------	--------------------------

Concentration (x)	Voltage (V)	Current (A) @40°C	<b>Current (A) @200°C</b>
0	20	$5.53 \times 10^{-3}$	$5.50 \times 10^{-2}$
0.6	20	2.26 × 10 <sup>-4</sup>	2.97 × 10 <sup>-2</sup>
0.7	20	$4.99 \times 10^{-6}$	$1.54 \times 10^{-4}$
0.8	20	$9.78 \times 10^{-6}$	$2.78 \times 10^{-3}$

# **5D. 5.** Frequency-dependent dielectric properties and dielectric relaxation behaviour of BFO-CTO ceramics at room temperature

Frequency-dependent dielectric permittivity ( $\varepsilon$ ') and loss tangent ( $\tan\delta$ ) at room temperature were depicted in Figure 5D.9(a-c). In the current investigation, two different frequency range impedance analyzers were used to cover the frequency up to  $10^9$  Hz at room temperature and plotted in Figures 5D.9(a), 5D.9(b) and 5D.9(c) for x=0.6, 0.7, and x=0.8 respectively. Different colours represent the different frequency ranges of different impedance analyzers. It was observed that there is a strong frequency dependency at lower frequencies, which could be attributed to space charge accumulation at grain boundaries and extrinsic defects present in bulk ceramics. As the CTO possess strong dielectric permittivity and lower loss tangent compared to BFO ceramics, [15] thus it is noted that the current BFO-CTO ceramics displayed improved dielectric permittivity (e.g.,  $\varepsilon$ ' ~ 22 for x=0 (ref. Figure 5D.10),  $\varepsilon$ ' ~ 117 for x=0.8 at 10MHz) and reduced dielectric losses as we increase the CTO content from x=0 to x=0.8. At higher frequencies, i.e., from x=00 to x=0.80. At higher frequencies, i.e., from x=010 Hz to x=010 Hz, weak frequency dependency was observed with a marginal change of dielectric permittivity. The frequency-dependent dielectric properties confirm the relaxor nature of the ceramics by a declined value of x=020 over the increased frequencies.

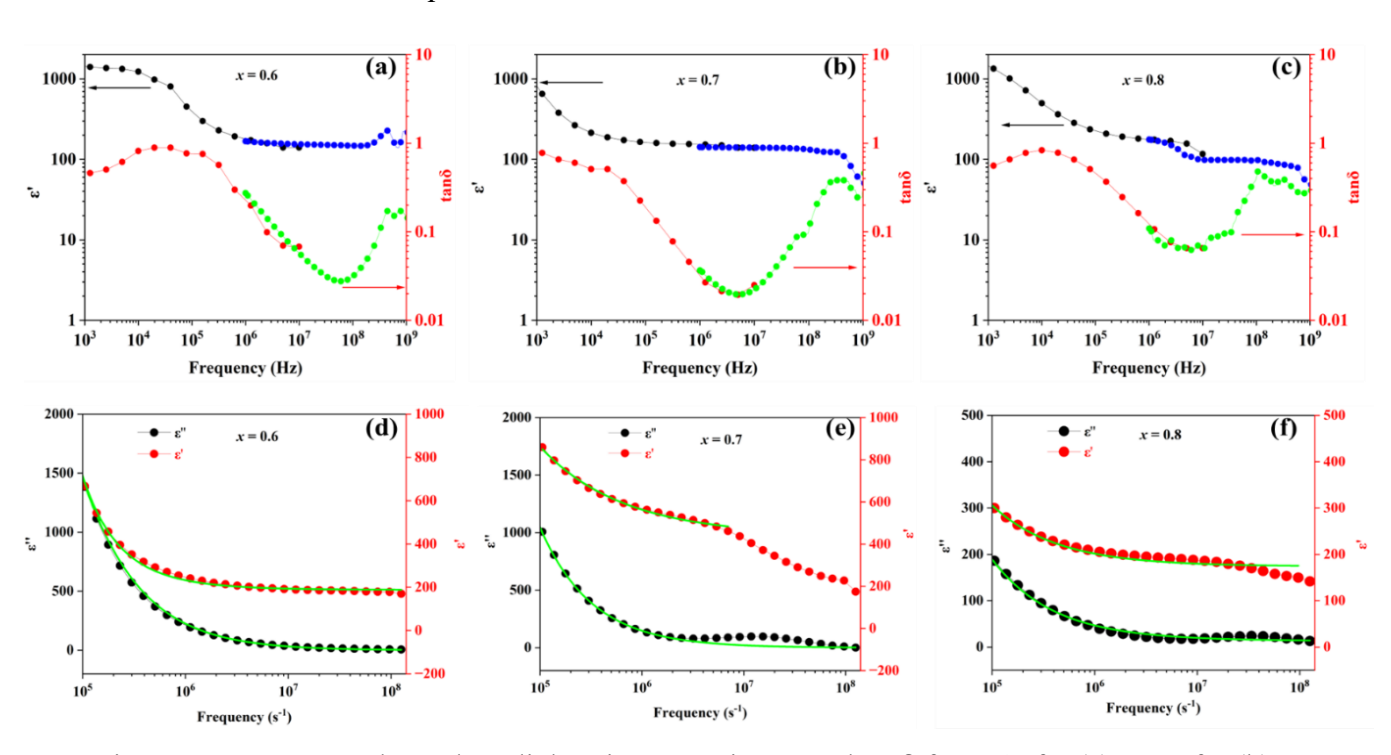


Fig 5D. 9 Frequency-dependent dielectric properties.  $\varepsilon'$  and  $\tan\delta$  for 0.6 of x (a), 0.7 of x (b) and 0.8 of x (c). Different plot colours represent different frequency ranges recorded using different impedance analyzers. (d) Cole-Cole distribution of dielectric relaxation times of  $\varepsilon'$  and  $\varepsilon''$  for x = 0.6, 0.7 of x (e) and 0.8 of x (f)

Lower tan  $\delta$  values were recorded, i.e.,  $\sim 0.10$  for x = 0 at 10 MHz,  $\sim 0.03$  for x = 0.6 at 60 MHz,  $\sim 0.01$  for x = 0.7 at 5 MHz, and  $\sim 0.06$  for x = 0.8 at 7 MHz. It is worth noting that x

= 0.7 displayed the lowest tan $\delta$  out of all the compositions. This could be ascribed to the grain size, sintering temperature conditions and electrical microstructural homogeneity.

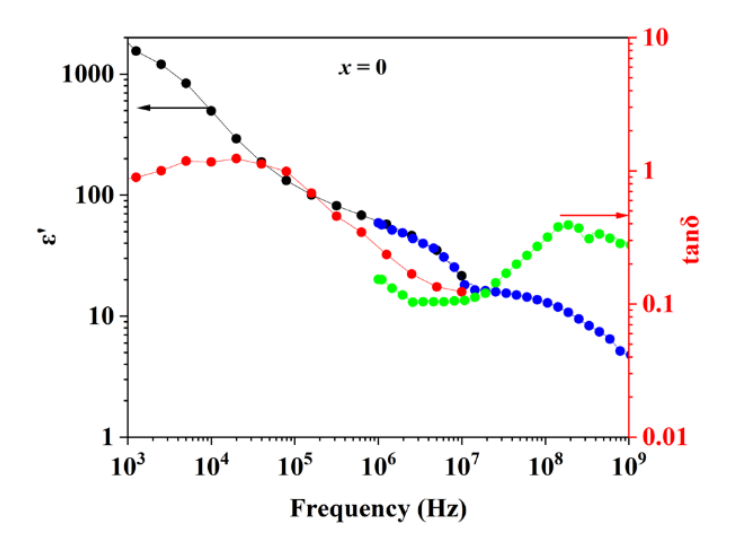


Fig 5D. 10 Frequency-dependent  $\varepsilon$ ' and  $\tan\delta$  for 0 of x, different plot colours represent different frequency ranges recorded using different impedance analyzers

#### 5D.5.1 Dielectric relaxation $(\tau)$

The complex dielectric permittivity  $\varepsilon^* = \varepsilon'$  - i", real part ( $\varepsilon'$ ), and imaginary part ( $\varepsilon''$ ) have been recorded in the frequency range of 16 kHz  $\leq f \leq$  3 GHz to study the dielectric relaxation behaviour [16-19] of (1-x) BFO-(x) CTO ceramics as shown in the Figures 5D.9(d-f), (16 kHz  $\leq f \leq$  20 MHz) for x = 0.6, 0.7, and 0.8 respectively. The dielectric relaxation time is calculated using Cole-Cole distribution functions, which are derived from the modified Debye equation [20] as follows;

$$\varepsilon^* = \varepsilon' - i \varepsilon'' = \varepsilon_{\infty} + \frac{(\varepsilon_0 - \varepsilon_{\infty})}{1 + (i\omega\tau)^{1-\alpha}}$$

modified equation for  $\varepsilon'$  as a function of  $\omega$ 

$$\varepsilon'(\omega) = \varepsilon_{\infty} + \frac{(\varepsilon_0 - \varepsilon_{\infty}) \left(1 + \cos\left(\frac{\beta\pi}{2}\right) (\omega\tau)^{\beta}\right)}{1 + 2 (\omega\tau)^{\beta} \cos\left(\frac{\beta\pi}{2}\right) + (\omega\tau)^{2\beta}}$$
 (2)

modified equation for  $\epsilon''$  as a function of  $\omega$ 

$$\varepsilon''(\omega) = (\varepsilon_0 - \varepsilon_\infty) \frac{(\omega \tau)^\beta \sin(\frac{\beta \pi}{2})}{1 + 2(\omega \tau)^\beta \cos(\frac{\beta \pi}{2}) + (\omega \tau)^{2\beta}} \longrightarrow (3)$$

Here  $\omega$  is  $2\pi f$ ,  $\tau$  is the mean dielectric relaxation time,  $\varepsilon_0$  (static permittivity  $\omega \to 0$ ) is the permittivity at extremely low frequency, and  $\varepsilon_{\infty}$  is defined as permittivity at high frequency.

Debye equation is extensively used for the non-interacting identical electric dipoles which have uniform dielectric relaxation times.  $\alpha$  (controls the width of the distribution),  $\beta$  are the fitting parameters vary from 0 to 1 ( $0 \le \alpha$ ,  $\beta \le 1$ ) and  $\beta = 1$ -  $\alpha$ , if  $\alpha = 0$  or  $\beta = 1$ , the equations (1), (2), and (3) are simplified to the renowned Debye equation. In the current investigation equations 2) and (3) are used to predict the  $\tau$  values for interacting dipoles with different dielectric relaxation times. The trend followed by  $\varepsilon'(f)$  and  $\varepsilon''(f)$  at  $\omega = 1/\tau$  is almost similar with a marginal uncertainty at the lower frequencies (16 kHz  $\leq f \leq$  20 MHz). It was noted that there is a sharp rise of  $\varepsilon'$  and  $\varepsilon''$  values with decreasing frequency. Table 5D.4 displays the variation of exponents  $\alpha$ ,  $\beta$  and  $\tau$  (yielded by cole-cole distribution fittings) with varying material composition (x = 0, 0.6, 0.7, and 0.8).  $\tau'$  values corresponding to  $\varepsilon'(f)$  are ~135 $\mu$ sec, ~44 $\mu$ sec and  $\sim 265 \mu \text{sec}$  for x = 0.6, 0.7 and 0.8 respectively. Interestingly, 0.7 of x displayed a lower relaxation time than 0.6, 0.8 of x.  $\tau''$  values corresponding to  $\varepsilon'(f)$  follow the same fashion as  $\tau'$ (ref. Table 5D.4). The  $\tau$ ' and  $\tau$ " values corresponding to  $\varepsilon$ '(f), and  $\varepsilon$ "(f) at higher frequencies (1 MHz $\leq f \leq$  3 GHz) are depicted in Table 5D.5. It was seen that the relaxation times are uncertain for CTO concentration in  $0.6 \le x \le 0.8$  with huge error bars (e.g.,  $1.08 \times 10^{-11} \pm 2.07 \times 10^{-9}$  for 0.6 of x) and  $\beta = 1 \text{ for } 0.6, 0.8 \text{ of } x. \epsilon', \epsilon''$  follow the different trends and are extremely sensitive to the frequency chosen to fit the data as displayed in Figure 5D.11(a-d).

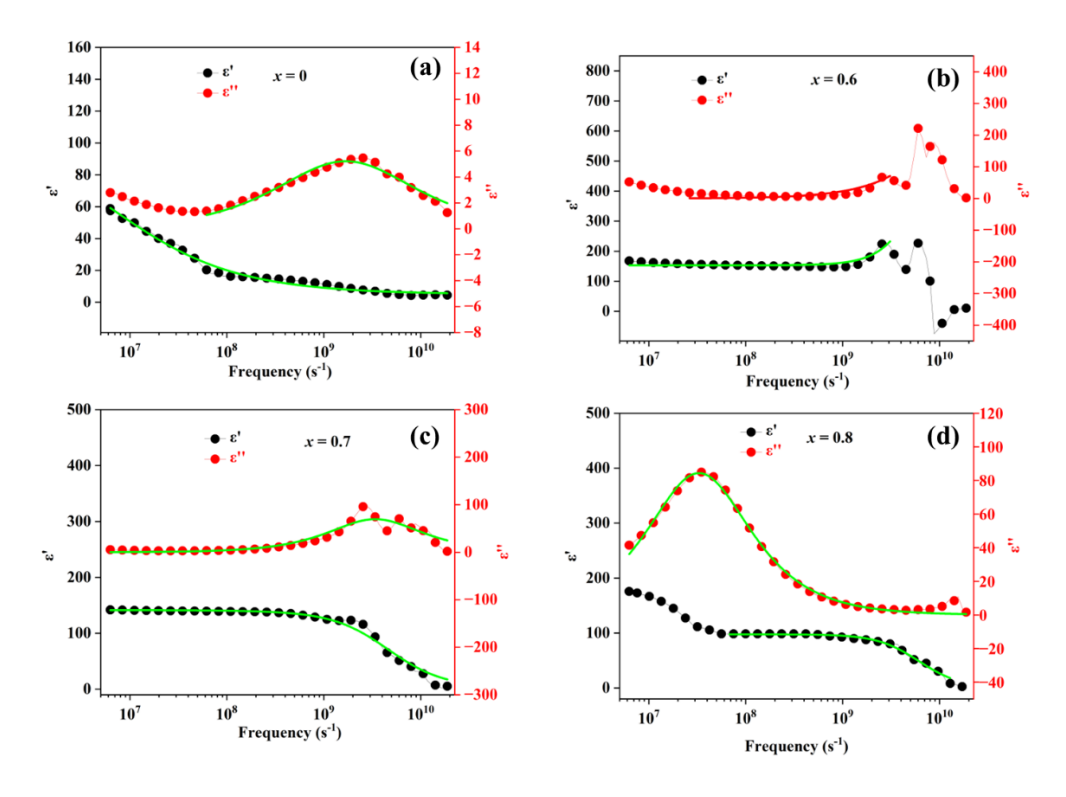


Fig 5D. 11 Cole-Cole distribution of dielectric relaxation times of  $\varepsilon'$  and  $\varepsilon''$  for (a) x = 0, (b) x = 0.6, (c) x = 0.7, and (d) x = 0.8

 $\beta$  = 1 (pure Debye relaxation) indicates the non-interacting dipoles phenomenon in which the relaxation process is direct and not influenced by interaction among the neighbour dipoles and exhibits perfectly simpler exponential relaxation behaviour.

Table 5D. 4 Dielectric relaxation times yielded by cole-cole distribution fittings within the frequency range  $16 \text{ kHz} \le f \le 20 \text{ MHz}$ .

x	τ' (sec)	τ'' (sec)	α'	α''	β'	β''
0.6	$1.35 \times 10^{-4} \pm 6.25 \times 10^{-6}$	$1.00 \times 10^{-4} \pm 2.26 \times 10^{-6}$	0.15	0.17	0.85	0.83
0.7	$4.44 \times 10^{-5} \pm 2.21 \times 10^{-6}$	$5.91 \times 10^{-5} \pm 3.43 \times 10^{-6}$	0.22	0.14	0.78	0.86
0.8	$2.65 \times 10^{-4} \pm 3.30 \times 10^{-6}$	$1.31 \times 10^{-4} \pm 9.23 \times 10^{-6}$	0.30	0.18	0.70	0.82

Table 5D. 5 Dielectric relaxation times yielded by cole-cole distribution fittings within the frequency range 1 MHz  $\leq$  f  $\leq$  3 GHz

x	τ' (sec)	τ'' (sec)	α'	α''	β'	β''
0	$1.51 \times 10^{-7} \pm 7.80 \times 10^{-8}$	$5.91 \times 10^{-10} \pm 1.46 \times 10^{-11}$	0.44	0.23	0.56	0.77
0.6	$8.73 \times 10^{-11} \pm 3.11 \times 10^{-10}$	$1.08 \times 10^{-11} \pm 2.07 \times 10^{-9}$	0	0.22	1	0.78
0.7	$1.50 \times 10^{-9} \pm 3.90 \times 10^{-10}$	$2.94 \times 10^{-10} \pm 1.55 \times 10^{-11}$	0.12	0	0.88	1
0.8	$1.63 \times 10^{-10} \pm 1.30 \times 10^{-11}$	$3.03 \times 10^{-8} \pm 0.00$	0	0.06	1	0.94

## **5D. 6.** Temperature-dependent dielectric properties and relaxor ferroelectric behaviour of BFO-CTO ceramics

Temperature-dependent relative permittivity ( $\varepsilon_r$ ), tan $\delta$  of BFO-CTO ferroelectrics is depicted in Figures 5D.12(a-c) and Figure 5D.13. Relative permittivity ( $\varepsilon_r$ ), maximum permittivity ( $\varepsilon_m$ ) and tan $\delta$  (ref. Figure 5D.13 representative results for x=0.7) drop with increasing frequency is a preliminary indication of the transition from FE to relaxor ferroelectric RFE nature. The obtained results agree with the earlier reports on BFO-based ceramics. [21-24]. It was observed that the maximum temperature ( $T_m$ ) shifted to higher values with increasing CTO content initially (e.g., ~270 °C for x=0.6 and ~450 °C for x=0.7) and then decreased (e.g., ~350 °C for x=0.8). The results revealed that the double and triple dielectric anomaly is observed at 180 °C, 270 °C for x=0.6 and 238 °C, 350 °C, and 420 °C

for x = 0.8 (ref. Figures 5D.12a, 5D.12c). The observed anomalies are ascribed to the heterogeneously distributed electrical/core-shell microstructure or the response of the grain boundaries within the (BFO-based) electroceramic materials, which leads to the concentration of electrical field at some areas of the microstructure.

Curie-Weiss law is utilized to perform the quantitative analysis of RFE properties, the equation is as follows;

$$\frac{1}{\varepsilon_r} - \frac{1}{\varepsilon_m} = \frac{(T - Tm)^{\gamma}}{C}$$

where C is the constant and  $\gamma$  is the degree of diffusivity ( $1 \le \gamma \le 2$ ), 1 represents normal ferroelectric and 2 illustrates ideal RFEs. [25] The  $\gamma$  values are determined using the functions, ln ( $1/\varepsilon_r$  - $1/\varepsilon_m$ ) on the axis of ordinate and ln (T- $T_m$ ) on abscissa displayed in Figures 5D.12 (a-c) [bottom panel] for 0.6 of x ( $\gamma = 1.69$ ), 0.7 of x ( $\gamma = 1.84$ ) and 0.8 of x ( $\gamma = 1.76$ ) respectively. The interesting point is that CTO concentration of 0.7 possesses the strongest RFE nature compared to 0.6 and 0.8.

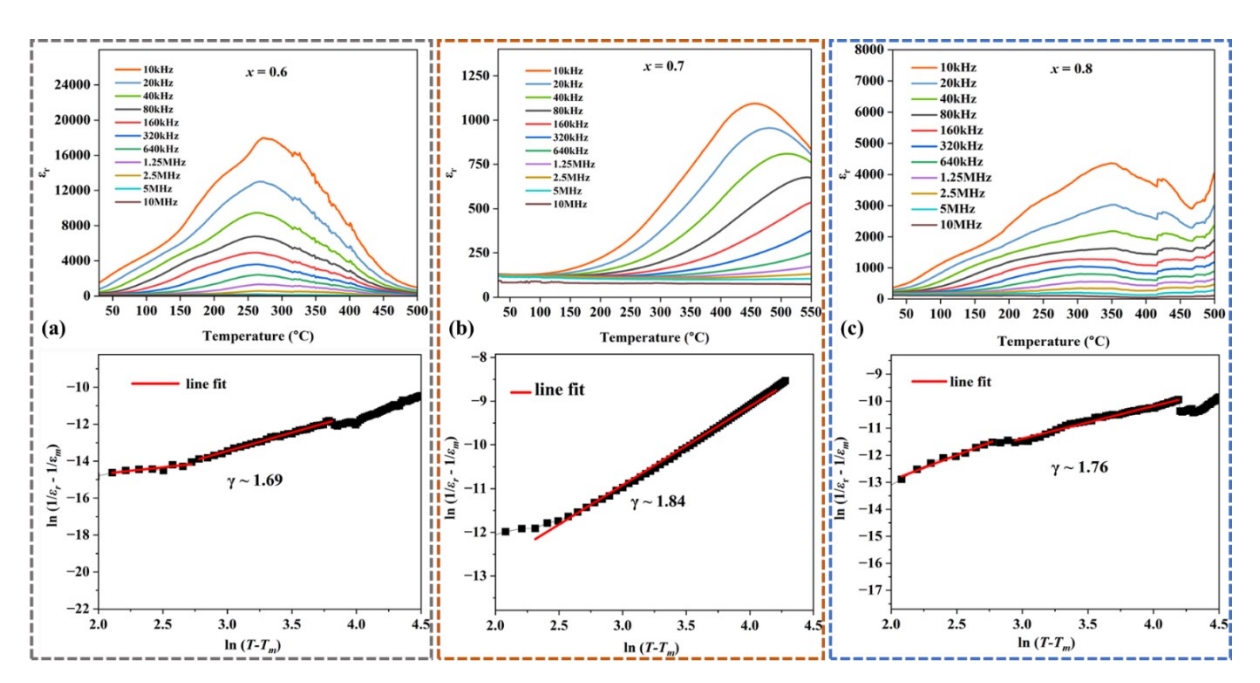


Fig 5D. 12 Temperature-dependent dielectric permittivity of (1-x) BFO – x CTO ceramics measured at 10 kHz - 10 MHz and the corresponding Curie-Weiss law fitting for x = 0.6 (a), 0.7 of x (b) and 0.8 of x (c)

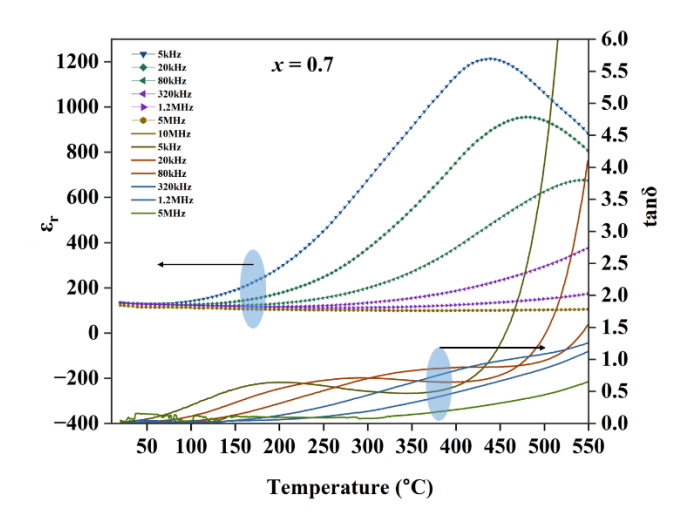


Fig 5D. 13 Temperature-dependent  $\varepsilon_r$  and  $\tan\delta$  for 0.7 of x

#### 5D. 7. Polarization – Electric field (*P-E*) loops of BFO-CTO ceramics

Temperature-dependant, and time-dependent and voltage dependant P-E hysteresis loops of BFO-CTO RFEs (for x = 0.7 value) are shown in Fig 5D.14(a), 5D.14 (b) and 5D.14 (c) respectively. Supplementary Figure 5D.15(a-c) further depicts the entire measurement range for all the temperature and time-dependent P-E hysteresis loops. Fig 5D.14(d) demonstrates the maximum recoverable energy density ( $W_{\rm rec}$ ) of 2.5 J cm<sup>-3</sup> [green shaded area], and the corresponding energy loss ( $W_{\rm loss}$ ) of 4.65 J cm<sup>-3</sup> [red shaded area] using the P-E hysteresis loop measured at the room temperature and at applied EF 66.66kV cm<sup>-1</sup> (120 msec) Similar calculations of  $W_{\rm rec}$ ,  $W_{\rm loss}$ , efficiency ( $\eta$ ) and maximum polarization ( $P_{\rm max}$ ) are performed using each P-E hysteresis loops measured at an electric field (EF) of 33.33 kV/cm [Fig 5D.14 (a-b) and 5D.15 (a-b)]. Temperature and time dependence of  $W_{\rm rec}$  and  $W_{\rm loss}$  are displayed in Figures 5D.16(a) and 5D.16(c) respectively, whereas Figures 5D.16(b) and 5D.166(d) demonstrate the variation of  $\eta$  and  $P_{\rm max}$  with temperature and time respectively. Supplementary Figure 5D.17 records the time variation of these parameters ( $W_{\rm rec}$ ,  $W_{\rm loss}$ ,  $\eta$  and  $P_{\rm max}$ ) using PE loops measured at the applied EF 66.66kV/cm. Table 5D.6 organizes all the relevant data in a concise and useful manner.

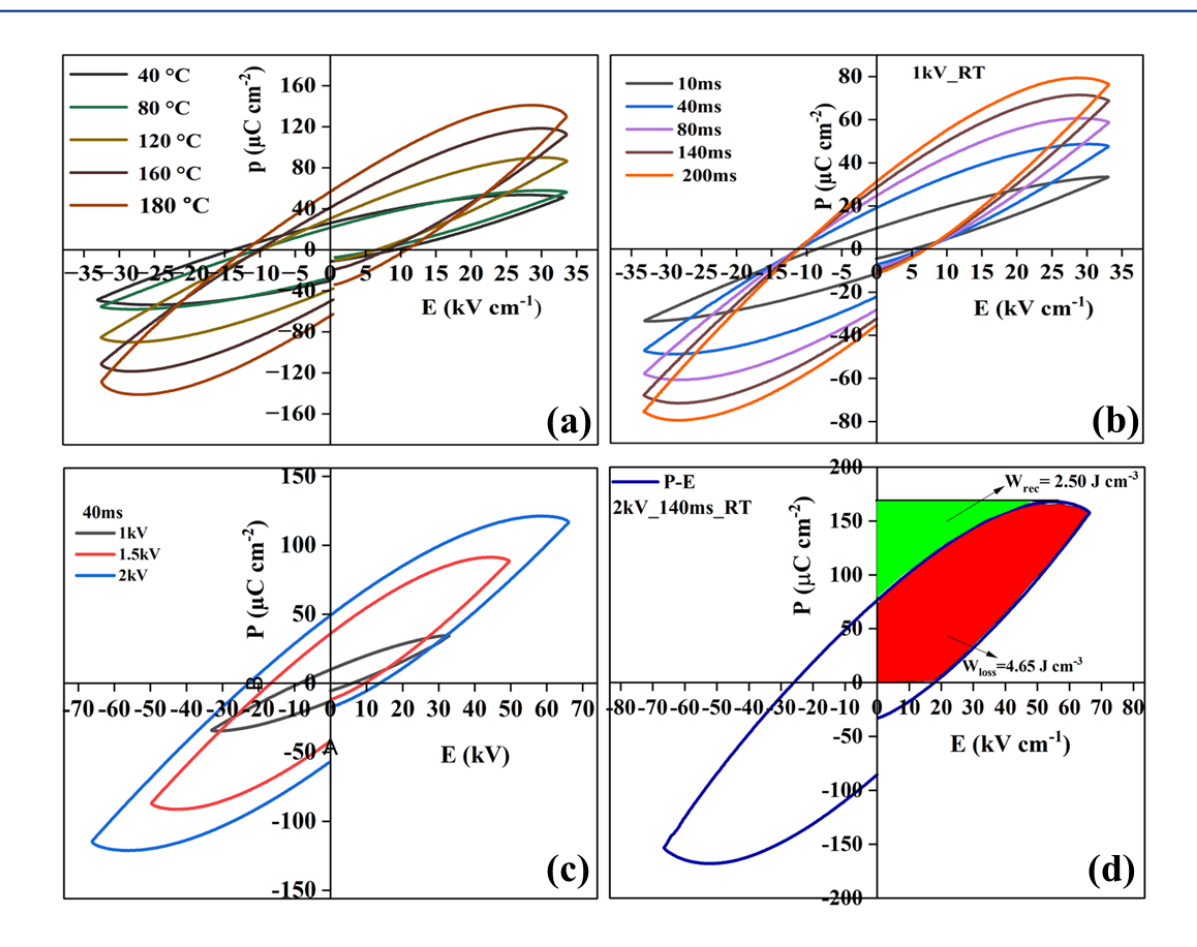


Fig 5D. 14 (a) Temperature-dependent P-E loops at a field of 33.33 kV cm<sup>-1</sup> for 0.7 of x. (b) Time-dependent P-E loops at an electric field of 33.33 kV cm<sup>-1</sup> for 0.7 of x. (c) Variation of electric field-dependent P-E curves measured at a period of 40 ms for 0.7 of x. (d) W<sub>rec</sub>, W<sub>loss</sub>, schematic representation at an electric field of 66.66 kV cm<sup>-1</sup> at a period of 140 ms.

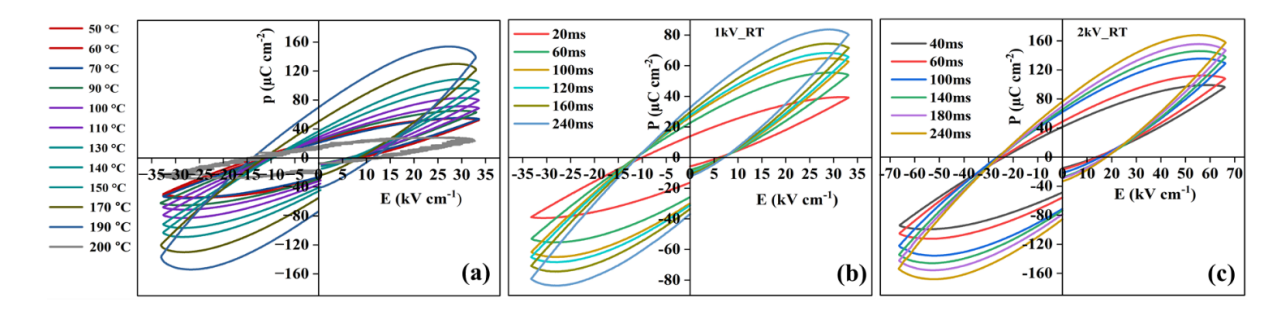


Fig 5D. 15 (a) Temperature-dependent P-E loops at an electric field of 33.33 kV cm-1 (b) Time-dependent P-E loops at an electric field of 33.33 kV cm<sup>-1</sup> (c) Time-dependent P-E loops at an electric field of 66.66 kV cm<sup>-1</sup> (x =0.7 in all cases).

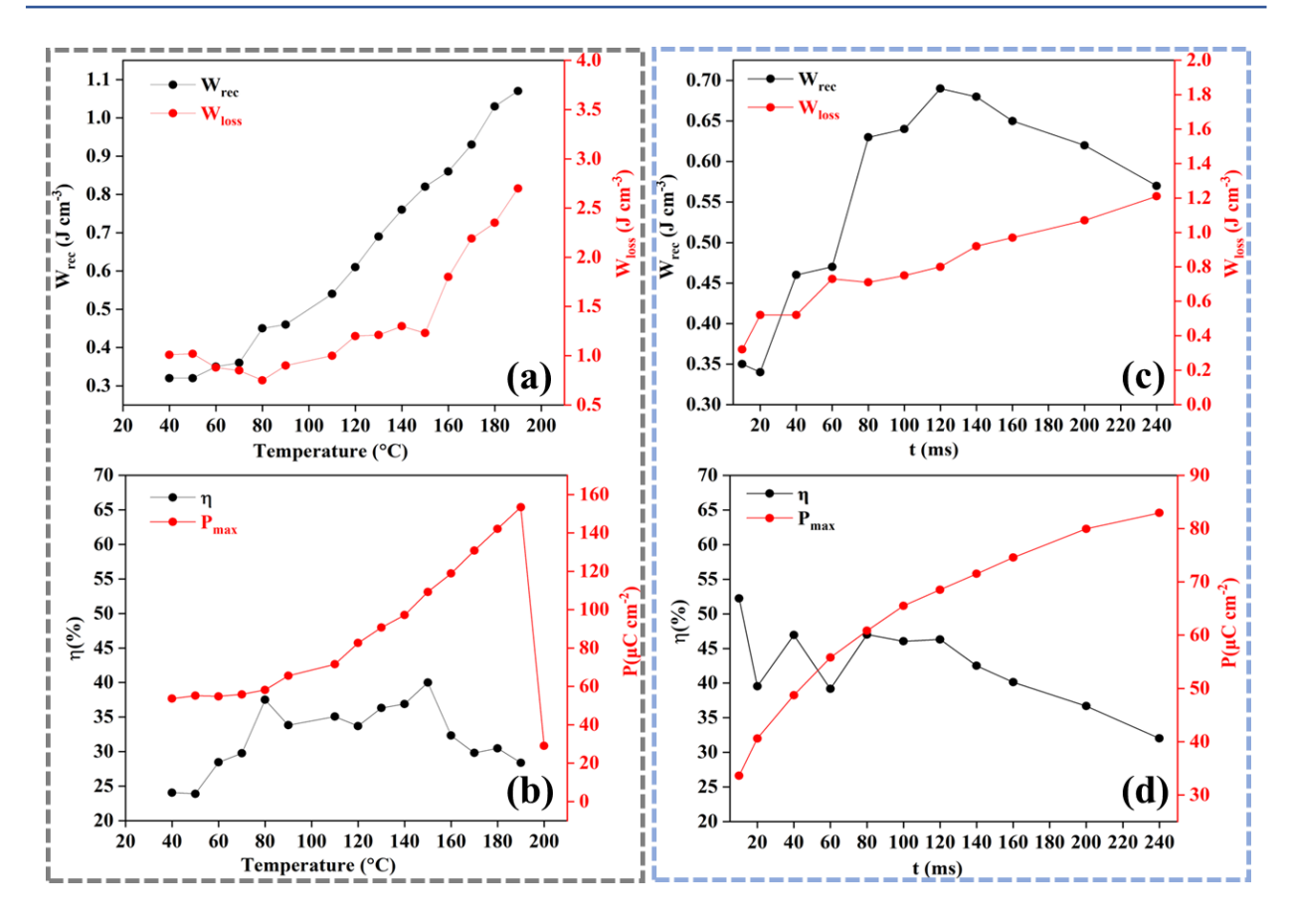


Fig 5D. 16 (a) Variation of temperature-dependent Wrec, Wloss, Pmax, and  $\eta$  for 0.7 of x at an electric field of 33.33 kV cm<sup>-1</sup>. (b) Variation of time-dependent Wrec, Wloss, Pmax, and  $\eta$  for 0.7 of x at an electric field of 33.33 kV cm<sup>-1</sup>.

Temperature-dependent P-E curves of BFO-CTO RFEs at an electric field (EF) of 33.33 kV/cm revealed that the  $P_{\rm m}$  and  $P_{\rm r}$  increases with temperature monotonically from 40 °C ( $P_{\rm m}\sim$  53.59  $\mu$ C cm<sup>-2</sup>,  $P_{\rm r}\sim$  26.34  $\mu$ C cm<sup>-2</sup>) to 190 °C ( $P_{\rm m}\sim$  153.43  $\mu$ C cm<sup>-2</sup>,  $P_{\rm r}\sim$  68.92  $\mu$ C cm<sup>-2</sup>) (ref. Figures 5D.14a, 5D.15a). The time-dependent P-E curves under the electric field (EF) of 33.33 kV cm<sup>-1</sup> and 66.66 kV cm<sup>-1</sup> were displayed the monotonical increment of  $P_{\rm m}$ ,  $P_{\rm r}$  (e.g., 9.52  $\mu$ C cm<sup>-2</sup> (10 ms), 31.78  $\mu$ C cm<sup>-2</sup> (240 ms) at 33.33 kV cm<sup>-1</sup> and 40.53  $\mu$ C cm<sup>-2</sup> (40 ms), 75.80  $\mu$ C cm<sup>-2</sup> (240 ms) at 66.66 6 kV cm<sup>-1</sup>) [ref. Figures 5D.14b, 5D.15(b-c)].

 $W_{\rm rec}$ ,  $W_{\rm loss}$ , and  $P_{\rm m}$  increase with temperature (40 °C to 190 °C) and time (10 ms to 240 ms) with marginal variations.  $P_{\rm m}$  abruptly drops at 200 °C due to unstable P-E curves, as shown in Figures 5D.16(a-d), 5D.17. The results revealed that there is no considerable efficiency drop up to 190 °C with stable P-E curves, which suggests that this material can be used for high-temperature energy storage applications. P-E measurements were carried out at various EFs i.e., 33.33 kV cm<sup>-1</sup>, 50 kV cm<sup>-1</sup> and 66.66 kV cm<sup>-1</sup> (ref. Figure 5D.14c).

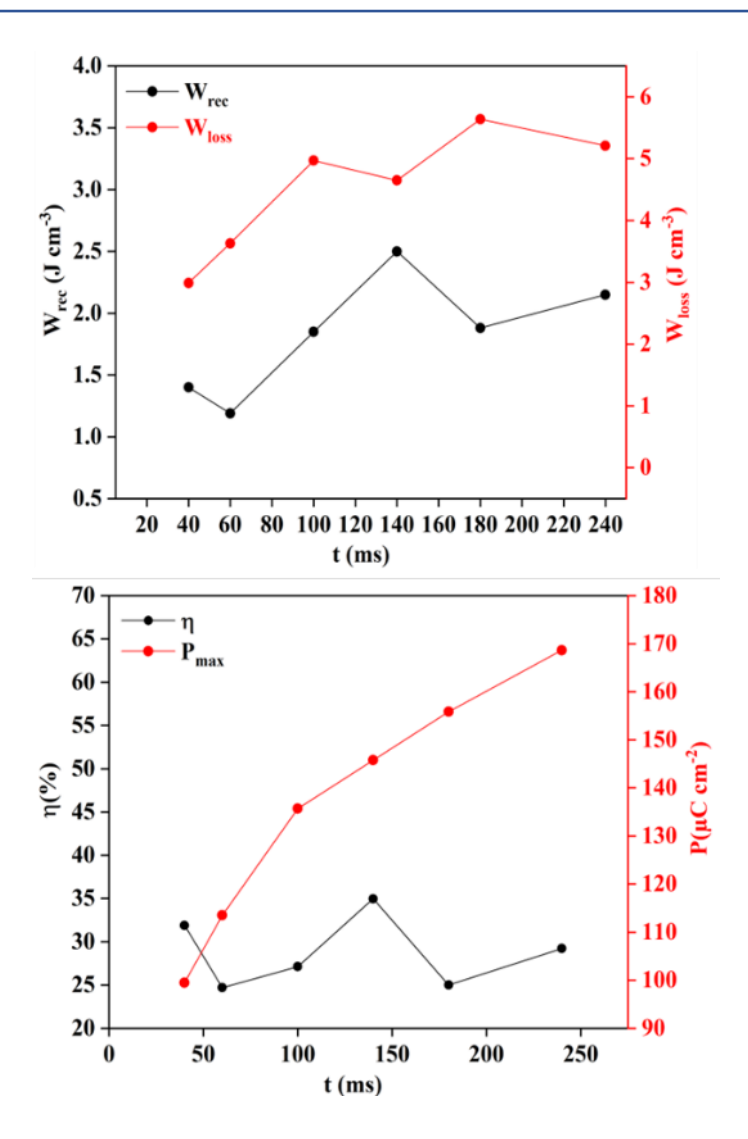


Fig 5D. 17 Variation of time-dependent  $W_{rec}$ ,  $W_{loss}$ ,  $P_{max}$ , and  $\eta$  for 0.7 of x at an electric field of 66.66 kV cm<sup>-1</sup>

We have not reached the saturation point  $P_{\rm m}$  at this point of investigation. It was noted that  $P_{\rm m}$  is increasing with increasing EF further confirming the depletion of long-range FE orders and the emergence of dynamic PNRs. Unlike the long-range FE orders, dipoles are sensitive towards applied EF in PNRs by which higher  $P_{\rm m}$ ,  $W_{\rm rec}$  and  $\eta$  can be obtained.

Table 5D. 6 Recoverable energy density ( $W_{rec}$ ), loss ( $W_{loss}$ ), efficiency( $\eta$ ) and maximum
polarization (Pmax) for $x = 0.7$

1	1 kV  40 ms  (f = 25  Hz)  x = 0.7					1 kV RT, x = 0.7				2kV RT, x = 0.7				
Temp	Wrec	Wloss	η	P <sub>max</sub>	Time	Wrec	W <sub>loss</sub>	η	P <sub>max</sub>	Time	Wrec	W <sub>loss</sub>	η	P <sub>max</sub>
°C	J/cm <sup>3</sup>	J/cm <sup>3</sup>	%	μC/cm <sup>2</sup>	ms	J/cm <sup>3</sup>	J/cm <sup>3</sup>	%	μC/cm <sup>2</sup>				-	
40	0.32	1.01	24.06	53.59					•	ms	J/cm <sup>3</sup>	J/cm <sup>3</sup>	%	μC/cm <sup>2</sup>
50	0.32	1.02	23.86	55.12	10	0.35	0.32	52.23	33.61					
60	0.35	0.88	28.48	54.78	20	0.34	0.52	39.53	40.61	40	1.4	2.99	31.89	99.49
70	0.36	0.85	29.75	55.8	40	0.46	0.52	46.93	48.72					
80	0.45	0.75	37.50	58.12		0.40				60	1.19	3.63	24.68	113.52
90	0.46	0.90	33.82	65.53	60	0.47	0.73	39.16	55.8	60	1.19	3.03	24.00	113.32
110	0.54	1.00	35.06	71.53	80	0.63	0.71	47.01	60.83	100	1.85	4.97	27.12	125 71
120	0.61	1.20	33.70	82.62	100	0.64	0.75	46.04	65.53	100	1.63	4.97	27.12	135.71
130	0.69	1.21	36.31	90.64	100	0.64	0.73	40.04	03.33					
140	0.76	1.30	36.89	97.18	120	0.69	0.8	46.30	68.53	140	2.5	4.65	34.96	145.78
150	0.82	1.23	40.00	109.24	140	0.68	0.92	42.50	71.53					
160	0.86	1.8	32.33	118.83	160	0.65	0.07	40.12	74.50	180	1.88	5.64	25.00	155.85
170	0.93	2.19	29.80	130.77	160	0.65	0.97	40.12	74.58					
180	1.03	2.35	30.47	142.10	200	0.62	1.07	36.68	79.96	240	2.15	5.21	29.21	168.64
190	1.07	2.70	28.38	153.43	240	0.57	1.21	32.02	82.96					

# 5D.7.1 Comparison of $W_{rec}$ and temperature sustainability between the present work and previous reports

Table 5D.7 illustrates the comparison of maximum temperature sustainability and  $W_{rec}$  between the present work and previous reports on bulk ceramics, where the stable P-E curves were observed up to 190 °C with  $W_{rec}$  of 2.5 J cm<sup>-3</sup>. Table 5D.8 illustrates the key findings of  $W_{rec}$  based on the sample thickness (t) of the current investigated BFO-CTO (t ~ 0.3 mm) composition and the results from the earlier investigations. The results revealed that by reducing the thickness of the sample,  $W_{rec}$  is increasing which is ascribed to the extrinsic defects minimization. Hence the present composition (BFO-CTO) has a huge potential to improve its performance by reducing the sample thickness. These findings demonstrate a significant improvement compared to the earlier research reports in terms of performance.

Table 5D. 7 Comparison of maximum temperature sustainability and W<sub>rec</sub> between the present work and previous reports on bulk ceramics

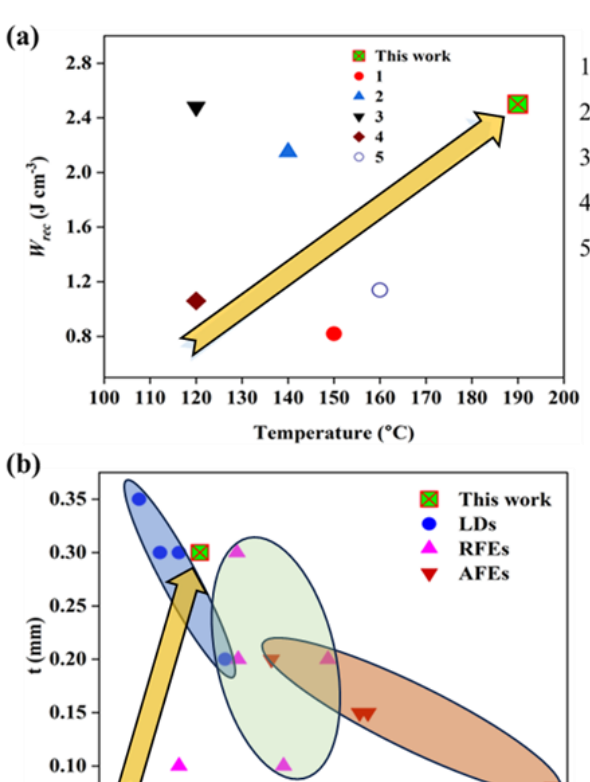
	Temperature	Wrec	
Composition	(°C)	(J cm <sup>-3</sup> )	Ref.

(1-x) BiFeO <sub>3</sub> -0.30BaTiO <sub>3</sub> -xAgNbO <sub>3</sub> +	150	0.82	(1)
5 mol% CuO ( $x = 0.14$ )			
$(1-x) \text{ BaTiO}_3 -x (\text{Mg}_{2/3}\text{Ta}_{1/3}) \text{ O}_3$	140	2.15	(2)
$Na_{0.7}Bi_{0.1}NbO_3 (x = 0.12)$	120	2.48	(3)
(1-x) K <sub>0.5</sub> Na <sub>0.5</sub> NbO <sub>3</sub> -xBi (Zn <sub>0.5</sub> Zr <sub>0.5</sub> ) O <sub>3</sub>	120	1.06	(4)
(x = 0.15)	120	1.00	(4)
0.95((1-x) Bi <sub>0.5</sub> Na <sub>0.5</sub> TiO <sub>3</sub> -xSr <sub>0.7</sub> Bi <sub>0.2</sub> TiO <sub>3</sub>	160	1.14	(5)
$(x = 0.4)) -0.05 \text{AgNbO}_3$	100	1.17	(3)
Present work	190	2.5	

Table 5D. 8 Comparison of  $W_{rec}$  between previous reports and present work based on the thickness of the bulk ceramics

Composition	Thickness	W <sub>rec</sub>	Ref.
Composition	(mm)	(J cm <sup>-3</sup> )	KCI.
LDs			
0.88SrTiO <sub>3</sub> -0.02CaZrO <sub>3</sub> -0.1MgTiO <sub>3</sub> +BaCu(B <sub>2</sub> O <sub>5</sub> )	0.35	1.05	(6)
0.9(Sr <sub>0.7</sub> Bi <sub>0.2</sub> ) TiO <sub>3</sub> -0.1Bi (Mg <sub>0.5</sub> Hf <sub>0.5</sub> ) O <sub>3</sub>	-	3.1	(7)
$Ca_{0.97}Sm_{0.02}TiO_3$	-	2.0	(8)
0.9CaTiO <sub>3</sub> -0.1BiScO <sub>3</sub>	-	1.55	(9)
RFEs			
0.8(0.95Bi <sub>0.5</sub> Na <sub>0.5</sub> TiO <sub>3</sub> -0.05SrZrO <sub>3</sub> )-0.2NaNbO <sub>3</sub>	0.20	5.55	(10)
$0.9K_{0.5}Na_{0.5}NbO_3-0.1BiFeO_3$	-	2.0	(11)

$0.61 BiFeO_3 - 0.33 (Ba_{0.8} Sr_{0.2}) TiO_3 - 0.06 La (Mg_{2/3} Nb_{1/3})$			
O <sub>3</sub> +0.1wt.%MnO <sub>2</sub> +2wt.%BaCu(B <sub>2</sub> O <sub>5</sub> )	0.30	3.38	(12)
0.90BaTiO <sub>3</sub> -0.10Bi (Mg <sub>0.5</sub> Zr <sub>0.5</sub> ) O <sub>3</sub> @SiO <sub>2</sub>	0.20	3.41	(13)
0.6BaTiO <sub>3</sub> -0.4Bi (Mg <sub>1/2</sub> Ti <sub>1/2</sub> ) O <sub>3</sub>	0.10	4.49	(14)
Present work	0.30	2.5	
AFEs			
AgNb <sub>0.85</sub> Ta <sub>0.15</sub> O <sub>3</sub>	0.20	4.20	(15)
	0.20 0.15	4.20 6.30	(15) (16)
AgNb <sub>0.85</sub> Ta <sub>0.15</sub> O <sub>3</sub>			, ,



0.05

3

5 6 7 W<sub>rec</sub> (J cm<sup>-3</sup>)

2

- 1. 0.56BiFeO<sub>3</sub>-0.3BaTiO<sub>3</sub> 0.14AgNbO<sub>3</sub>+ 5 mol% CuO
- 2. 0.88BaTiO<sub>3</sub> -0.12Bi(Mg<sub>2/3</sub>Ta<sub>1/3</sub>)O<sub>3</sub>
- 3. Na<sub>0.7</sub>Bi<sub>0.1</sub>NbO<sub>3</sub>
- 4. 0.85K<sub>0.5</sub>Na<sub>0.5</sub>NbO<sub>3</sub>-0.15Bi (Zn<sub>0.5</sub>Zr<sub>0.5</sub>)O<sub>3</sub>
- 5. 0.95(0.6Bi<sub>0.5</sub>Na<sub>0.5</sub>TiO<sub>3</sub>-0.4Sr<sub>0.7</sub> Bi<sub>0.2</sub>TiO<sub>3</sub> -0.05AgNbO<sub>3</sub>

Figure 7a illustrates the comparison of maximum temperature sustainability and recoverable energy density ( $W_{rec}$ ) between the present work and previous reports on bulk ceramics, where the stable P-E curves were observed up to 190 °C with  $W_{rec}$  of 2.5 J cm<sup>-3</sup> (see

10

Table S7[1-5] for the corresponding data). Higher Wrec value at high temperature clearly indicates that our material composition will have significant advantage in terms of potential energy storage applications in space, defence, data-centres, and electric vehicles. Similarly, Figure 7b demonstrate comparison of  $W_{rec}$  based on the sample thickness (t) of the current investigated BFO-CTO (t ~ 0.3 mm) composition and the results from the earlier investigations with similar composition and thickness range from ~0.1mm to ~0.35mm (see Table S8 [6-18] for the corresponding data). The results revealed that with reducing the thickness of the sample  $W_{rec}$  is increasing which is ascribed to the extrinsic defects minimization. Hence the present composition (BFO-CTO) has a huge potential to improve its performance by reducing the sample thickness. These findings demonstrate a significant improvement compared to the earlier research reports in terms of quantifiable performance parameter like value of  $W_{rec}$ . Temperature and thickness (t) dependent behaviour of Wrec strongly suggests that our composite material choice and fabrication protocol has significantly improved the crucial energy storage capability.

#### **REFERENCES**

- (1) Q. Qing Wang, Z. Wang, X. Qiang Liu, X. Ming Chen, Improved structure stability and multiferroic characteristics in CaTiO<sub>3</sub>-modified BiFeO<sub>3</sub> ceramics. J. Am. Ceram. Soc. 95(2), 670–675 (2012). https://doi.org/10.1111/j.1551-2916. 2011.04824.x
- (2) Gomasu Sreenu, S. Saha, R.N. Bhowmik et al., Investigation of structural, electrical, and dielectric properties of lead-free (BiFeO3)(1-x) (CaTiO3)x ceramics. J. Mater. Sci: Mater. Electron. 33, 24959–24971 (2022). https://doi.org/10.1007/s10854-022-09205-6
- (3) Wang, W.; Zhang, L.; Li, C.; Alikin, D. O.; Shur, V. Y.; Wei, X.; Gao, F.; Du, H.; Jin, L. Effective Strategy to Improve Energy Storage Properties in Lead-Free (Ba0.8Sr0.2)TiO3-Bi(Mg0.5Zr0.5)O3 Relaxor Ferroelectric Ceramics. Chem. Eng. J. 2022, 446, 137389.
- (4) T.M. Correia, M. McMillen, M.K. Rokosz, P.M. Weaver, J.M. Gregg, G. Viola, M.G. Cain, A lead-free and high-energy density ceramic for energy storage applications. J. Am. Ceram. Soc. (2013). https://doi.org/10.1111/jace.12508
- (5) Ishiwara, H. Impurity substitution effects in BiFeO<sub>3</sub> thin films. From a viewpoint of FeRAM applications. Curr. Appl. Phys. 12, 603–611 (2012).
- (6) F. Yan, Y. Shi, X. Zhou, K. Zhu, B. Shen, J. Zhai, Optimization of polarization and electric field of bismuth ferrite-based ceramics for capacitor applications, Chem. Eng. J. 417 (2021) 127945.
- (7) D. Wang, Z. Fan, D. Zhou, A. Khesro, S. Murakami, A. Feteira, Q. Zhao, X. Tan, I.M. Reaney, Bismuth ferrite-based lead-free ceramics and multilayers with high recoverable energy density, J. Mater. Chem. A 6 (2018) 4133–4144.
- (8) Subhadeep Saha et.al., Effect of Nd<sup>3+</sup> substitution on structural, morphological, and electrical properties of Bismuth Ferrite ceramics, J Mater Sci: Mater Electron (2023) 34:559, https://doi.org/10.1007/s10854-023-09947-x
- (9) Wang, Y. & Nan, C. Enhanced ferroelectricity in Ti-doped multiferroic BiFeO3 thin films. Appl. Phys. Lett. 89, 52903 (2006).
- (10) Guo, Y. et al. Critical roles of Mn-ions in enhancing the insulation, piezoelectricity and multiferroicity of BiFeO3-based lead-free high-temperature ceramics. J. Mater. Chem. C. 3, 5811–5824 (2015).
- (11) H. Pan, J. Ma, Ji. Ma, Q. Zhang, X. Liu, Bo. Guan, Gu. Lin, X. Zhang, Y.-J. Zhang, et. al., Giant energy density and high efficiency achieved in bismuth ferrite-based film

- capacitors via domain engineering. Nat. Commun. (2018) https://doi.org/10.1038/s41467-018-04189-6
- (12) Khan, M. A., Comyn, T. P. & Bell, A. J. Leakage mechanisms in bismuth ferrite-lead titanate thin films on Pt/Si substrates. Appl. Phys. Lett. 92, 72908 (2008).
- (13) V. A. Sotskov, Features of the temperature and concentration dependences of resistivity in disordered macroscopic composite systems of the insulator-semiconductor type, ech. Phys. 50, 1162–1165 (2005). https://doi.org/10.1134/1.2051455
- (14) M. M. Kumar, V. R. Palkar, K. Srinivas, and S. V. Suryanarayana, "Ferroelectricity in a Pure BiFeO3 Ceramic," Appl. Phys. Lett., 76 [19] 2764–6 (2000).
- (15) I.I. Makoed, N.A. Liedienov, et.al., Influence of rare-earth doping on the structural and dielectric properties of orthoferrite La0.50R0.50FeO3 ceramics synthesized under high pressure, J. Alloys Compd. 842 (2020), https://doi.org/10.1016/j.jallcom.2020.155 859
- (16) D.W. Davidson, R.H. Cole, Dielectric relaxation in glycerol, propylene glycol, and n-propanol, J. Chem. Phys. 19 (1951) 1484–1490, https://doi.org/10.1063/1.1748105.
- (17) T.P. Iglesias, G. Vil~ao, J.C.R. Reis, An approach to the interpretation of Cole-Davidson and Cole-Cole dielectric functions, J. Appl. Phys. (2017) 122, https://doi.org/101.4985839
- (18) S. Leelashree, S.N. Kaul, S. Srinath, Effect of progressive substitution of Lu by Ho on the structural and dielectric properties of nanocrystalline LuFeO3 orthoferrite, Materials Research Bulletin 145 (2022) 111570, https://doi.org/10.1016/j.materresbull.2021.111570
- (19) L. Zhang, X.M. Chen, Dielectric relaxation in LuFeO3 ceramics, Solid State Commun. 149 (2009) 1317–1321, https://doi.org/10.1016/j.ssc.2009.05.036
- (20) Y. Saad, I. 'Alvarez-Serrano, M. L. L'opez and M. Hidouri, Structural and dielectric characterization of new lead-free perovskites in the (SrTiO3)–(BiFeO3) system, Ceram. Int., 2016, 42, 8962–8973, https://doi.org/10.1016/j.ceramint.2016.02.028
- (21) Z. Z. Ma, Z. M. Tian, J. Q. Li, C. H. Wang, S et.al., Enhanced polarization and magnetization in multiferroic (1-x) BiFeO3-xSrTiO3 solid solution, Solid State Sci., 2011, 13, 2196–2200, https://doi.org/10.1016/j.solidstatesciences.2011.10.008
- (22) Hao Pan, Yi Zeng, Yang Shen, Yuan-Hua Lin, Jing Ma, Liangliang Li and Ce-Wen Nan, BiFeO3–SrTiO3 thin film as a new lead-free relaxor-ferroelectric capacitor with ultrahigh energy storage performance, Journal of Materials Chemistry, A 5(12):5920—5926, April 2017, https://doi.org/10.1039/C7TA00665A

- (23) Tao Cui, Ji Zhang, Jian Guo, Xiongjie Li, Shun Guo, Yu Huan, Jing Wang, Shan-Tao Zhang, Yaojin Wang, Outstanding comprehensive energy storage performance in lead-free BiFeO3-based relaxor ferroelectric ceramics by multiple optimization design, Acta Materialia, Volume 240, 2022, 118286, https://doi.org/10.1016/j.actamat.2022.118286
- (24) Rhys Montecillo, et. al., Optimized electric-energy storage in BiFeO3–BaTiO3 ceramics via tailoring microstructure and nanocluster, Journal of the European Ceramic Society. 43, 5, 1941-1951, (2023). https://doi.org/10.1016/j.jeurceramsoc.2022.12.064
- (25) Z. Shen, X. Wang, B. Luo, et.al., BaTiO3–BiYbO3 perovskite materials for energy storage applications, J. Mater. Chem. A, 2015, 3, 18146–18153, https://doi.org/10.1039/C5TA03614C
- (26) Sun, H.; Wang, X.; Sun, Q.; Zhang, X.; Ma, Z.; Guo, M.; Sun, B.; Zhu, X.; Liu, Q.; Lou, X. Large Energy Storage Eensity in BiFeO3-BaTiO3-AgNbO3 Lead-Free Relaxor Ceramics. J. Eur. Ceram. Soc. 2020, 40 (8), 2929-2935, DOI: 10.1016/j.jeurceramsoc.2020.03.012.
- (27) X Chen, X. L., J Sun, C Sun, J Shi, F Pang, H Zhou. Simultaneously Achieving Utrahigh Energy Storage Density and Energy Efficiency in Barium Titanate Based Ceramics. Ceram. Int. 2020, 46 (3), 2764-2771, DOI: 10.1016/j.ceramint.2019.09.265.
- (28) Zhou, M.; Liang, R.; Zhou, Z.; Dong, X. Superior Energy Storage Properties and Excellent Stability of Novel NaNbO3-Based Lead-Free Ceramics with A-Site Vacancy Obtained via A Bi2O3 Substitution Strategy. J. Mater. Chem. A 2018, 6 (37), 17896-17904, DOI: 10.1039/c8ta07303a.
- (29) Zhang, M.; Yang, H.; Li, D.; Ma, L.; Lin, Y. Giant Energy Storage Efficiency and High Recoverable Energy Storage Density Achieved in K0.5Na0.5NbO3-Bi(Zn0.5Zr0.5)O3 Ceramics. J. Mater. Chem. C 2020, 8 (26), 8777-8785, DOI: 10.1039/d0tc01711f.
- (30) Qiao, X.; Wu, D.; Zhang, F.; Chen, B.; Ren, X.; Liang, P.; Du, H.; Chao, X.; Yang, Z. Bi0.5Na0.5TiO3-Based Relaxor Ferroelectric Ceramic with Large Energy Density and High Efficiency under A Moderate Electric Field. J. Mater. Chem. C 2019, 7 (34), 10514-10520, DOI: 10.1039/c9tc03597d.
- (31) Lingxia Li, et al., Preparation and dielectric properties of BaCu(B<sub>2</sub>O<sub>5</sub>)-doped SrTiO<sub>3</sub>-based ceramics for energy storage, Mater. Sci. Eng. B 178 (2013) 1509-1514
- (32) Xi Kong, et al., Bi-modified SrTiO<sub>3</sub>-based ceramics for high-temperature energy storage applications, J. Am. Ceram. Soc. 103 (2019) 1722-1731
- (33) Jiawei Zhang, et al., Enhanced energy storage performances of CaTiO3-based ceramic through A-site Sm3+ doping and A-site vacancy, J. Eur. Ceram. Soc. 41 (2021) 352-359

- (34) Bingcheng Luo, at al., Enhanced Energy-Storage Density and High Efficiency of Lead-Free CaTiO3–BiScO3 Linear Dielectric Ceramics, ACS Appl. Mater. Interfaces 9 (2017) 19963-19972
- (35) Chaoqiong Zhu, et al., Multiphase Engineered BNT-Based Ceramics with Simultaneous High Polarization and Superior Breakdown Strength for Energy Storage Applications, ACS Appl. Mater. Interfaces 13, 24 (2021) 28484-28492
- (36) Zetian Yang, et al., Grain size engineered lead-free ceramics with both large energy storage density and ultrahigh mechanical properties, Nano Energy 58 (2019) 768-777
- (37) Haoguang Yang, et al., Enhanced breakdown strength and energy storage density in a new BiFeO3-based ternary lead-free relaxor ferroelectric ceramic, J. Eur. Ceram. Soc. 39 (2019) 2673-2679
- (38) Qibin Yuan, et al., Bioinspired Hierarchically Structured All-Inorganic Nanocomposites with Significantly Improved Capacitive Performance, Adv. Funct. Mater. 30 (2020) 2000191
- (39) Qingyuan Hu, et al., Achieve ultrahigh energy storage performance in BaTiO3–Bi(Mg1/2Ti1/2)O3 relaxor ferroelectric ceramics via nano-scale polarization mismatch and reconstruction, Nano Energy 67 (2020) 104264
- (40) Lei Zhao, et al., Lead-Free Antiferroelectric Silver Niobate Tantalate with High Energy Storage Performance, Adv. Mater. 29 (2017) 1701824
- (41) Nengneng Luo, et al., Constructing phase boundary in AgNbO3 antiferroelectrics: pathway simultaneously achieving high energy density and efficiency, Nat. Commun. 11 (2020) 4824
- (42) Zhilun Lu, et al., Mechanism of enhanced energy storage density in AgNbO3-based lead-free antiferroelectrics, Nano Energy 79 (2021) 105423
- (43) Jie Jiang, et al., Enhanced energy storage properties of lead-free NaNbO3-based ceramics via A/B-site substitution, Chem. Eng. J. 422 (2021) 130130

#### **CHAPTER - 6**

#### SUMMARY AND CONCLUSIONS

In summary, the conventional method was used to fabricate a novel lead-free BFO-STO, BFO-CTO and BFO-BZO ceramics. Dielectric properties were characterized at room temperature in a large frequency range from 20 Hz to 1.8 GHz. XRD analysis has demonstrated differences in their crystalline structure. BFO-STO exhibits a very different behaviour because its XRD pattern contains simultaneous peaks from diffracting planes of BFO and STO. In comparison, the diffraction patterns of BFO-BZO and BFO-CTO are dominated by the peaks from diffracting planes of BZO and CTO, respectively. SEM microstructure of BFO-BZO shows a nearly bi-modal distribution with spherical morphology of the grains. The microstructure of BFO-CTO is very different, with a nearly homogeneous structure composed of big faceted grains. Relatively wider grain size distribution has been observed for the BFO-STO ceramic.

(BFO) (1-x) - (CTO)<sub>x</sub>,  $0 \le x \le 1$  ferroelectric ceramic were fabricated from the calcined powders of BFO and CTO, prepared by auto combustion route. Structural and microstructural characteristics were systematically explored. Weighted phase fraction, lattice parameters and volume variations were identified using the Rietveld refinement technique. Distorted perovskite schematic layout was visualized, and the angles between the atoms were measured. Highly dense, porosity-free micrographs were observed with increasing CTO concentration.

A novel lead-free (1-x) BFO-xCTO (x = 0.6, 0.7, and 0.8) RFEs were synthesized using solution auto combustion, and structural and microstructural properties were systematically explored. CTO incorporation into the BFO-CTO matrix suppressed the formation of oxygen vacancies, and Fe-ion fluctuations by inhibiting the Fe<sup>+3</sup> to Fe<sup>+2</sup> transition, confirmed through XPS. I-V hysteresis loops, frequency, temperature-dependent dielectric properties and dielectric relaxation times were discussed in detail. The ultrafast dielectric relaxation time of 44  $\mu$ s was obtained for 0.7 of x.

#### **Conclusions**

- Four orders of magnitude reduction in the leakage current density, from  $1.9 \times 10^{-1}$  A cm<sup>-2</sup> for x = 0 to  $7.4 \times 10^{-5}$  A cm<sup>-2</sup> for x = 0.8, at a field of 1 kVcm<sup>-1</sup> has been obtained in the sintered BFO-CTO samples.
- ➤ The presence of CTO in the BFO-CTO solid solution has increased the dielectric constant and decreased the loss tangent values compared to pure BFO, which is extremely lossy.
- A significant increase in the  $(\rho)$  was observed by two orders of magnitude, i.e., from  $2.21 \times 10^3 \ \Omega \ \text{cm} \ (x=0)$  to  $8.80 \times 10^5 \ \Omega \ \text{cm} \ (x=0.5)$ .
- The *J* is reduced by nearly two orders of magnitude from  $\sim 2.60 \times 10^{-1} \,\mathrm{A \ cm^{-2}}$  (x = 0) to  $\sim 2.50 \times 10^{-3} \,\mathrm{A \ cm^{-2}}$  (x = 0.5) at an electric field of 1 kV cm<sup>-1</sup>.
- The  $\varepsilon_r$  increased with increasing CTO content, e.g.,  $\sim 24$  for x = 0.1 and  $\sim 51$  for x = 0.5 at a frequency of 10 MHz. The  $\tan \delta$  is reduced by increasing CTO concentration, e.g.,  $\sim 1.39$  (at 10 kHz, x = 0) to  $\sim 0.35$  (at 10 kHz, x = 0.5) and  $\sim 0.37$  (at 10 MHz, x = 0.5) to 0.17 (at 10 MHz, x = 0.5).
- The enhanced electrical ( $\rho$  or  $\sigma$  and J), dielectric properties ( $\varepsilon_r$  and  $\tan \delta$ ), and RFE behaviour suggest that the BFO-CTO material can be a good candidate for energy storage applications.
- ➤ The partial substitution of Ca<sup>+2</sup>, and Ti<sup>+4</sup> ions in A and B sites of Bi<sup>+3</sup>, and Fe<sup>+3</sup> enhanced the relaxor ferroelectric nature by degrading the long-range FE orders and emergence of PNRs. As a result, high maximum polarization, and energy density of 2.5 J cm<sup>-3</sup> is achieved.
- ➤ P-E curves are stable up to 190 °C with a marginal efficiency variation (≤ 10% from 40°C to 190°C), suggesting that the BFO-CTO ceramics can be used for high-temperature energy storage applications.

#### Future scope of the present research work

- lacktriangle Thickness of the sample needs to be reduced to eliminate the associated extrinsic defects and the efficiency can be doubled thereby  $W_{rec}$  can also be doubled as reported in the present work.
- ♣ If we can improve the sintered density by 1% or 2% it significantly affects the energy storage properties.
- ♣ Sintering in different atmospheric conditions, i.e., in the presence of Oxygen, Nitrogen, Hydrogen and vacuum may significantly affect the sintering density.
- ♣ The RFE nature can be enhanced by trying different BFO-CTO composition proportions.
- ♣ Stable P-E loops can be achieved even above 200 °C by reducing leakage current density.

#### LIST OF PUBLICATIONS FROM THE CURRENT RESEARCH WORK

- Gomasu Sreenu, Mahfooz Alam, Didier Fasquelle, Dibakar Das "High-frequency dielectric characterization of novel lead-free ferroelectrics" J Mater Sci: Mater Electron, 31, 18477–18486 (2020). <a href="https://doi.org/10.1007/s10854-020-04391-7">https://doi.org/10.1007/s10854-020-04391-7</a>
- 2. **Gomasu Sreenu**, Subhadeep Saha, R. N. Bhowmik, J. P. Praveen, Dibakar Das "Investigation of structural, electrical, and dielectric properties of lead-free (BiFeO<sub>3</sub>)<sub>(1-x)</sub> (CaTiO<sub>3</sub>)<sub>x</sub> ceramics" J Mater Sci: Mater Electron 33, 24959–24971 (2022). https://doi.org/10.1007/s10854-022-09205-6
- 3. Subhadeep Saha, <u>Gomasu Sreenu</u>, J Paul Praveen, Dibakar Das "Effect of Nd<sup>3+</sup> substitution on structural, morphological, and electrical properties of Bismuth Ferrite ceramics" J Mater Sci: Mater Electron 34, 559 (2023). <a href="https://doi.org/10.1007/s10854-023-09947-x">https://doi.org/10.1007/s10854-023-09947-x</a>
- 4. <u>Gomasu Sreenu</u>, Subhadeep Saha, and Dibakar Das, "Synthesis of Novel Lead-free (BiFeO3)(x) (CaTiO3)(1-x) Ceramics and Thermal, Structural, Microstructural and Ferroelectric Characterizations for Energy Storage Applications" AIP conference proceedings (2023) (Accepted)
- 5. <u>Gomasu Sreenu</u>, Subhadeep Saha, Dibakar Das, et al., "Effect of Partial Substitution of CTO on Structural, Microstructural, Electrical and Dielectric Properties of BFO-based Lead-Free Ceramics Through Microwave Sintering" (Ready for submission)
- 6. <u>Gomasu Sreenu</u>, Subhadeep Saha, Dibakar Das, et al., "Achieving High-energy Density in Relaxor Nature Enhanced Lead-free BiFeO<sub>3</sub>-CaTiO<sub>3</sub> Ferroelectric Ceramics for High-Temperature Energy Storage Applications", (Ready for submission)
- 7. <u>Gomasu Sreenu</u>, Subhadeep Saha, Dibakar Das, "Investigation of Structural, Microstructural and Optical Properties of Lead-free (BiFeO<sub>3</sub>)(1-x) (CaTiO<sub>3</sub>)<sub>x</sub> Ceramics in Submillimeter Region" (Ready for submission)
- 8. Subhadeep Saha, <u>Gomasu Sreenu</u>, and Dibakar Das et al., "Investigation of the dielectric and optoelectronic properties of Nd3+- substituted bismuth ferrite ceramics in THz/far-infrared region", (Ready for submission)
- 9. Subhadeep Saha, <u>Gomasu Sreenu</u> and Dibakar Das, "Study of Frequency and Temperature-dependent responses of Dielectric permittivity with morphotropic phase boundary in Nd-substituted bismuth ferrite ceramics" (Ready for submission)

#### LIST OF CONFERENCE PRESENTATIONS/TALKS

- Gomasu Sreenu, Dibakar Das, Oral talk on "Lead-free ferroelectric materials for energy storage applications" at Science, Technology, and Innovation Talks (STIN-2021) as a part of National Science Day celebrations organized by the International Advanced Research Centre for Powder Metallurgy and New Materials (ARCI), held from 25<sup>th</sup>- 26<sup>th</sup> February-2021, Hyderabad, India.
- 2. <u>Gomasu Sreenu</u>, Subhadeep Saha, Dibakar Das, Poster presentation on "Synthesis and characterization of (x)BiFeO3 (1-x) CaTiO3 solid solution for structural, morphological, thermal and electrical properties" at Second International e-conference on Physics of Materials & Nanotechnology (ICPN-2021) held from 28<sup>th</sup> to 30<sup>th</sup> Oct 2021, Organized by Department of Physics, Mangalore University, India.
- 3. <u>Gomasu Sreenu</u>, Subhadeep Saha, Dibakar Das, Flash talk/Oral presentation on "Structural and electrical characterizations of novel lead-free ferroelectric bulk ceramics (1-x)BiFeO3 –xCaTiO3 for energy storage applications" in the 'International Virtual Conference on Advanced Ceramics and Technologies: Materials and manufacturing (IvaCCT- 2021) held from 13<sup>th</sup>-14<sup>th</sup> Dec 2021 organized by Indian ceramic society Karnataka chapter.
- 4. <u>Gomasu Sreenu</u>, Subhadeep Saha, RN Bhowmik, Dibakar Das, **Oral presentation** on "A Novel Lead-free Ferroelectric High Energy Density Ceramic System for High-Temperature Energy Storage Applications" at AEM2022 **Imperial College London**, UK held from 6<sup>th</sup> 8<sup>th</sup> April 2022.
- Sreenu Gomasu, Subhadeep Saha, RN Bhowmik, D Das, Poster presentation "Dielectric and Ferroelectric Characteristics of (BiFeO3)(1-x) –(CaTiO3)x Lead-Free Ceramics for High-Temperature Energy Storage Application" at IIM-ATM, RFC Hyderabad, India held from 14<sup>th</sup> – 16<sup>th</sup> November 2022.
- 6. Gomasu Sreenu, Subhadeep Saha, D das Poster presentation "Dielectric and Electrical Characterizations of Lead-free (BiFeO3)(1-x) (CaTiO3)x Ceramics for Energy Storage Applications" at Global Trends in Traditional to Space Ceramics organized by Indian ceramic society, IIT-BHU held from 8<sup>th</sup> 9<sup>th</sup> December 2022.
- 7. <u>Gomasu Sreenu</u>, Subhadeep Saha, Dibakar Das, Poster presentation "Synthesis of Novel Lead-free (BiFeO<sub>3</sub>)<sub>(x)</sub> (CaTiO<sub>3</sub>)<sub>(1-x)</sub> Ceramics and Thermal, Structural,

- Microstructural and Ferroelectric Characterizations for Energy Storage Applications" at 66th DAE Solid State Physics Symposium, Birla Institute of Technology Jharkhand, India held from 18<sup>th</sup> to 22<sup>nd</sup> Dec 2022.
- 8. <u>Gomasu Sreenu</u>, Subhadeep Saha, RN Bhowmik, Dibakar Das Poster presentation on "Structural and Electrical Characteristics of a novel Lead-free Ferroelectric (1-x)BiFeO3 –xCaTiO3 Ceramics for High-Temperature Energy Storage Application" at advanced in functional materials (AFM), Kyushu University, Fukuoka, Japan held from 9<sup>th</sup> to 12<sup>th</sup> Jan 2023.
- 9. Subhadeep Saha, <u>Gomasu Sreenu</u> and Dibakar Das, Poster presentation on "Synthesis and Structural Characterization of Nd-doped Bismuth Ferrite" at Second International e-conference on Physics of Materials & Nanotechnology (ICPN-2021) held from 28<sup>th</sup> to 30<sup>th</sup> Oct 2021, Organized by Department of Physics, Mangalore University, India.
- 10. Subhadeep Saha, <u>Gomasu Sreenu</u> and Dibakar Das, Flash-talk presentation on "Effect of Nd<sup>3+</sup> doping in Bismuth Ferrite Ceramics" at International Virtual Conference on Advanced Ceramics and Technologies: Materials and manufacturing (IvaCCT- 2021) held from 13<sup>th</sup>-14<sup>th</sup> Dec 2021 organized by Indian ceramic society Karnataka chapter, PDA College of Engineering, Kalaburagi, Karnataka, India.
- 11. Subhadeep Saha, <u>Gomasu Sreenu</u>, and Dibakar Das Poster presentation on "Electrical Characterizations of Nd substituted Bismuth Ferrite Ceramics for Energy Storage Applications" at IIM-ATM, RFC, Hyderabad, Telangana, India held from 14<sup>th</sup> 16<sup>th</sup> November 2022.
- 12. Subhadeep Saha, <u>Gomasu Sreenu</u> and Dibakar Das **Oral Presentation** on "Study of leakage current density in Nd<sup>3+</sup> substituted Bismuth Ferrite for Energy Storage Applications" at Global Trends in Traditional to Space Ceramics, held from 8<sup>th</sup> 9<sup>th</sup> December 2022 by Indian ceramic society, IIT-BHU, Banaras, UP, India.
- 13. Subhadeep Saha, <u>Gomasu Sreenu</u>, RN Bhowmik and Dibakar Das, Poster presentation on "Structural, Morphological and Electrical Characterization of Nd substituted Bismuth Ferrite Ceramics for Energy Storage Applications" at advanced in functional materials (AFM), Kyushu University, Fukuoka, Japan, held from 9<sup>th</sup> to 12<sup>th</sup> Jan 2023.

#### **AWARDS**

1. Gomasu Sreenu (18ETPM01), PhD scholar in School of Engineering Sciences and Technology (SEST), University of Hyderabad received Publication Incentive Award from the Institution of Eminence (IoE), University of Hyderabad, based on the publication entitled "High-Frequency Dielectric Characterization of Novel Lead-Free Ferroelectric"

Dr. Dibakar Das
Professor,
School of Engineering Sciences and Technology (SEST),
University of Hyderabad,
Hyderabad-500046, INDIA,
E-mail: dibakardas@uohyd.ac.in or dibakar1871@gmail.com

Tel: 91 – 040 23134454 (Office), 91 – 958104879 (Mobile)



Date: 27th July 2023

To
The Controller of Examination (CE),
University of Hyderabad,
Hyderabad – 500046.

Through
Dean SEST,
University of Hyderabad.

Subject - Ph.D. thesis submission of Gomasu Sreenu (Reg. No. 18ETPM01) reg.

Dear Sir,

Please find the enclosed Ph.D. thesis titled "Investigation of Novel Lead-Free BiFeO<sub>3</sub> - CaTiO<sub>3</sub> Piezoelectric Ceramics for High-Temperature Energy Storage Applications" by Gomasu Sreenu (Reg. No. 18ETPM01). The thesis has been checked for plagiarism from the central library of University of Hyderabad and the report shows a similarity index of 33%, out of which 28% is from our own work. So, an effective similarity index of 5 % (33-28) has been found for the thesis, which is within the acceptable limit. Hope you will find everything in order.

Please let me know if you need anything else in this regard.

Thanking you in anticipation.

Sincerely yours,

(Prof. Dibakar Das, Supervisor)

TOI. Dibakar Was, purper visory Park India

School of Engineering Sciences & Technology Engineering Sciences & Technology University of Hyderabad Hyderabad-500046.

# Investigation of Novel Lead-Free BiFeO3-CaTiO3 Piezoelectric Ceramics for High-Temperature Energy Storage Applications

by Gomasu Sreenu

Submission date: 26-Jul-2023 10:48PM (UTC+0530)

**Submission ID:** 2137173576

File name: Gomasu\_Sreenu.pdf (10.16M)

Word count: 22774 Character count: 113582

# Investigation of Novel Lead-Free BiFeO3-CaTiO3 Piezoelectric Ceramics for High-Temperature Energy Storage Applications

ORIGINALI	TY REPORT	
3.5 SIMILAR	31% 33% 2% STUDENT STUDENT	PAPERS
PRIMARY :	SOURCES CONTROL OF THE PROPERTY OF THE PROPERT	
1	link.springer.com Internet Source	26%
2	Gomasu Sreenu, Subhadeep Saha, R. N. Bhowmik, J. P. Praveen, Dibakar Das. "Investigation of structural, electrical, and dielectric properties of lead-free (BiFeO3)(1-x)  – (CaTiO3)x ceramics", Journal of Materials Science: Materials in Electronics, 2022	29
	- pubs.acs.org	
3	Internet Source	9,
4	en.wikipedia.org	<19
5	Bushra Khan, Aditya Kumar, Preeti Yadav, Gulab Singh, Upendra Kumar, Ashok Kumar, Manoj K. Singh. "Structural, dielectric, magnetic and magneto-dielectric properties	<19

Publication

Gomasu Sreenu, Mahfooz Alam, Didier <1% 6 Fasquelle, Dibakar Das. "High-frequency dielectric characterization of novel lead-free ferroelectrics", Journal of Materials Science: Materials in Electronics, 2020 Publication Letao Yang, Xi Kong, Fei Li, Hua Hao, <1% Zhenxiang Cheng, Hanxing Liu, Jing-Feng Li, Shujun Zhang. "Perovskite Lead-free dielectrics for energy storage applications", Progress in Materials Science, 2018 Publication hdl.handle.net <1% 8 Internet Source Zetian Yang, Hongliang Du, Li Jin, Dirk 9 Poelman. "High-Performance Lead-Free Bulk Ceramics for Energy Storage Applications: Design strategies and Challenges", Journal of Materials Chemistry A, 2021 Publication Mürbe, Julia, and Jörg Töpfer. "Phase <1% 10 Formation, Sintering Behavior, and Magnetic Properties of Low-Temperature Fired Mg-Cu-Zn Ferrites", Journal of the American Ceramic Society, 2012.

11	eprints.whiterose.ac.uk Internet Source	<1%
12	"Advances in Nanostructured Materials", Springer Science and Business Media LLC, 2022 Publication	<1%
13	Ge Wang, Zhilun Lu, Yong Li, Linhao Li, Hongfen Ji, Antonio Feteira, Di Zhou, Dawei Wang, Shujun Zhang, Ian M Reaney. "Electroceramics for High-Energy Density Capacitors: Current Status and Future Perspectives", Chemical Reviews, 2021 Publication	<1%
14	coek.info Internet Source	<1%
15	Ming Liu, Ziyao Zhou. "Integrated Multiferroic Heterostructures and Applications", Wiley, 2019 Publication	<1%
16	Shuai Sun, Yuming Ye, Liuhuo Wang, Dequan Chen, Yi Chen, Xiongwu Tao, Junhong Zhou, Baichuan Deng, Longhao Zhang. "Enhanced electrostatic energy storage achieved in BiFeO3-driven (Sr,Bi)TiO3 ceramics for high-voltage pulsed applications", Ceramics International, 2022	<1%

17	Nawishta Jabeen, Ahmad Hussain, Muhammad Adnan Qaiser, Jazib Ali, Abdul Rehman, Nourreddine Sfina, Gharieb A. Ali, Vineet Tirth. "Enhanced Energy Storage Performance by Relaxor Highly Entropic (Ba0.2Na0.2K0.2La0.2Bi0.2)TiO3 and (Ba0.2Na0.2K0.2Mg0.2Bi0.2)TiO3 Ferroelectric Ceramics", Applied Sciences, 2022	<1%
18	ro.uow.edu.au Internet Source	<1%
19	Chenghao Zhu, Wenbo Ye, Peng Zheng, Hongfei Zhang, Fuan Lu, Qiaolan Fan, Jingji Zhang, Liang Zheng, Yang Zhang, Wangfeng Bai. "Fantastic Energy Storage Performances and Excellent Stability in BiFeO –SrTiO -Based Relaxor Ferroelectric Ceramics ", ACS Applied Energy Materials, 2022 Publication	<1%
20	Di Hu, Zhongbin Pan, Xiaoyan Tan, Fan Yang, Jie Ding, Xiang Zhang, Peng Li, Jinjun Liu, Jiwei Zhai, Hui Pan. "Optimization the Energy Density and Efficiency of BaTiO3-based Ceramics for Capacitor Applications", Chemical Engineering Journal, 2020 Publication	<1%
21	Haonan Sun, Xiangjian Wang, Qinzao Sun, Xiaoxiao Zhang, Zhuang Ma, Mengyao Guo,	<1%

Buwei Sun, Xiaopei Zhu, Qida Liu, Xiaojie Lou. "Large energy storage density in BiFeO3-BaTiO3-AgNbO3 lead-free relaxor ceramics", Journal of the European Ceramic Society, 2020

Wen Wang, Leiyang Zhang, Wenjing Shi, Yule Yang et al. "Enhanced Energy Storage Properties in Lead-Free (Na Bi ) Sr TiO -Based Relaxor Ferroelectric Ceramics through a Cooperative Optimization Strategy ", ACS Applied Materials & Interfaces, 2023

<1%

pubs.rsc.org

<1%

Bingcheng Luo, Xiaohui Wang, Enke Tian,
Hongzhou Song, Hongxian Wang, Longtu Li. "
Enhanced Energy-Storage Density and High
Efficiency of Lead-Free CaTiO –BiScO Linear
Dielectric Ceramics ", ACS Applied Materials &
Interfaces, 2017

<1%

- Publication
- Luo, Lingling, Na Jiang, Xiao Zou, Dongliang Shi, Ting Sun, Qiaoji Zheng, Chenggang Xu, Kwok Ho Lam, and Dunmin Lin. "Phase transition, piezoelectric, and multiferroic properties of La(Co0.5 Mn0.5 )O3 -modified BiFeO3 -BaTiO3 lead-free ceramics:

  Properties of LCMO-modified BiFeO3 -BaTiO3

<1%

### lead-free ceramics", physica status solidi (a), 2015.

Publication

Mahesh Peddigari, Haribabu Palneedi, Geon-Tae Hwang, Jungho Ryu. "Linear and Nonlinear Dielectric Ceramics for High-Power Energy Storage Capacitor Applications", Journal of the Korean Ceramic Society, 2018

<1%

Mane, Sagar, Pravin Tirmali, Snehal Kadam, Arjun Tarale, Chandrakant Kolekar, and Shrinivas Kulkarni. "Dielectric, magnetic, and magnetodielectric properties of x[Co0.9Ni0.1Fe2O4]-(1-x) [0.5(Ba0.7Ca0.3)TiO3)-0.5Ba(Zr0.2Ti0.8)O3] multiferroic composites", Journal of the Chinese Advanced Materials Society, 2016. Publication

<1%

Shibnath Samanta, V. Sankaranarayanan, K. Sethupathi. "Effect of micro-defects and Pbloss on electrical and optical properties of PLZT ceramic", Journal of Materials Science:

Materials in Electronics, 2018

Publication

<1%

T. Durga Rao, Saket Asthana. "Evidence of improved ferroelectric phase stabilization in Nd and Sc co-substituted BiFeO ", Journal of Applied Physics, 2014

<1%

30	es.scribd.com Internet Source	<1%
31	www.researchgate.net Internet Source	<1%
32	Submitted to Ahsanullah University of Science and Technology Student Paper	<1%
33	K.F. Wang, JM. Liu, Z.F. Ren. "Multiferroicity: the coupling between magnetic and polarization orders", Advances in Physics, 2009	<1%
34	Peng Shi, Xiaopei Zhu, Xiaojie Lou, Bian Yang, Qida Liu, Chuncai Kong, Sen Yang, Liqiang He, Ruirui Kang, Jiantuo Zhao. "Tailoring ferroelectric polarization and relaxation of BNT-based lead-free relaxors for superior energy storage properties", Chemical Engineering Journal, 2021	<1%
35	Yi Zhang, Aiwen Xie, Jian Fu, Xuewen Jiang, Tianyu Li, Cong Zhou, Ruzhong Zuo. " Superior Energy-Storage Properties in Bi Na TiO -Based Lead-Free Ceramics via Simultaneously Manipulating Multiscale Structure and Field- Induced Structure Transition ", ACS Applied Materials & Interfaces, 2022	<1%

Ying Lin, Da Li, Miao Zhang, Shili Zhan,
Yaodong Yang, Haibo Yang, Qibin Yuan. "
Excellent Energy-Storage Properties Achieved
in BaTiO -Based Lead-Free Relaxor
Ferroelectric Ceramics via Domain
Engineering on the Nanoscale ", ACS Applied
Materials & Interfaces, 2019
Publication

<1%

Feihong Pang, Xiuli Chen, Congcong Sun,
Junpeng Shi, Xu Li, Hongyun Chen, Xiaoyan
Dong, Huanfu Zhou. "Ultrahigh Energy
Storage Characteristics of Sodium NiobateBased Ceramics by Introducing a Local
Random Field", ACS Sustainable Chemistry &
Engineering, 2020

<1%

Chaoqiong Zhu, Ziming Cai, Limin Guo, Ying Jiang, Longtu Li, Xiaohui Wang. "
Simultaneously Achieved Ultrastable Dielectric and Energy Storage Properties in Lead-Free Bi Na TiO -Based Ceramics ", ACS Applied Energy Materials, 2022
Publication

<1%

Raghavan, C.M., J.W. Kim, and S.S. Kim.
"Effects of (Dy, Zn) co-doping on structural and electrical properties of BiFeO3 thin films",
Ceramics International, 2013.
Publication

<1%

Exclude quotes On Exclude matches < 14 words

Exclude bibliography On